STUDY OF COPPER-RICH INTERMETALLIC PHASE FORMATION

IN COPPER-ALUMINUM BINARY SYSTEM


by


VALERY GEORGES OUVAROV-BANCALERO


Presented to the Faculty of the Graduate School of

The University of Texas at Arlington in Partial Fulfillment

of the Requirements

for the Degree of


DOCTOR OF PHILOSOPHY


THE UNIVERSITY OF TEXAS AT ARLINGTON

May 2018

# ACKNOWLEDGEMENTS

First of all, I would like to express my deepest gratitude and appreciation to my research advisor, Dr. Choong-Un Kim. His off the charts knowledge and scientific intuition made me push my limits further every day during this incredible journey. I am indebted to him for giving me the chance to be part of his outstanding research team. I would also like to thank my committee members, Dr. Meletis, Dr. Hao, Dr. Michael, and Dr. Cao, for their time and valuable suggestions.

I would like to extend my special thanks to my colleagues and team members. There are too many for me to name them individually, but I am sure they will recognize themselves. Thank you for all the good moments we shared, and for your comradery.

I am also extremely grateful to our department secretaries, Beth Robinson, Jennifer Standlee, and Natalie Burden, for their continuous support and contagious cheerfulness.

Most importantly, I want to thank my parents and my sister for their incredible love and support. None of this amazing adventure would have been possible without you; I owe you everything. Papa, Maman, et Virginie, je vous aime de tout mon cœur et vous remercie infiniment pour tout le support et l'amour que vous m'avez donné. Je vous dédie cette thèse de doctorat et j'espère que vous êtes fiers de moi. Je vous aimerai et chérirai pour toujours.

Last but not least, I want to thank my girlfriend, Brooke, for all the love and energy she gave me for the past two and a half years. Her unconditional support greatly helped me in difficult times. I love you babe!

April 11, 2018

iii

ABSTRACT


STUDY OF COPPER-RICH INTERMETALLIC PHASE FORMATION

IN COPPER-ALUMINUM BINARY SYSTEM


Valery Georges Ouvarov-Bancalero, PhD


The University of Texas at Arlington, 2018


Supervising Professor: Choong-Un Kim

This work aims to study the initial formation and subsequent growth of intermetallic compounds (IMC) in the binary Al-Cu system. Al-Cu pair configurations have been successfully used for several decades as structural components, and extensive research on their mechanical and metallurgical properties is available. More recently, the microelectronics industry started implementing the Cu wire-bond technology, which renewed the interest of the scientific community. As with every technological evolution, initial quality and reliability issues arose. Copper (Cu) wire to aluminum (Al) bond-pad is prone to crack nucleation leading to failure at the interface between Cu and Cu-rich IMCs. Even though numerous studies are available on the subject, the wire bonding configuration makes the interface characterizations difficult and many unanswered questions remain. Consequently, and using an alternative approach, the main motivation of this study was to

determine the exact causes and underlying mechanisms responsible for the failure of Cu bonds.

In the first part of this work, Al-Cu diffusion couples were fabricated. A Cu plate (bulk) was sputtered with a ~2µm thick Al thin film. This thin film-bulk interdiffusion configuration mimics the one of the wire bonding, while bringing the advantage of surface accessibility and exaggerated IMC growth for more accurate characterizations. Preliminary results after thermal aging under different conditions show that it is not the commonly thought $\gamma$-$Cu_9Al_4$ IMC that is responsible for crack nucleation, but rather a new phase, named $\alpha$' for the sake of this work. Scanning electron microscope (SEM) micrographs clearly show that delamination occurs following the $\alpha$'/Cu interface. X-ray diffraction (XRD) patterns reveal that this phase is based on a face-centered cubic (FCC) structure, very similar to Cu. With a lattice mismatch of less than 2%, it is at this point hypothesized that $\alpha$' grows epitaxially on Cu, producing a compressive-tensile stress situation; misfit dislocations start nucleating after the $\alpha$' layer reaches a critical thickness, where the interfacial strain energy becomes too high for the system to bear. More in-depth XRD analyses, such as d-spacing/lattice parameter evolution in both $\alpha$' and Cu, and Williamson-Hall analysis converge in this direction.

The second part of this work is dedicated to understanding the origin of $\alpha$' formation, its exact crystal structure, as well as its relationship to the Al-Cu phase diagram. Identical diffusion couples were subjected to high temperature thermal treatment and $\alpha$' was found to coexist with other equilibrium phases, such as $\beta$-$Cu_3Al$ and $\gamma$-$Cu_9Al_4$, at given

temperatures on the Cu side of the diffusion couple. Further proofs of its existence were found by high-resolution transmission electron microscope (HRTEM) analyses carried out on the same diffusion couple. Careful analysis and simulations of the selected area electron diffraction (SAED) patterns unmistakably revealed faint and diffuse superlattice reflections corresponding to a $D0_{22}$ crystal structure.

Finally, the last section of the project demonstrates the solid-state epitaxial growth of α' on Cu. A (111) Cu single crystal was sputtered with ~1μm thick Al thin film and aged under controlled atmosphere. XRD investigations in both Bragg-Brentano, and rocking curve (RC) configurations revealed the out-of-plane epitaxial relationship between α' and Cu. In-plane epitaxy was then determined by means of HRTEM cross-section micrographs of the interface, assisted by corresponding FFT computations.

Results reported in the overall investigation brought a comprehensive and plausible way to explain failure mechanisms in Cu wire bonding technology.

Table of Contents

List of Tables

Chapter 1: Introduction & Background

1.1 Industrial & scientific context

1.1.1 Overview of the wire bonding process

The wire bonding technology is the most widely used path to form interconnects between silicon die pads and package leads; it is nowadays used in more than 90% of chip interconnects and continues to grow steadily [1]. Wire bonding is a welding process where two metals, one being a thin wire and one being the Al metallization layer on the pad surface, are brought together using a combination of localized heat, pressure, and/or ultrasonic energy. A thin layer of intermetallic compound (IMC) will develop upon bonding, providing strength and reliability to the bond. The step by step process using the thermal compression technique, and final products are shown in Figure 1.1.
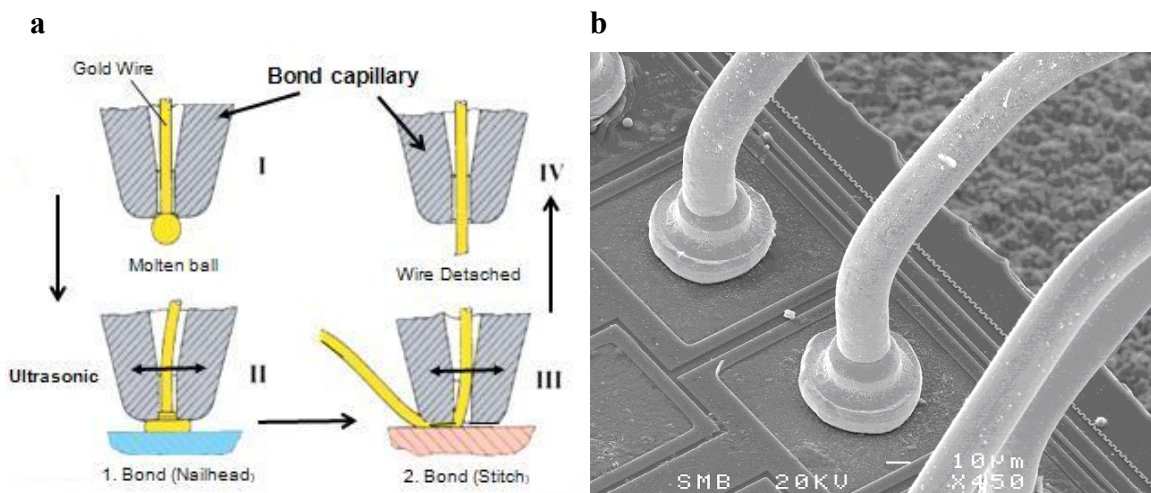


*Figure 1.1 (a) Schematic representation of wire bonding thermal compression process [2], and (b) SEM micrograph of final ball bonds [3].*

The four basic steps of the process are the following [2]:

I. The ball is melted in a hydrogen flame

II. The wire is positioned on top of the substrate, then pressure is applied (Nail head)

III. Capillary is pulled up, positioned on lead frame, and pressure is applied (Stitch)

IV. Capillary tool is pulled up and excess wire is removed

Different types of wire materials are/were used in the integrated circuit (IC) industry. Historically, Al, then Au have been most widely utilized. They are both highly ductile materials, which facilitates the plastic deformation occurring during the bonding step and allows the formation of a strong and durable bond. Their high electrical conductivity at room temperature were also a deciding factor in the decision of implementing them as interconnects. Additionally, Au has exceptional heat transfer and oxidation/corrosion properties, which made it the material of choice for decades. Most often, the purity of the raw wire material is in excess of 99.99% (4N), although sometimes higher impurity content can be beneficial and make the wires more reliable by decreasing the tendency to form IMCs [4].

Several reasons are now pushing IC manufacturers to find alternative bond materials. While Au was for long the natural candidate, owing to its flexibility, its performance limitations and ever-rising cost made it progressively less and less ideal. Figure 1.2 is a chart representing the annual gold price from 1971 until 2013. A sharp and steady price increase began in the early 2000's, with no sign of slowing down. This is one of two main reasons that spurred the need to find a replacement material.
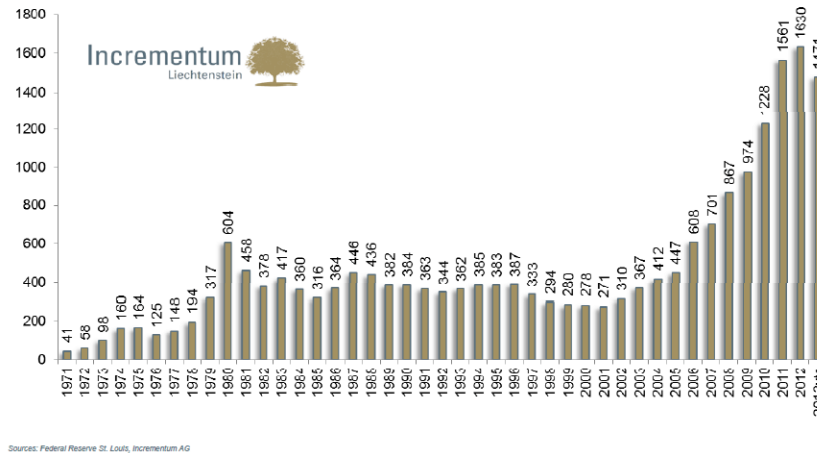
*Figure 1.2 Annual average gold price recorded since 1971 [5].*

Although Au was used for so long and process optimizations arrived at maturation, there is nowadays an emerging need for increased reliability standards in fields where microelectronic devices become more abundant and the consumer safety is at stake. A perfect example of this trend taking root is in the automotive industry: the new ISO-26262 Functional Safety norm. The role of such norms is to address potential hazards caused by the malfunction of embedded electronics in automobiles [6]. Hence, after having postponed the introduction of Cu wires for years, the industry is currently transitioning and the Cu wire bonding technology is gaining traction.

### 1.1.2 Au bond to Al pad: Source of reliability concerns

Since Bell Labs first published in 1957 a manuscript about a new technology called wire bonding [7], an immense number of studies have been performed on Au wire bond [8-16]. According to this substantial database, one conclusion is shared throughout the community; the most important factor leading to failure between Au wire and Al pad is the

3

IMC formation. For a reason that will be covered later, in the Hume-Rothery rules for substitutional solid solution section, Au and Al are prone to forming IMCs at a very fast rate when in contact. Physical properties of IMC can be very different than the parent elements, which can cause several issues. Gold-aluminum IMC formation during the initial bonding, and growth during device operation (about 100°C), are the source of serious issues. $Au_5Al_2$ for example is commonly called the "white plague", as its low electrical conductivity dramatically increases resistivity and can quickly trigger failure. $AuAl_2$, known as the "purple plague" is another problematic intermetallic. Upon nucleating and growing it will tend to contract, causing the creation of voids in the surrounding metal, decreasing both the electrical conductivity and the structural integrity of the bond. Figure 1.3 shows an optical micrograph of Au/Al bond after 500h at 195°C. One can notice the thick IMC layers forming between the ball bond and the Al metallization layer. Fast IMC growth rate and mass flux imbalance engender a lot of vacancy formation. When the material becomes saturated with vacancies, they coarsen and form microscopic voids. These are known as Kirkendall voids, and have disastrous consequences on the bond durability.
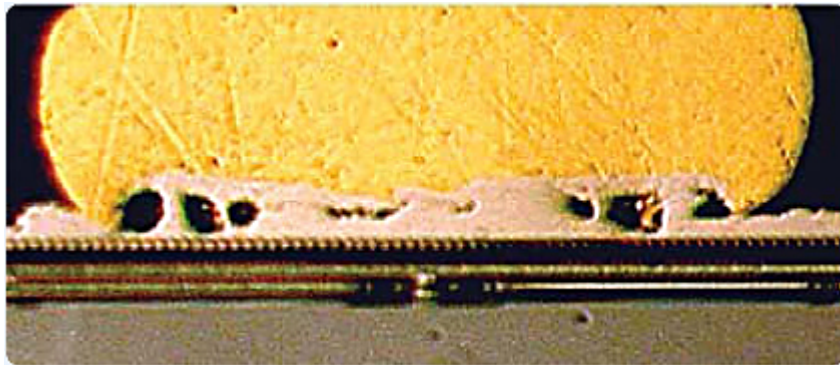


*Figure 1.3 Au bond subjected to a 500h heat treatment at 195°C [17].*

The problem highlighted above is intrinsic to the use of Au as a wire material. Additionally, its use is compromised by the global trend the IC industry has been following in modern times. The economic law known as Moore's law has been shown to perfectly apply to the microelectronic industry: according to Scott E. Thompson et al. review [18], the density and performance of integrated circuits is doubling every two years. Continuous advances in the fields of materials and processes have made Moore's law unrelenting for more than 40 years. This constant miniaturization (scaling) of solid-state devices has had negative influence on their general reliability. As a result, the ever-increasing current density flowing in integrated circuits worsened phenomena such as Joule heating and electromigration, which have a direct consequence on interface reaction and IMC formation in wire bonds.

### 1.1.3 Hume-Rothery rules for substitutional solid solution

A solid solution is formed when atoms from the alloying element (solute), occupy random locations within the lattice of the main constituent (solvent). A substitutional solid solution occurs when the solute atoms occupy the normal lattice sites of the solvent. Substitutional solid solutions generally happen when the atomic radii of both constituent are similar. For example, Cu and Ni are totally miscible over the whole concentration range; they can substitute to each other without any disruption of the base FCC lattice. The renowned scientist William Hume-Rothery, pioneer in the field of metallurgy, set a number of empirical rules predicting the solubility between metallic elements. These rules have proven successful in defining solubility conditions in many systems, and are considered as a solid guideline.

***Rule I. Crystal structure factor:*** The crystal structure of two metallic elements should be the same.

***Rule II. Relative atomic size factor:*** The atomic radii must be rather comparable in order to accommodate to the crystal structure of the solvent:

$$\% \text{ difference} = \left(\frac{r_{solute} - r_{solvent}}{r_{solvent}}\right) \times 100 \leq 15\% \tag{1.1}$$

Extensive solid solubility can only take place when the atoms have a size difference ranging below 15%. Solid solution can still occur for numbers greater than 15%, but solubility limit shall be very limited. The reason for this is that lattice distortions resulting from a higher percentage difference are too important to favor solid solubility. A convincing proof of this Hume-Rothery rule was brought by researchers who used electron theory [19-23]. They showed that the total strain energy in the solid solution can be approximated using the following equation:

$$E = 8 \pi \mu \, r_0^3 \, \varepsilon^2 \tag{1.2}$$

where $r_0$ and $(1+\varepsilon)*r_0$ are the unstrained atomic radii of the solvent and solute atoms respectively, $\mu$ the shear modulus, and $\varepsilon$ is the strain. By choosing values $\varepsilon = 0.15$ and $\mu*r_0^3 = 0.7$ eV, $E = 4k_bT$ at 1000°K. It was further shown by Darken and Gurry (known for the Darken-Gurry maps), that the solubility limit shall remain below 1at.% when the energy surpasses $4k_bT$ per atom [24].

***Rule III. Chemical affinity factor:*** When two elements have a low chemical affinity, they will tend to form extended solid solutions. When the affinity in between two elements is great they will tend to form intermetallic compounds instead. Figure 1.4 shows the periodic table as function of the electronegativity of elements. From this table it becomes clear that the Au-Al system is more prone to the rapid formation and growth of IMCs than the Cu-

Al system. Indeed, Au has an electronegativity of 2.5 on the Pauling scale while Cu has an electronegativity measured at 1.9, and Al at 1.6.

**Pauling Electronegativity Values**

| | | | | | | | | | | | | | | | | | |
|---|---|---|---|---|---|---|---|---|---|---|---|---|---|---|---|---|---|
| 1 H 2.20 | | | | | | | | | | | | | | | | | |
| 3 Li 0.98 | 4 Be 1.57 | | | | | | | | | | | 5 B 2.04 | 6 C 2.55 | 7 N 3.04 | 8 O 3.44 | 9 F 3.98 | |
| 11 Na 0.93 | 12 Mg 1.31 | | | | | | | | | | | 13 Al 1.61 | 14 Si 1.90 | 15 P 2.19 | 16 S 2.58 | 17 Cl 3.16 | |
| 19 K 0.82 | 20 Ca 1.00 | 21 Sc 1.36 | 22 Ti 1.54 | 23 V 1.63 | 24 Cr 1.66 | 25 Mn 1.55 | 26 Fe 1.83 | 27 Co 1.88 | 28 Ni 1.91 | 29 Cu 1.90 | 30 Zn 1.65 | 31 Ga 1.81 | 32 Ge 2.01 | 33 As 2.18 | 34 Se 2.55 | 35 Br 2.96 | |
| 37 Rb 0.82 | 38 Sr 0.95 | 39 Y 1.22 | 40 Zr 1.33 | 41 Nb 1.6 | 42 Mo 2.16 | 43 Tc 1.9 | 44 Ru 2.2 | 45 Rh 2.28 | 46 Pd 2.20 | 47 Ag 1.93 | 48 Cd 1.69 | 49 In 1.78 | 50 Sn 1.96 | 51 Sb 2.05 | 52 Te 2.1 | 53 I 2.66 | |
| 55 Cs 0.79 | 56 Ba 0.89 | 57 La 1.1 | 72 Hf 1.3 | 73 Ta 1.5 | 74 W 2.36 | 75 Re 1.9 | 76 Os 2.2 | 77 Ir 2.20 | 78 Pt 2.28 | 79 Au 2.54 | 80 Hg 2.00 | 81 Ti 1.62 | 82 Pb 2.33 | 83 Bi 2.02 | 84 Po 2.0 | 85 At 2.2 | |
| 87 Fr 0.7 | 88 Ra 0.9 | | | | | | | | | | | | | | | | |

*Figure 1.4 Periodic table as a function of electronegativity [25].*

***Rule IV. Relative valence factor:*** In order to achieve maximum solubility both elements should have the same number of valence electrons. That being said, a metal will more readily dissolve another metal with higher valency than the opposite.

### 1.1.4 Diffusion couple and IMC formation mechanism

Diffusion couples are one of the oldest and most accurate ways to determine phase diagrams and thermodynamically stable phases present at specified temperatures. They have been used for decades in studying phase equilibria in binary and ternary systems. Their use for that purpose is based on the assumption that local equilibrium exists at the interface between each phase included within the diffusion zone. From a thermodynamics

point of view, it means that the chemical potential of all phases involved should perpetually evolve across the diffusion zone, but remain equivalent at both sides of a given interface [26]. It is important to note though that because of the gradient in chemical potential that acts as a driving force, the overall system cannot be at equilibrium during the diffusion process.

A hypothetical diffusion couple subjected to thermal treatment (resulting in one IMC layer), along with its concentration profile is schematically represented in Figure 1.5.
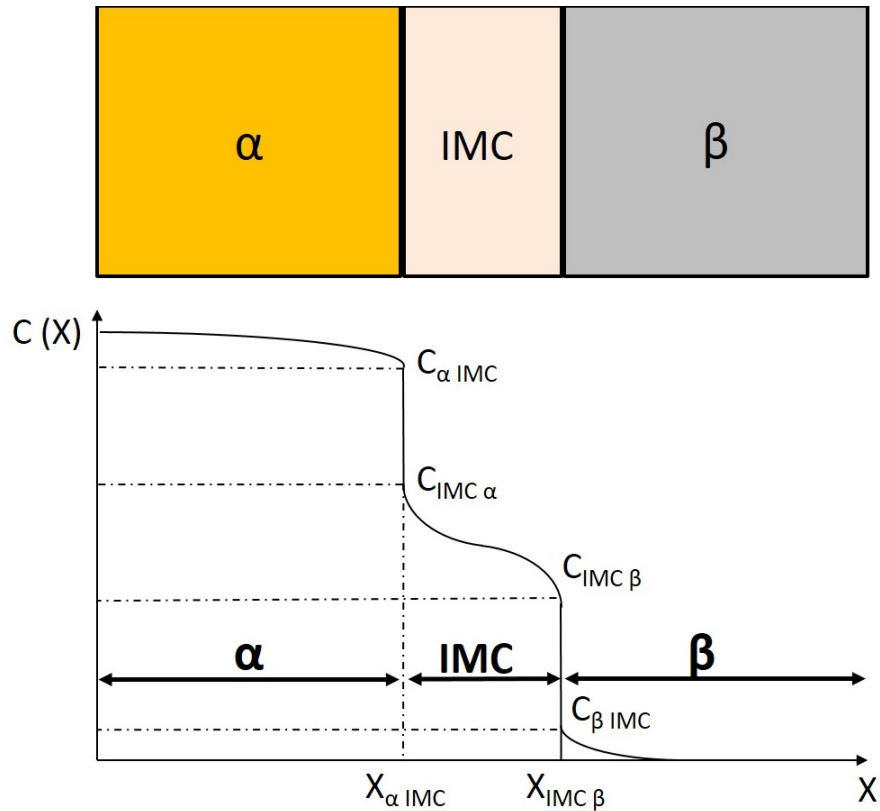


*Figure 1.5 Hypothetical diffusion couple subjected to heat treatment, and corresponding concentration profile. Redrawn from [27].*

It is well known that such a diffusion process can either be governed by diffusion across the newly formed IMC phase, or by the reactions taking place at the different interfaces. In

most cases, the formation and growth of IMCs will result from a combination of both. The general rule is that in very thin layers, diffusion progresses very quickly, so the process is said to be interface reaction controlled. As the thickness of the newly formed products keeps increasing, the diffusion process progressively slows down, and ultimately the kinetics are governed by the so-called diffusion controlled mode [27].

When the diffusion process eventually becomes entirely diffusion controlled, the IMC growth follows a parabolic law, such as:

$$X_{IMC} = K_{IMC} \sqrt{t} \tag{1.3}$$

where $X_{IMC}$ is the IMC thickness, $t$ is the time, and $K_{IMC}$ is the IMC growth constant. Kidson has proven that the growth constant can be expressed as follows [28]:

$$\mathrm{K_{IMC}} = 2 \left\{ \left[ \frac{\widetilde{D}_{\beta\,IMC}\, K_{\beta\,IMC} - \widetilde{D}_{IMC\,\beta}\, K_{IMC\,\beta}}{C_{IMC\,\beta} - C_{\beta\,IMC}} \right] - \left[ \frac{\widetilde{D}_{IMC\,\alpha}\, K_{IMC\,\alpha} - \widetilde{D}_{\alpha\,IMC}\, K_{\alpha\,IMC}}{C_{\alpha\,IMC} - C_{IMC\,\alpha}} \right] \right\} \tag{1.4}$$

where $C_{\alpha\,IMC}$ is the equilibrium concentration on the $\alpha$ side of the $\alpha$/IMC interface, $\widetilde{D}_{\alpha IMC}$ is the interdiffusion coefficient in $\alpha$ phase close to the $\alpha$/IMC interface, and $K_{\alpha IMC}$ is the composition gradient in $\alpha$ close to the $\alpha$/IMC interface. As observed in equation (1.4), the model doesn't take into account various phenomena related to the interface reaction controlled mode, such as the nucleation of IMC, as well as the formation/destruction of vacancies. Therefore, the use of this derivation is only appropriate when the diffusion time is long enough to be governed by the diffusion controlled mode [29].

The formation and growth of IMC during interdiffusion between two metals involves different steps. A supersaturated solid solution is first formed between the two reacting species. Subsequently, the newly formed IMC nuclei tend to grow and connect with other

nuclei along the given interface; heterogeneous nucleation occurs at crystallographic defects such as dislocations and grain boundaries. Further diffusion allows the IMC layer to grow normal to the interface [30]. The nucleation and growth mechanism of an IMC directly depends on both thermodynamic and kinetic considerations [31].

The diffusion theory states that an IMC doesn't form right upon interdiffusion between the two species, but rather after the initial interface goes through an incubation time, necessary for reaching the local equilibrium. Thompson [32] theoretically derived the equation for the incubation time to nucleate the IMC X at the interface between two metals A and B. Considering that diffusion of A in β is quicker than B in α, the equation is as follows:

$$\theta = \frac{2}{9} \frac{\lambda^4 kT}{D} \frac{\sigma_{\beta X}}{\Delta G^2} \qquad (1.5)$$

with

$$\Delta G = \Delta G_v + (\Delta \sigma) \lambda^2$$

and

$$\Delta \sigma = \sigma_{\alpha X} + \sigma_{\beta X} + \sigma_{\alpha \beta}$$

where $\lambda$ is the jump distance, $D$ is the diffusivity, $k$ is the Boltzmann constant, $T$ is the absolute temperature, $\sigma_{\beta X}$ is the interfacial energy at the β / X interface, and $\Delta G_v$ is the energy change per atom resulting from the transformation of β in IMC X. According to Thompson, there is no incubation time in the case where $\sigma_{\beta X}$ is negative. Overall, the incubation time can be disregarded for practical applications as it is always less than a second, regardless of the system [31].

The nucleation rate is defined as the number of nuclei formed per unit volume in unit time. The classical theory of nucleation was developed to understand the precipitation behavior in stoichiometric alloys [33]. The steady-state nucleation rate of a new IMC in an interdiffusion configuration remains fundamentally similar and is given by [31]:

$$N = \frac{A}{\eta} \exp\left[-\frac{b\Delta\sigma^3}{(\frac{\Delta G_d}{V_m})^2 kT}\right] \tag{1.6}$$

where $A$ is a constant, $\eta$ is the dynamic viscosity, $b$ is a parameter considering particle shape and contact angle at both ends of the particle, $V_m$ is the molar volume of the nuclei, and $\Delta G_d$ is the driving force for one mole of atoms of the new IMC. One can notice that the interfacial energy term $\Delta\sigma$ can have a significant influence on the nucleation rate $N$ as it is IMC dependent.

To summarize, IMC phase formation is influenced by several factors including thermodynamic driving force, diffusivity of the elements, temperature and initial contact area. In this regard, the diffusion couple is indeed a very powerful technique that allows the determination of equilibrium phases forming during isothermal heat treatment. The technique has its own drawbacks though. For instance, the end phases (pure elements) might both be solid at the chosen interdiffusion temperature, but intermediate liquid phases might potentially render the analysis of results complicated. Moreover, accelerated reactions in the diffusion zone, resulting from grain boundaries and other crystal defects, might complicate the final analysis. As a consequence, the diffusion couple method would gain in reliability when combined with other accurate phase determination techniques, such as equilibrated stoichiometric alloys, where the precise position of phase field boundaries can be investigated.

## 1.1.5 Interface boundaries in solids

After having introduced the key role of IMC growth on the reliability of the wire bonding technology, as well as the interfacial reactions occurring in interdiffusion, it is now necessary to introduce a few basics about interface boundaries in solids. Solid phases can be joined in different manners across an interface, depending on their crystal structures and compositions. Interfaces can be subdivided into three main categories: coherent, semi-coherent, and incoherent.

***Coherent Interfaces [34]:*** A coherent interface can occur when two distinct lattices are fully continuous along an interface. Put simply, this means that each atom is partially bonded to a "foreign" atom. Coherent interfaces are only possible when two phases have a similar crystal structure and orientation with small lattice mismatch, or when they have a different crystal structure but with a specific orientation that minimizes the interfacial strain. The conventional way of specifying an orientation relationship is by giving the parallel (hkl) planes and parallel directions [uvw] lying in these crystallographic planes in the following manner:

$$(100)_\alpha \text{ // } (100)_\beta \text{ ; } [010]_\alpha \text{ // } [010]_\beta$$

The interface energy $\gamma$ of a coherent interface is governed by the energy increase due to the formation of A-B bonds such as: $\gamma_{coherent} = \gamma_{ch}$. The interface strain term, due to lattice mismatch, is usually neglected for coherent interfaces. These kinds of interfaces have the lowest energy (5-200mJ/m$^2$ [35]), as there are no dangling bonds at the interface, as well as limited lattice distortions. In 1938, Becker [36] was the first to calculate the coherent interface energy between two phases of the same crystal structure; he assumed that the two phases were having a stable composition up to the interface. Using the regular solution

12

model, he showed that the interfacial energy is proportional to the square of the concentration gradient at the interface:

$$\gamma \sim \left(\frac{dC}{dx}\right)^2 \tag{1.7}$$

A hypothetical coherent interface between two phases of same crystal structure is shown in Figure 1.6.
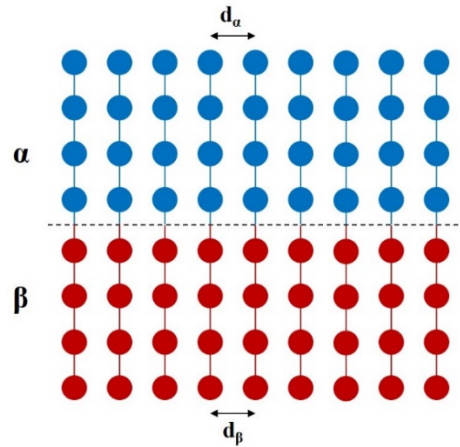


*Figure 1.6 Hypothetical coherent interface between two phases with same crystal structures.*

***Semicoherent Interfaces [34]:*** When the lattice misfit between two phases is larger than in the case of coherent interfaces, or the interface covers a rather large area, it will be energetically favorable for the system to release the long-range strain field by nucleating misfit dislocations (i.e. edge dislocations at the interface). In one-dimension, the lattice can easily be accommodated by introducing misfit dislocations separated by a distance $D$ such as [34]:

$$D = \frac{d\beta}{\delta} \approx \frac{b}{\delta} \tag{1.8}$$

where $d_\beta$ is the interplanar spacing of β phase normal to the interface, $\delta$ is the one-dimensional lattice mismatch, and $b$ is the Burgers vector of the dislocations such as, b=$(d_\alpha+d_\beta)/2$.

In the case of a semicoherent interface, the total interfacial energy must take into account local lattice distortions caused by the misfit dislocations: $\gamma_{semicoherent} = \gamma_{ch} + \gamma_{st}$. It is obvious that the structural component $\gamma_{st}$ shall be proportional to the lattice mismatch. The interfacial energy of semicoherent interfaces is in the range of 200-800mJ/m$^2$ [35]. An example of semicoherent interface is illustrated in Figure 1.7.
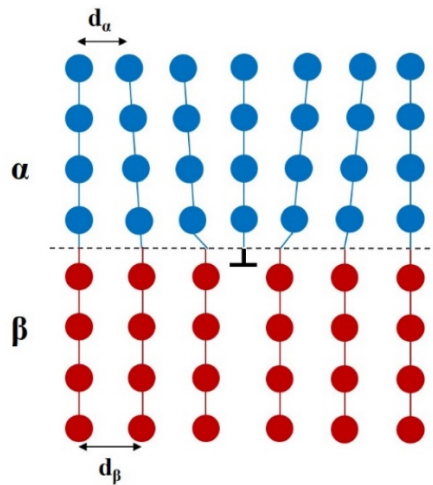


*Figure 1.7 Hypothetical semicoherent interface between two phases of substantial lattice mismatch.*

Included in the semicoherent interfaces are known complex and specific orientation relationships between FCC and BCC phases for example. Such orientation relationships are possible due to similarities in the lattice patterns of dissimilar matching planes. The Kurdjumov-Sachs and Nishiyama-Wassermann are among the most encountered instances of complex orientation relationships. This subject will prove to be of particular interest in this work, hence it will be introduced accordingly later on.

***Incoherent Interfaces [34]:*** Incoherent interfaces occur when there is a total incompatibility in crystal structure, or the lattice mismatch is too large to promote lattice

continuity. Such interfaces are known to behave similarly to high-angle grain boundaries. Incoherent interfaces are commonly found in stoichiometric alloys undergoing precipitation, as well as in interdiffusion conditions. The interfacial energy in this case is very large (800-2500mJ/m$^2$ [35]), as there is no lattice continuity whatsoever. Figure 1.8 shows a typical incoherent interface.
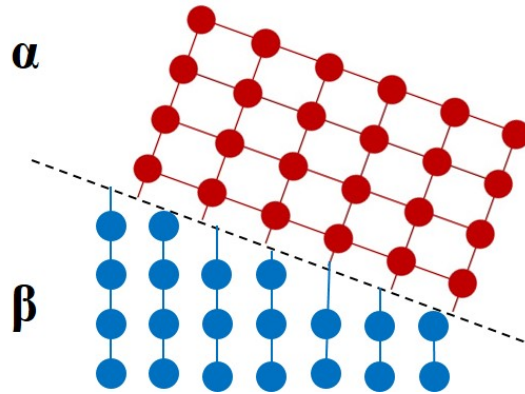


*Figure 1.8 Hypothetical incoherent interface between two phases randomly oriented.*

1.2 The Aluminum-Copper system

1.2.1 The Al-Cu phase diagram

The Al-Cu system has been one of the most widely studied binary systems for almost a century. Al-rich alloys remain tremendously important in many key industries, such as the aerospace and transportation industries. From a more scientific aspect, the early stage precipitation of Guinier-Preston zones (GP zone) resulting from age hardening, is considered as one of the most fundamental concepts in metallurgy. Cu-rich alloys have been primarily investigated for their shape memory properties, and aluminum bronze is still massively utilized as structural components in naval and aerospace industries, where their strength and excellent corrosion/oxidation resistance is needed. While abundant data

is available for these alloys and applications, the recent introduction of Cu as a wire material in wire bonding urged the need to assess the feasibility and long-term efficiency/reliability of this process, very different from past Al-Cu applications.

Most recent assessments of the Al-Cu equilibrium phase diagram were carried out by Murray in 1985 [37], then by Ponweiser et al. in 2011 [38]. A redrawn Al-Cu phase diagram is shown in Figure 1.9.
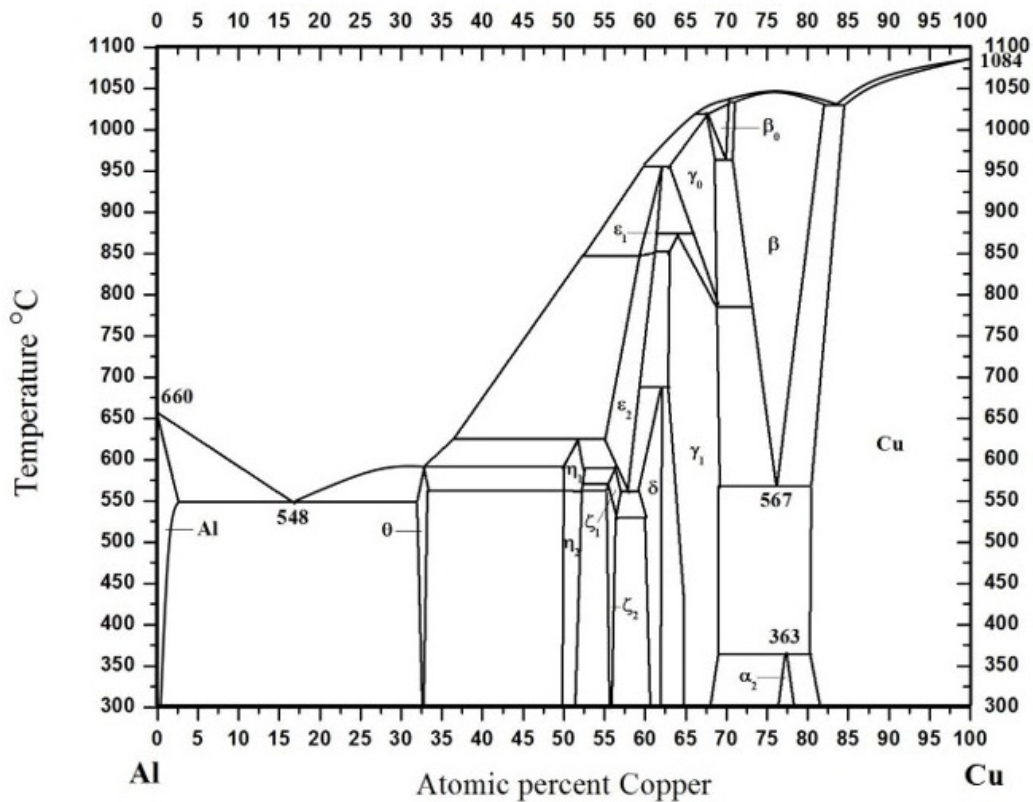


*Figure 1.9 A redrawn Al-Cu equilibrium phase diagram, according to Murray [37].*

According to the phase diagram shown in Figure 1.9, 6 IMCs are shown to exists at temperatures below ~363°C; $\theta$-$Al_2Cu$, $\eta$-CuAl, $\xi$-$Cu_4Al_3$, $\delta$–$Cu_3Al_2$, $\gamma$-$Cu_9Al_4$, and $\alpha_2$-$Cu_3Al$, listing from the Al-rich end. Additionally, 7 other IMC can form at high

temperature, but are not stable at the ambient. Table 1.1 provides structural data on all existing IMCs.

*Table 1.1 Structural data on IMC in the Al-Cu system.*

| | Pearson Symbol | Space group | Lattice constants (Å) | Composition [37] (in at.% Cu) | Reference |
|---|---|---|---|---|---|
| Al | cF4 | Fm-3m | a = 4.04 | 0-2.48 | [39] |
| $\theta$-CuAl$_2$ | tI12 | I4/mcm | a = 6.06<br>c = 4.87 | 31.9-33 | [40] |
| $\eta_1$ | oP16 / oC16 | Pban / Cmmm | a = 4.08<br>b = 12.00<br>c = 8.63 | 49.8-52.4 | [41,42] |
| $\eta_2$-CuAl | mC20 | C2/m | a = 12.06<br>b = 4.10<br>c = 6.91<br>β = 55.04° | 49.8-52.3 | [43] |
| $\xi_1$-Cu$_4$Al$_3$ | oF88 | Fmm2 | a = 8.12<br>b = 14.49<br>c = 9.99 | 55.2-59.8 | [44] |
| $\xi_2$-Cu$_4$Al$_3$ | oI24-3.5 | Imm2 | a = 4.09<br>b = 7.03<br>c = 9.97 | 55.2-56.3 | [45] |
| $\epsilon_1$ | cubic? | ? | | 59.4-62.1 | [46] |
| $\epsilon_2$ | hP4 | P6$_3$/mmc | a = 4.14<br>c = 5.06 | 55-61.1 | [43] |
| $\delta$-Cu$_3$Al$_2$ | hR52 | R3m | a = 8.70<br>α = 89.74 | 59.3-61.9 | [47] |
| $\gamma_0$ | ? | I-43m | ? | 59.8-69 | [48] |
| $\gamma_1$-Cu$_9$Al$_4$ | cP52 | P-43m | a = 8.70 | 62.5-69 | [49] |
| $\beta_0$ | ? | ? | ? | 67.6-70.2 | / |
| β-Cu$_3$Al | cI2 | Im-3m | a = 2.95 | 70.6-82 | [50] |
| $\alpha_2$-Cu$_3$Al | tI8 | I4/mmm | a = 3.66<br>c = 7.33 | 76.5-78 | [51] |
| Cu | cF4 | Fm-3m | a = 3.61 | 80.3-100 | [52] |

The investigations leading to constant updates in phase diagrams are based on thermodynamic calculations (CALPHAD method). They also heavily rely on a combination of experimental data using differential thermal analysis (DTA) on stoichiometric alloys, and diffusion couples characterized with X-ray diffraction (XRD), scanning electron microscopy (SEM) / energy dispersive spectroscopy (EDS), and transmission electron microscopy (TEM).

## 1.2.2 The Al-Cu system in wire bonding configuration

There are several advantages in using Cu over Au as a wire material in the wire bonding process. First of all, Cu wires are considerably cheaper in terms of costs. Moreover, Cu has significantly better mechanical properties (stiffness / rigidity), electrical conductivity, and high thermal conductivity. These intrinsic qualities make Cu a more suitable candidate for fine-pitch bonding. Finally, its lower reaction rate when in contact with Al results in slower IMC growth and improved long-term reliability.

Interdiffusion in the Al-Cu system has been the subject of a considerable amount of work in recent times. The existence of a sizable database provides a good global understanding of the diffusion mechanisms under various conditions [53-56]. The main issue usually encountered in the Al-Cu pair as a structural material is the formation and growth of IMCs, resulting in interface defects that compromises their mechanical integrity. When it comes to Cu wire bonding, recent investigations suggested that failure also results from the growth of IMCs between the Cu ball bond and the Al thin film metallization layer [57,58]. However, the wire bonding configuration makes the characterization of the several thin IMC layers tricky and sometimes deceiving. As a result, many unanswered questions

remain regarding the intermetallic phases present at the interface, as well as their thickness and overall role they play in the failure of Cu bonds. For instance, all investigations on Al-Cu interdiffusion state that only 5 IMCs exist in the equilibrium phase diagram, and constantly forget to mention the existence of $\alpha_2$-$Cu_3Al$ at appropriate temperatures. This $\alpha_2$-$Cu_3Al$ is the most Cu-rich IMC known thus far (see phase diagram in Fig. 1.9), and was described as being a one dimensional long-period superlattice (LPS) based on the $D0_{22}$ crystal structure [59]. The tetragonality component of the $D0_{22}$ structure is so small in the case of $\alpha_2$-$Cu_3Al$, that it could be approximated as the ordered FCC-based $L1_2$, for the sake of simplification. To the best of my knowledge, only one team of researchers recently casually suggested its formation in contact to Cu in Cu-Al wire bonding [60]. Constant failure to mention its existence resulted in the wrongful assumption that $\gamma$-$Cu_9Al_4$ is the most Cu-rich IMC. It is especially important to acknowledge $\alpha_2$-$Cu_3Al$ potential formation as delamination was, in most cases, reported to be caused by $\gamma$-$Cu_9Al_4$ at the interface with Cu. Figure 1.10 shows a SEM micrograph of a failed Cu ball bond where a crack can clearly be seen at the Cu-rich IMC/Cu interface. Consequently, the determination of the terminal IMC is primordial if one wants to understand the underlying failure mechanisms.
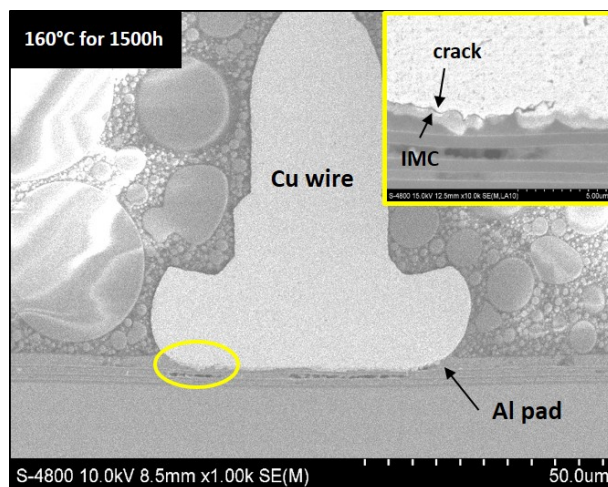


*Figure 1.10 Failed Cu-Al wire bond. SEM. (UTA Electronic Materials Laboratory)*

Researchers' lack of success in being able to discover whether $\alpha_2$-$Cu_3Al$ forms may come from its structural similarity with Cu. Figure 1.11 represents the crystallographic modeling of Cu (FCC) and $\alpha_2$-$Cu_3Al$ ($L1_2$ / $D0_{22}$) to emphasize their similarities. With a lattice mismatch below 2%, very careful diffraction analysis combined with advanced microscopy techniques would be mandatory in order to detect it in such limited thickness.



**FCC**          **L1$_2$**          **D0$_{22}$**
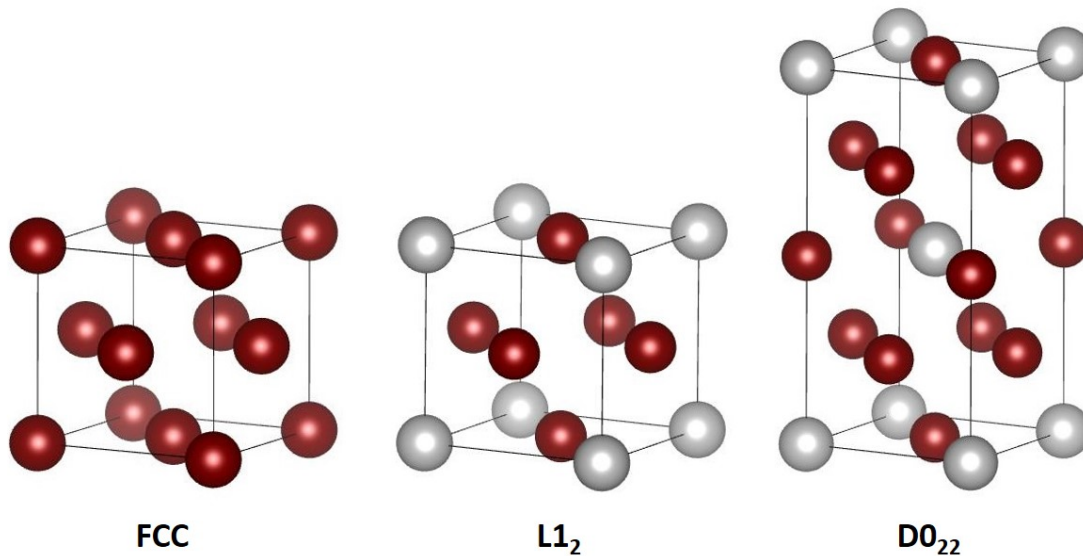
*Figure 1.11 Crystal structures of Cu (FCC) and $\alpha_2$-$Cu_3Al$ ($L1_2$ / $D0_{22}$). Red atoms are Cu and grey atoms are Al. Drawings produced by VESTA [61].*

1.3 Objectives of this research and organization of this dissertation

As previously mentioned, the need to find a replacement material for Au wires is becoming a primary concern for the microelectronic industry. Cu already proved to be a more suitable material due to its superior physical properties, leading to better long-term reliability prospects. However, the failure mechanisms related to the implementation of Cu as a wire material are not yet totally understood. As a matter of fact, the many

inconsistencies reported in the available literature make the overall understanding of the interface degradation blurry at best.

Consequently, led by the urge of gaining a better understanding of interface failure in Al-Cu interdiffusion, we proceeded in fabricating several configurations of diffusion couples, including the one mimicking the wire bonding process. Characterization of IMC formation and growth proved to be a very difficult task, even considering the availability of modern analytic and microscopic tools. After a substantial amount of trial and error, it was decided that a 2μm Al thin film coated on a Cu bulk plate, associated with elevated interdiffusion temperatures, was the best way to promote and characterize IMC layers. This thin film-bulk configuration allows x-ray penetration in the diffusion zone, making possible to trace phase kinetics and development of interfacial strain between the different IMC layers.

Research carried out in Chapter 3 suggests that $\gamma$-$Cu_9Al_4$ is not the terminal phase at the Cu-rich end of the diffusion couple, but rather an unknown phase, that we named $\alpha'$. This IMC is structurally very close to $\alpha_2$-$Cu_3Al$ but proved to be stable at diffusion temperatures as high as 450 $^o$C. Careful XRD analysis of interface strain development at the $\alpha'$/ Cu interface shows that this new IMC is responsible for crack nucleation and delamination. Our conclusions are in good agreement with other research that suggest that crack almost always develop at most Cu-rich IMC/Cu. Chapter 4 is dedicated to determining the crystal structure of this new $\alpha'$ phase, along with its relationship to the equilibrium phase diagram. It is shown that this phase coexists with the equilibrium phases $\beta$-$Cu_3Al$ and $\gamma$-$Cu_9Al_4$ at very high temperatures (up to 625$^o$C) on the Cu side of diffusion couples. Subsequent in-depth HRTEM analysis demonstrate that the new IMC has a $\alpha_2$-

like $D0_{22}$ crystal structure. In light of these results, its formation mechanism will be discussed. In Chapter 5, the failure mechanisms suggested in Chapter 3 will be highlighted. A Cu (111) single crystal bulk was coated with 1μm Al thin film and subjected to high temperature heat treatment. XRD rocking curve measurements, coupled with SAED pattern analysis definitely proved that $\alpha'$ grows epitaxially on the Cu (111) substrate. The interfacial strain build-up, misfit dislocation nucleation, and relaxation phenomenon leading to delamination will be discussed in detail. Finally, conclusions to this project will be drawn, and future work planned accordingly.

Chapter 2: Characterization techniques for IMC phase determination

In this chapter, basic concepts related to the main characterization tools used in this study will be covered. Analytical and microscopy techniques are of fundamental importance to this project in order to get both structural and morphological information on IMC phase formation, and resulting stress development. Consequently, an appropriate introduction explaining the theory and the interpretation of results was deemed necessary.

## 2.1 X-ray diffraction

X-ray powder diffraction technique, using a Bragg-Brentano theta-2theta configuration is a key analytical technique in unknown phase determination. Simply explained, a XRD pattern is a plot of the count of x-rays that were scattered by a sample at different $2\theta$ angles. It relies on the theory that photons (x-rays) of specific wavelength will diffract when shined through a crystal. Powder XRD is based on the constructive interference between an incoming monochromatic x-ray beam and the crystal analyzed. The diffraction occurs when Bragg's law is satisfied:

$$n\lambda = 2d \sin \theta \qquad (2.1)$$

This fundamental equation relates the x-rays wavelength $\lambda$, the interplanar spacing $d$ and the diffraction angle $\theta$. $n$ shall be a positive integer, meaning that the scattered waves from different atomic layers are perfectly in phase and the diffraction process can occur. It is also important to point out that the wavelength $\lambda$ and the interplanar spacing $d$ have to be of the same order of magnitude. Bragg's law wouldn't have a meaningful mathematical

outcome beyond: $\lambda < 2d$, since sin θ is always less than 1. Figure 2.1 shows the typical setup used in powder diffraction configuration.
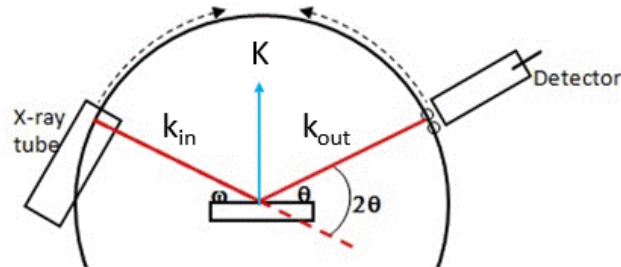


*Figure 2.1 Typical Bragg-Brentano geometry for powder XRD.*

Where ω is the angle between the incident x-ray beam and the sample surface, *2θ* is the diffraction angle, and *K* is the reciprocal lattice vector. The German physicist Max Von Laue proved that the diffraction condition in the reciprocal space is: $K = k_{in} - k_{out}$. As a matter of fact, Bragg and Von Laue diffraction conditions are identical. In the Bragg Brentano configuration ω is always fixed as ½ 2θ, and K is always perpendicular to the sample surface. This means that only lattice planes parallel to the sample surface will diffract and add to the x-ray intensity. The sample is typically analyzed over a wide range of 2θ angles, so all the different planes of the lattice can be reached. In a powdered sample displaying randomly oriented grains, the probability that all diffraction planes will produce diffracted x-rays should be equal. That's the reason why this method is widely used to determine the crystal structure of unknown materials.

Considering a cubic crystal structure, it is possible to relate the interplanar spacing *d* to the lattice parameter *a* and the Miller indices *hkl* for a given plane, by following the simple equation:

24

$$d_{hkl} = \frac{a}{\sqrt{h^2+k^2+l^2}} \quad\quad\quad (2.2)$$

Because only knowing the position of peaks is not enough in order to identify an unknown

phase, the Structure factor ($F_{hkl}$) is an important parameter to take into consideration. It is

defined as the resultant of the waves scattered by all the atoms in the unit cell:

$$F_{hkl} = \sum_i^N f_n e^{-2\pi i(hu_i+kv_i+lw_i)} \quad\quad\quad (2.3)$$

Where $f$ is the atomic scattering factor, and $N$ represents the number of atoms per unit cell.

The Structure factor basically estimates the level of wave interference and therefore varies

depending on the crystal structure and the positioning of dissimilar atoms in the crystal.

From this interference information, it is thus possible to identify the crystal structure of an

unknown phase. The Table 2.1 combines possible Miller indices allowing diffraction in the

case of cubic crystal structures:

*Table 2.1 List of Miller indices that yield diffraction signal in cubic structures*

| | Cubic | | | |
|---|---|---|---|---|
| $h^2 + k^2 + l^2$ | Simple | BCC | FCC | DC |
| 1 | 100 | | | |
| 2 | 110 | 110 | | |
| 3 | 111 | | 111 | 111 |
| 4 | 200 | 200 | 200 | |
| 5 | 210 | | | |
| 6 | 211 | 211 | | |
| 7 | FORBIDDEN NUMBER | | | |
| 8 | 220 | 220 | 220 | 220 |
| 9 | 300 | | | |
| 10 | 310 | 310 | | |
| 11 | 311 | | 311 | 311 |
| 12 | 222 | 222 | 222 | |
| 13 | 320 | | | |
| 14 | 321 | 321 | | |
| 15 | FORBIDDEN NUMBER | | | |
| 16 | 400 | 400 | 400 | 400 |

By rearranging the Bragg's law we obtain:

$$h^2 + k^2 + l^2 = (\frac{2a}{\lambda})^2 \sin^2 \theta_B \qquad (2.4)$$

We now have a way to determine the crystal structure of a cubic phase, by taking the ratio of this equation to the 1$^{st}$ peak:

$$\frac{(h^2+k^2+l^2)_n}{(h^2+k^2+l^2)_1} = \frac{\sin^2 \theta_{Bn}}{\sin^2 \theta_{B_1}} = r_n \qquad (2.5)$$

The ratio $r_n$ will depend on the crystal structure of the sample.
- For Simple Cubic (SC): $r_n$ = 1,2,3,4,5,6,…
- For Body-Centered Cubic (BCC): $r_n$ = 1,2,3,4,6,…
- For Face-Centered Cubic (FCC): $r_n$ = 1, 4/3, 8/3,…

If the material studied using powder XRD is a single crystal, some of the guidelines mentioned above cannot be taken into consideration. As only the planes parallel to the sample surface can satisfy the diffraction condition, many planes will not diffract at all. Let's take the example of a Cu (FCC) single crystal grown following (111). It means that the only family of planes normal to the surface are {111}. On a XRD pattern this means that only (111), (222), etc…will ever diffract. Other planes characteristic of a randomly oriented FCC crystal structure will therefore not produce any intensity. While powder XRD is very efficient in studying polycrystalline materials, it is not the most suitable way to investigate single crystals. For instance, ductile materials such as monocrystalline metals are not defect-free and slight misorientation is common. Valuable data related to the degree of misorientation (=quality) in a single crystal, or the epitaxial relationship of thin films with respect to a substrate, cannot be determined using conventional powder XRD

configuration. Instead, a powerful XRD technique known as rocking curve (RC) measurement is commonly employed.

RC measurements are primarily important in lattice matched thin films, where they can be used to detect misfit dislocation density and mosaic spread (misorientations). Additionally, values related to the layer thickness and relaxation phenomenon can also be gained. The RC data is recorded by "rocking" the sample around a known $2\theta$ angle, corresponding to the diffraction peak of interest. The $2\theta$ angle is fixed while the $\omega$ angle continuously changes over a small angular range, recording the x-ray counts at values slightly off the ideal diffraction conditions. The orientation of the reciprocal lattice vector K varies, while its magnitude remains unchanged. In practice, this is equivalent to a theta scan. The Figure 2.2 shows the typical RC geometry.
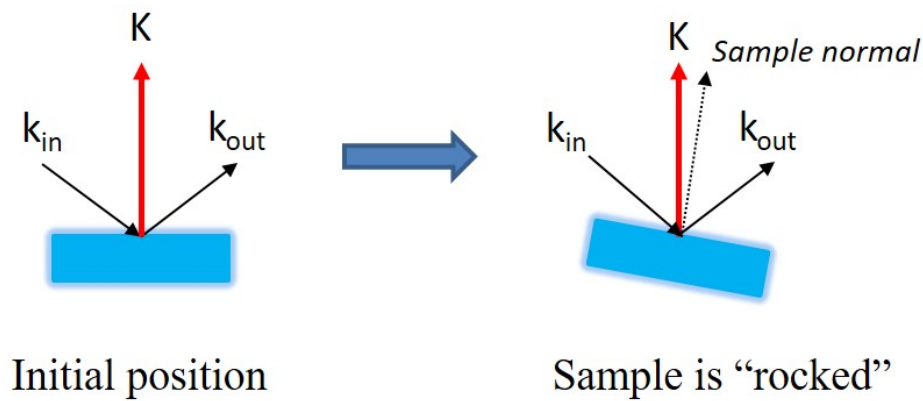


*Figure 2.2 Typical geometry in a RC measurement.*

In a perfect crystal, the resulting peak would be sharp and narrow, not deviating from the ideal diffraction condition. The crystallographic direction and the diffraction vector should be parallel. The only factor leading to peak broadening would inevitably come from instrument broadening. In reality though, anisotropic strain due to crystallographic defects

such as dislocations, mosaicity, and chemical heterogeneities cause the peak to broaden and add diffuse scattering. The mosaicity contribution (in degrees) can be approximately determined by taking the Full Width at Half Maximum (FWHM) of the peak. Hirsch [62] showed that the dislocation density can be reasonably estimated using:

$$\rho = \frac{\beta^2}{9b^2} \tag{2.6}$$

Where $\rho$ is the dislocation density in $cm^{-2}$, $\beta$ is the broadening of the rocking curve in radians, and $b$ is the Burgers vector in cm.

Two diffractometers were used in this work: a Siemens D500 (Bragg-Brentano), and a Bruker D8 Advance (Bragg-Brentano, RC) using a copper x-ray source, Cu $K_\alpha$ with a wavelength of 1.54 Å. Figure 2.3 shows the latter.
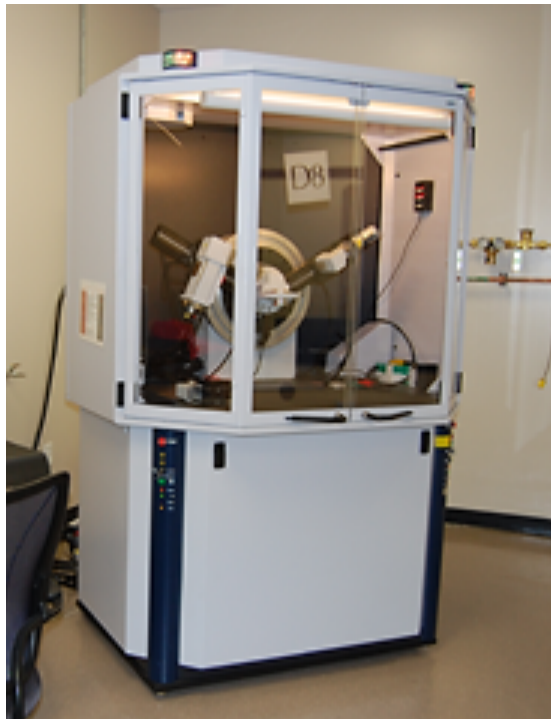


*Figure 2.3 Bruker D8 Advance diffractometer used in this work.*

## 2.2 Scanning Electron Microscope and Energy Dispersive Spectroscopy

The Scanning Electron Microscope, first introduced in 1965, quickly became an essential characterization tool for engineers and scientists of all kinds. Its versatility, affordability, and high capabilities are among the reasons explaining its success. The SEM can be considered as the perfect tool sitting between basic optical microscopes, and expensive transmission electron microscopes.

A SEM is composed of three main components: the electron source, the lens system, and finally the imaging system. The electron source is typically made out of tungsten (W) or lanthanum hexaboride ($LaB_6$) filaments. These filaments produce an accelerated high-density electron beam directed towards the sample. The acceleration voltage is usually in the range 5-40 KV. The resolution becomes higher when increasing the acceleration voltage, leading to a decrease in the wavelength of the accelerated electron beam. The lens system is made of three different kind of lenses: condenser lenses (CL), scanning coils, and objective lenses (OL). First, the condenser lenses are utilized in order to converge the electron beam and have a direct influence on the spot size (beam size at the sample surface). Then, the scanning coils redirect the electron beam on a two-dimension coordinate system (raster). Finally, the main role of the objective lenses is to focus the beam onto the sample. Figure 2.4 illustrates the inside of a SEM column.
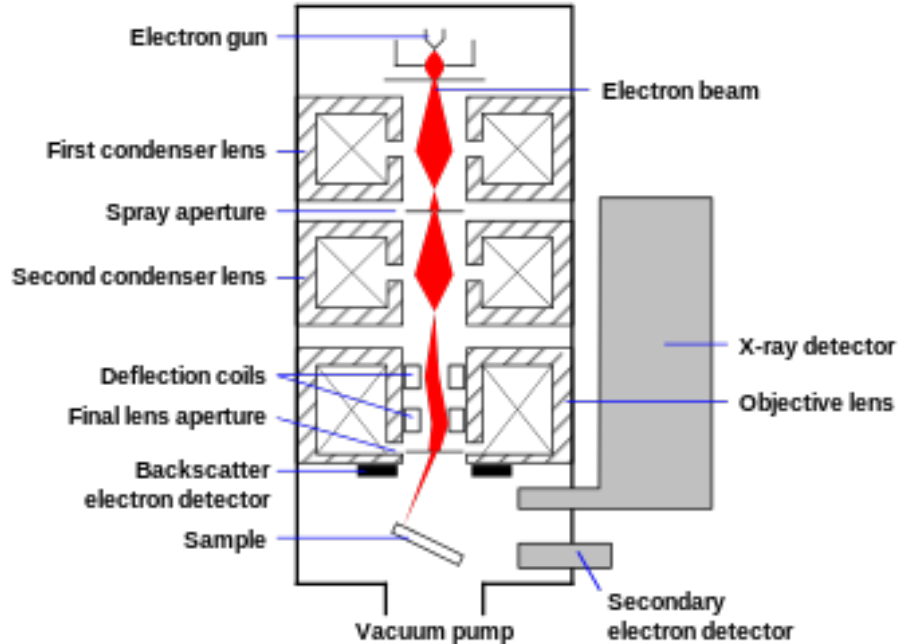
*Figure 2.4 Schematic cross-section of a SEM column [63].*

Several different kinds of interactions occur when the electron beam reaches the sample. Two main imaging modes emerge from these interactions. The first and most widely used is: Secondary Electron Imaging (SE). SE results from inelastic scattering of the incident electron beam with the sample surface. Electrons of the valence band of the sample don't need much energy to be ejected from their shell into the vacuum. Meanwhile, the incident electron beam carries highly energized electrons. Therefore, if one of these electrons coming from the probe hit a valence electron, it will knock it out of its shell. When these electrons are close enough from the surface of the sample (less than 10 nm), they can be collected by the SE detector. Secondary electrons have a weak energy of less than 100 eV. The generation of SE will form an SEM image displaying the surface features of a given sample. Because of the low energy of SE, this imaging mode is only useful for topographic and morphological purposes.

30

Secondly, the Backscattered Electron Imaging (BSE) mode is the result of elastic scattering of incident electron beam with the sample. When the incident electron beam collides with the nucleus of an atom from the sample, this same electron bounces back out as a backscattered electron. These electrons penetrate deeper in the sample, up to 100 nm, and have a high energy compared to secondary electrons. The number of backscattered electrons emitted and collected by the BSE detector depends on the atomic number of elements composing the sample. This is how the contrast is formed in BSE mode. The heavier an element is, the brighter it will appear on the SEM image. This is commonly called "composition mode".

Overall, many particles and waves are emitted by the specimen surface after interaction with the electron beam. They are schematically illustrated in Figure 2.5.
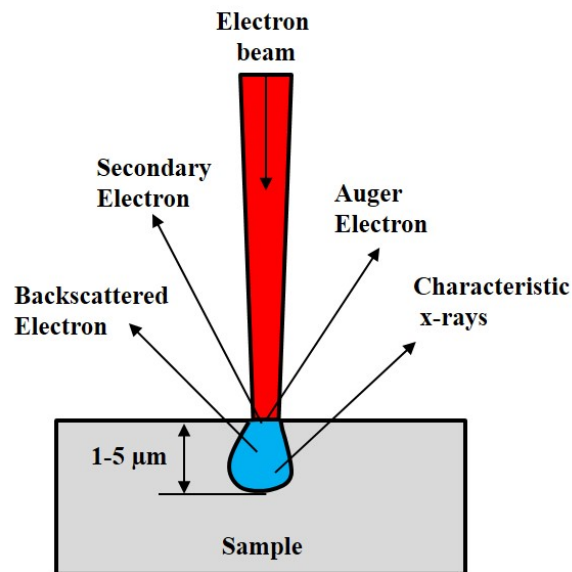


*Figure 2.5 Representation of the many interactions between the electron beam and the sample surface.*

When SEM is combined with other analytical instruments, several other information can also be extracted from the interaction between incident electron beam and sample

surface. Among them, Auger electrons are typically used in order to determine the surface chemistry of samples, and cathodoluminescence is useful in examining the internal structure of various materials. Energy dispersive spectroscopy is probably the most sought-after SEM addition amongst them all. An EDS analysis allows one to quantitatively identify the elements present in the sample in either atomic or weight percentage. Upon interaction with the probe, the elements contained in the sample will release characteristic x-ray (electronic reconfiguration). On the resulting x-ray spectrum, the x-axis shows the energy level of characteristics x-ray emitted, while the y-axis displays the number of x-rays counted by the EDS detector. Compositional mapping and line profile are other useful features of the EDS chemical analysis.

A Hitachi S-3000N Variable Pressure SEM equipped with a tungsten filament as electron source was employed in this research project. It is pictured in Figure 2.6.



*Figure 2.6 Hitachi model S-3000N SEM*

## 2.3 Transmission Electron Microscope

The transmission electron microscope was first invented by German researchers Max Knoll and Ernst Ruska in 1931, and remains to this day the "ultimate weapon" for many scientists across various disciplines. A TEM is typically utilized to investigate materials at the atomic scale by allowing ultra-high magnification, often exceeding a million time. Such magnification can be attained by using electrons as illumination source, accelerated at voltages ranging between 120 and 400 kV. The infinitely small de Broglie wavelength of these electrons (ex: 1.96 pm at 300kV) makes the resolution of a TEM theoretically unlimited. In reality, spherical aberration caused by the electron optics has long been limiting the actual spatial resolution of TEMs. Nonetheless, constant progress in the field of electron microscopy led to the conception of aberration corrected TEMs with sub-angstrom spatial resolutions [64].

In TEM, the highly-energized electron beam is transmitted through the sample. An image is formed from the interaction between the electron beam and the specimen. This image is then focused, magnified, and projected onto a fluorescent screen. A TEM is composed of the electron gun and the lens system. Similar to a SEM, the filament is made of W or $LaB_6$. The gun, being connected to the high voltage source, will emit electrons in the high vacuum via thermionic or filed emission. Since glass lenses would perturbate the electron beam, TEM uses electromagnetic lenses instead. From the top down, the condenser lenses are used to gather the electron, form the beam, and illuminate the area of interest of the sample. The spherical aberration is decreased by a condenser aperture which eliminate high-angle electrons. The objective lens is the most critical lens in TEM, as it is

the first-stage lens used to form the image after the interaction between the beam and the sample. To focus the sample, the focal length of the objective lens has to be adjusted. The contrast can be greatly improved by placing an objective aperture that will select the electrons contributing to form the image. The initial image is then magnified by the intermediate lens. This lens moves to either focus on the image formed with the objective lens (imaging mode), or the diffraction pattern formed in the back focal plane of the objective lens (diffraction mode). The intermediate-lens aperture is inserted to select a small area of the sample while operating in diffraction mode. This is commonly known as SAED (Selected Area Electron Diffraction). Finally, the projector lenses are used to further magnify the image. The Figure 2.7 represents the simplified layout of a TEM column.
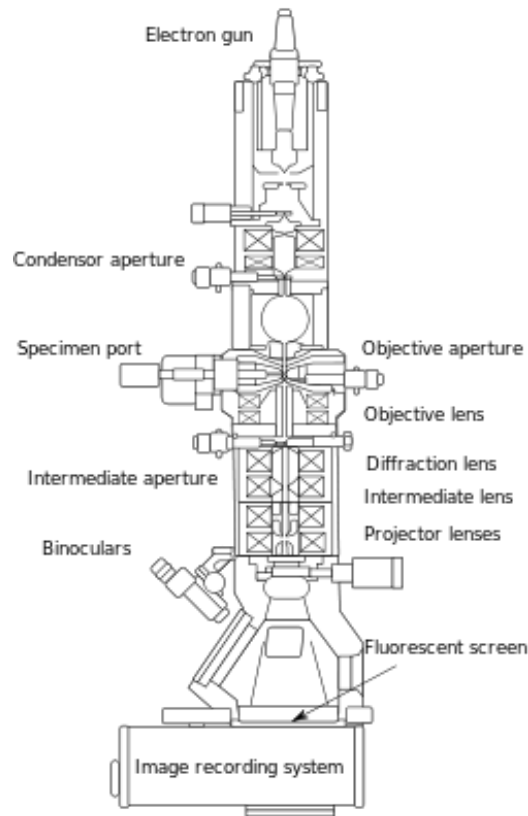


*Figure 2.7 Layout of a basic TEM column [65].*

The contrast in TEM imaging mode is dominated by diffraction contrast. In the Bright Field (BF) imaging mode, the objective aperture is positioned in the back focal plane of the objective lens, so only the transmitted beam is allowed to go though. In the BF mode the intensity change is determined by the weakening of the transmitted beam after interaction with the specimen with respect to the crystal orientation. Local perturbation in the lattice, such as precipitates, crystalline defects, strain, and thickness change will appear darker. In the Dark Field (DF) imaging mode, the transmitted beam is obstructed by the objective aperture, while one (or many) diffracted beam is allowed to go through. Diffracted beams are elastically scattered by the sample, hence valuable information about precipitates, dislocations, stacking faults, and other microstructural features can be obtained. As microstructures in TEM samples are sometimes difficult to analyze and may contain many artifacts, combining BF and DF images is key to extracting accurate information. The diffraction pattern (DP or SAED) mode is reminiscent of the XRD theory. Incoming electrons are elastically scattered upon interaction with the specimen, and diffraction occurs when Bragg's law is satisfied. The TEM SAED mode can be thought as a XRD pattern with superior spatial resolution. The resulting SAED can yield a ring pattern in case of polycrystalline materials, or spot pattern in case of single crystal. SAED patterns contain structural information and are of critical importance in analyzing orientation relationship between phases (ex: matrix and precipitates).

In this work, TEM characterizations were performed in collaboration with the School of Advanced Materials Science & Engineering, Sungkyunkwan University, Suwon, Korea. The TEM apparatus used was a JEOL JEM-ARM200F aberration-corrected scanning transmission electron microscope (STEM) operating at 200kV.

Chapter 3: IMC Growth & Crack Nucleation in Cu-Al Diffusion Couple

*Some of the work presented in this chapter was previously published in the Journal of Electronic Materials, January 2018, Volume 47, Issue 1, pp 855-865.*

## 3.1 Introduction

As stated in the introduction, the understanding of the mechanism dictating crack nucleation in Al thin film Cu bulk diffusion couple remains inconclusive. Even though a substantial database exists, many disagreements concerning the formation sequence of IMC phases, their formation energy, and their role in interface failure, undermine the global comprehension. Strikingly, most manuscripts claim that the Cu-rich IMC $\gamma$-$Cu_9Al_4$ is the terminal IMC and is accountable for interface failure, but fail to mention the potential existence of $\alpha_2$-$Cu_3Al$. Consequently, we saw a need for a comprehensive re-investigation of Cu-Al diffusion couple.

For this purpose, diffusion couples consisting of a Cu plate coated with an Al thin film were fabricated. This simulative configuration has various advantages over the wire bonding configuration. First, the free surface allows accurate IMC phase characterization by XRD within the diffusion zone. Then, the exaggerated IMC growth makes phase identification by SEM cross-section analysis less prone to error. Interdiffusion specimens were subjected to aging temperatures ranging between 350°C-450°C, for various durations of time. Experimental data presented hereafter is taken from 400°C and 450°C interdiffusion studies using a recrystallized stress-free Cu substrate because it provides the clearest evidence to support our conclusions.

## 3.2 Methodology

The samples used for the interdiffusion experiments were based on pure Cu plates coated with 2µm thick Al thin films.  The raw copper plate was a hot-rolled half hard Cu plate, having a 1-mm thickness, and a purity exceeding 99.95%. The as-received material was subjected to heat treatment at 500ºC for 1h in order to relieve internal stress and stabilize the grain structure through the recrystallization process. It is well agreed that 500ºC is well within the recrystallization range for Cu. Preliminary characterizations carried out by electron back-scattering diffraction (EBSD) on as-received and heat-treated specimens showed that these recrystallization conditions made the Cu plate free of textured grain. The mean grain size after treatment was measured to be ~25µm. It was therefore assumed that the hot-rolled Cu plate was free of texture or resulting crystal defects that could bias the diffusion process. After mechanical polishing and lapping to 0.3mm, the Cu plate was placed in a AJA ATC Orion Series UHV (ultra-high vacuum) sputtering system for the deposition of a 2µm thick Al film. The UHV sputtering system prevented the potentially dreadful formation of oxides at the Cu-Al interface. The subsequent aging treatments were conducted in a high-temperature tube furnace at temperatures ranging from 350ºC to 450ºC at various hours of time. For the entire duration of aging, the tube was filled with a continuous flow of $N_2$ gas to prevent oxidation.

## 3.3 Results & Discussion

### 3.3.1 Growth of IMC and Interface Failure

Analysis on the samples aged for various hours at temperatures ranging from 350ºC to 450ºC leads to the conclusion that there are essentially three IMC phases forming at all of the temperatures used in our study: $\theta$-$Al_2Cu$, $\gamma$-$Cu_9Al_4$, and an unknown IMC phase with a FCC-based crystal structure having a unit cell slightly larger than Cu. Other IMC phases such as $\eta$, $\xi$, and $\delta$ are not observed to form. There is the possibility that they are too short-lived to be detected, but the results are not inconsistent with previous research because those studies rarely find $\eta$, $\xi$, and $\delta$ phases either [66-68]. It is further determined that $\theta$-$CuAl_2$ is the first phase to form, followed by $\gamma$-$Cu_9Al_4$ and the FCC-based unknown phase. For the sake of this research, the yet unknown FCC-based phase will be named $\alpha$'. Their formation is clearly evidenced in XRD patterns taken from samples aged at all temperatures. The formation sequence and the type of IMC phases at interface is found to be essentially the same regardless of aging temperature. However, the reaction rate at 350ºC is too slow to track the full evolution of IMC phases within a reasonable amount of aging time; the formation of those three IMC phases becomes visible only after more than 500h of aging at 350ºC. Since the type and the sequence of IMC formation is determined to be unaffected by the aging temperature, their evolution is investigated using the samples aged at 400ºC and 450ºC and the resulting data is presented in this work.

Figure 3.1 shows XRD intensities taken from 673 K (400 ºC) aged samples as a function of 2-theta angle. It can be seen that the $\theta$-$CuAl_2$ forms as early as 20h of aging and the other two phases after 30h of aging.
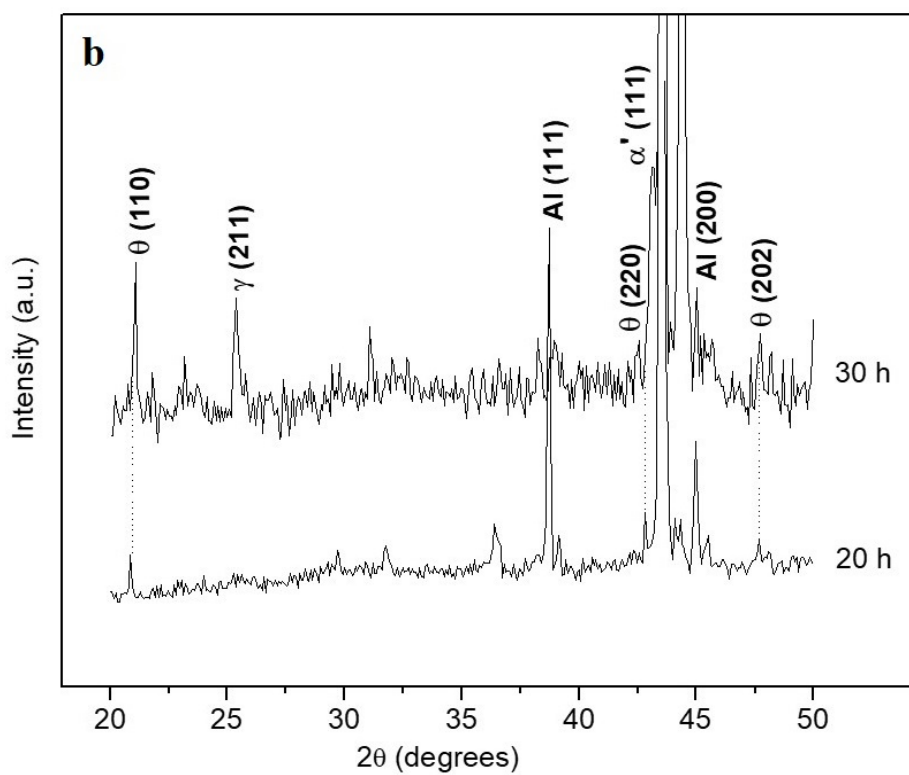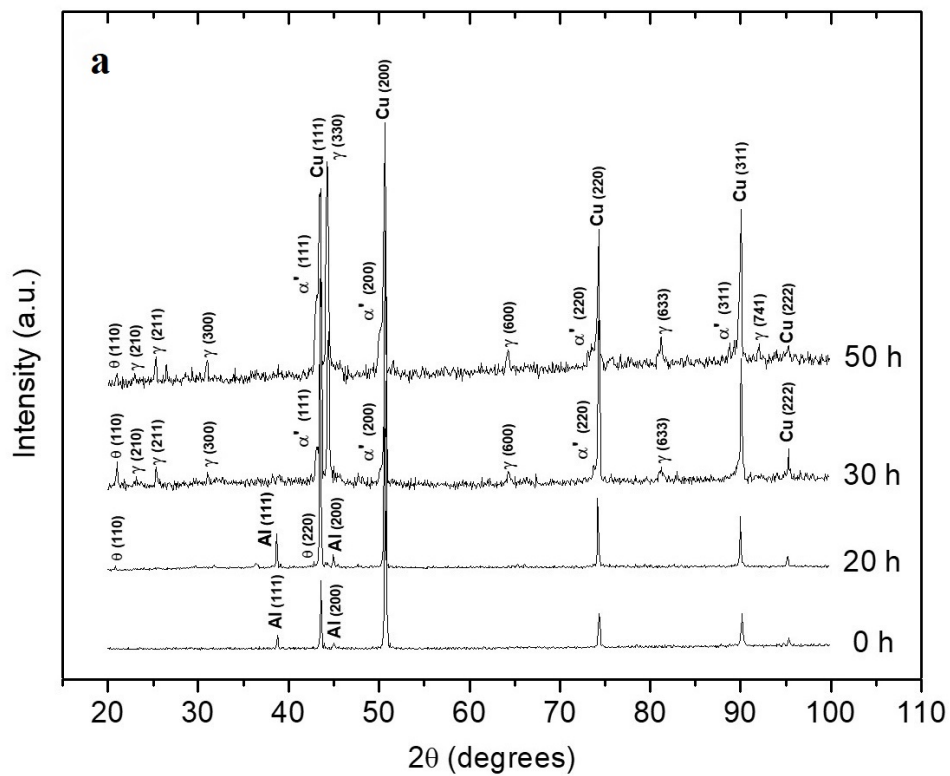
*Figure 3.1 (a) XRD patterns of sample aged at 400°C for various hours, and (b) enlarged view emphasizing on θ-CuAl$_2$ diffraction peaks.*

With a limited amount of Al, further aging prevents the formation of more $\theta$-$CuAl_2$ phase and existing amounts are quickly consumed by $\gamma$-$Cu_9Al_4$, until it completely disappears. At first glance, the peaks from the mysterious $\alpha'$ IMC phase appear as if they are part of Cu peaks. However, careful examination of the diffraction data reveals that the peaks are there. They are initially weak in intensity and their positions are very close to the Cu diffraction peak positions. This makes them appear as a slight left-shouldering of Cu peaks at the early stages of its formation, which is probably the reason why previous studies have failed to recognize the presence in the diffusion couple interface.

Further evidence for the formation of this new phase can be seen in the diffraction data collected from samples aged at 450ºC, which are shown in Figure 3.2. Except for the absence of $\theta$-$CuAl_2$ peaks, likely due to its complete consumption within 5h, the diffraction behavior of 450ºC samples are essentially the same as the ones from 400ºC and 350ºC. Continued aging makes both $\gamma$-$Cu_9Al_4$ and the new phase peaks intensify. One can notice that what appears as a left-shouldering of the Cu peaks in samples aged at 400ºC now becomes intense enough to appear as separate peaks. These peaks always appear at the left side of the Cu peaks and intensify with aging. Available data required for crystallographic analysis of the new phase is scarce, but we resolve the difficulty by considering the possibility of it being $\alpha_2$-$Cu_3Al$ phase. As shown in Chapter 1 (see Figure 1.11), where a schematic representation of the lattice structure of a $\alpha_2$-$Cu_3Al$ crystal is presented, $\alpha_2$-$Cu_3Al$ phase has a crystal structure of $D0_{22}$, which is fundamentally based on a FCC crystal.
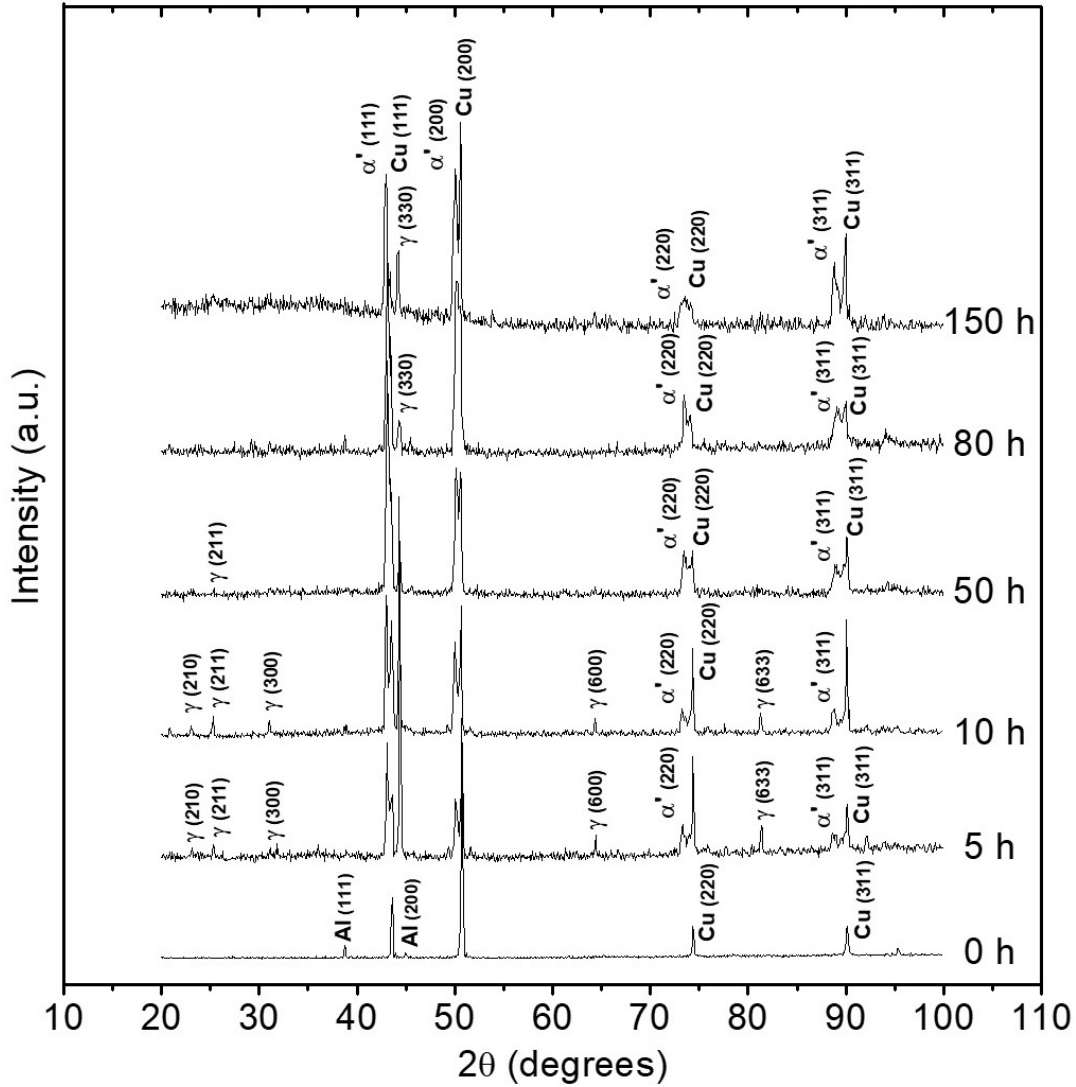
*Figure 3.2 XRD patterns of sample aged at 450°C for various hours.*

In essence, the principle diffraction behavior of this crystal closely resembles the FCC crystal because of the strong diffraction that occurs at conditions of unmixed (hkl), while weak superlattice diffraction occurs at mixed (hkl). The simplest way of understanding $\alpha_2$-$Cu_3Al$ diffraction associated closely to Cu is to consider the case of a completely disordered $\alpha_2$ phase. At disordered state, since each lattice point is with equal probability of having

Cu and Al, the crystal behaves the same way as Cu in terms of diffraction. Then, the Bragg's diffraction condition leads to:

$$\theta_B = \sin^{-1}\frac{\lambda\sqrt{h^2+k^2+l^2}}{2a} \quad \text{for unmixed (hkl),} \tag{3.1}$$

where $\theta_B$ is the Bragg angle, $a$ the lattice parameter (nm), $\lambda$ the x-ray wavelength (0.154nm), and *hkl* are the Miller indices. According to Kuwano et al. the lattice parameter of $\alpha_2$-Cu$_3$Al phase is about 0.3668nm, which is ~2% larger than that of pure Cu, 0.3597nm. Therefore, the principle XRD peaks of $\alpha_2$-Cu$_3$Al phase will appear to the left-side of Cu peaks with a small separation in the peak position. When the lattice parameter in our experiment is back-calculated using eq. (3.1) from the peak positions of the left side of the doublet in Figure 3.2, it is determined to be 0.3645nm on average, which is slightly inferior to the lattice parameter of $\alpha_2$-Cu$_3$Al. Further, according to the Al-Cu phase diagram, $\alpha_2$-Cu$_3$Al is supposed to decompose peritectoidally at 363ºC. Nevertheless, this new IMC was observed from 350ºC all the way to 450ºC. The hallmark evidence for $\alpha_2$-Cu$_3$Al phase formation would have been the (100) and (110) superlattice peaks expected from an ordered D0$_{22}$ structure. However, such superlattice peaks are not visible in all diffraction results. Hence, it could be tempting to think that what is believed to be $\alpha_2$-Cu$_3$Al formed by interdiffusion is in either a disordered or partially ordered state; the incomplete ordering might result from the fact that interdiffusion is a dynamic process and thus the atomic ordering is more difficult to achieve. However, because of the ambiguity and the lack of decisive evidence at this stage, we will treat the new IMC phase α' as a separate entity.

The formation of the new α' IMC phase and growth with aging treatment is also confirmed by our microscopic analysis of the interface microstructure. Figure 3.3 presents

a series of SEM micrographs of the sample interface after the aging treatment at 450ºC for various hours.  These images clearly show the existence of a distinctive phase in between the $\gamma$-$Cu_9Al_4$ phase and Cu substrate.
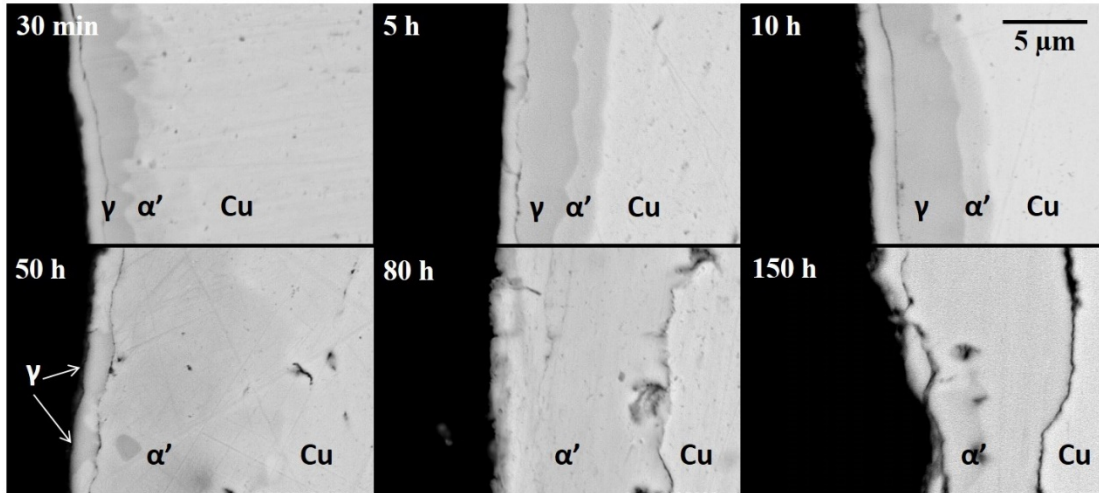


*Figure 3.3 SEM pictures showing the growth of IMC with aging time at 450°C.*

For phase contrast enhancement, these SEM micrographs are taken with a backscattered electron BSE detector.  Since the intensity of the BSE is roughly proportional to the atomic density of element present in the area, the BSE produces an image with compositional contrast.  In this particular case, because Cu is heavier than Al, the area containing a higher Cu concentration appears brighter.  One can note the presence of a layer with a distinctive contrast between $\gamma$-$Cu_9Al_4$ phase and the Cu substrate.  This area grows further into the Cu substrate as the aging progresses while consuming $\gamma$-$Cu_9Al_4$; the complete consumption is found to occur at approximately 80h of aging.  Compositional analysis conducted using EDS reveals that it has a chemical composition ranging from 17 to 22 at.% Al.  Although chemical composition taken from EDS cannot be used in quantifying the exact composition of the phase under investigation, it can provide supplementary evidence to the result

obtained from the XRD analysis and suggests the formation of a distinct phase of specific composition. Note also the formation of the interface crack precisely following the Cu interface. When the aging time reaches 80h, the $\gamma$-$Cu_9Al_4$ phase has been completely consumed and the interface crack has started to form. Further aging promotes the cracks to develop to a degree that induces noticeable interfacial delamination failure. This result, failure at the interface between Cu and the Cu-rich IMC, is in good agreement with the conclusions made in other studies and therefore it is reasonable to conclude that the failure in the Al-Cu diffusion couple occurs by delamination along the Cu substrate.

The complete consumption of $\gamma$-$Cu_9Al_4$ after 80h of aging, shown in Figure 3.3 is a result of interdiffusion in a system with a limited supply of Al. In fact, diffusion in our system can be treated as Al diffusion in a semi-infinite Cu with its source at the Cu surface. In such a condition, a rapid consumption of the Al-rich phases, such as $\theta$-$CuAl_2$ phase, occurs by interdiffusion, followed by the sequential consumption of the Cu-rich phases. Therefore, the complete consumption of $\gamma$-$Cu_9Al_4$ phase, observed in samples aged for 80h, is consistent with the usual interdiffusion mechanism. In the case of prolonged aging, it is likely that $\alpha'$ phase would also disappear by a continuation of Al dilution. However, since cracking at interface disrupts the diffusion path for Al, $\alpha'$ phase disappearance cannot be experimentally realized. This makes the estimation of interdiffusivity complicated, but an activation energy for Al diffusion in Cu can still be approximated. If it is assumed that the growth of the IMC layer, regardless of its kind, represents the penetration of Al into Cu through diffusion, the total IMC thickness, or the $\alpha'$ phase growth front, can be treated as a marker for Al diffusion into Cu. Therefore, the phase growth front, X, is expected to follow a parabolic kinetic relation as function of time:

$$X^2 = Kt, \tag{3.2}$$

where $K$ and $t$ represent the kinetic constant and aging time, respectively. Figure 3.4 presents the average position of the α' phase front, measured by a cross-sectional inspection of the sample interface, as a function of aging time at 400ºC and 450ºC. A reasonable agreement of data to equation (3.2) is evident in this plot.
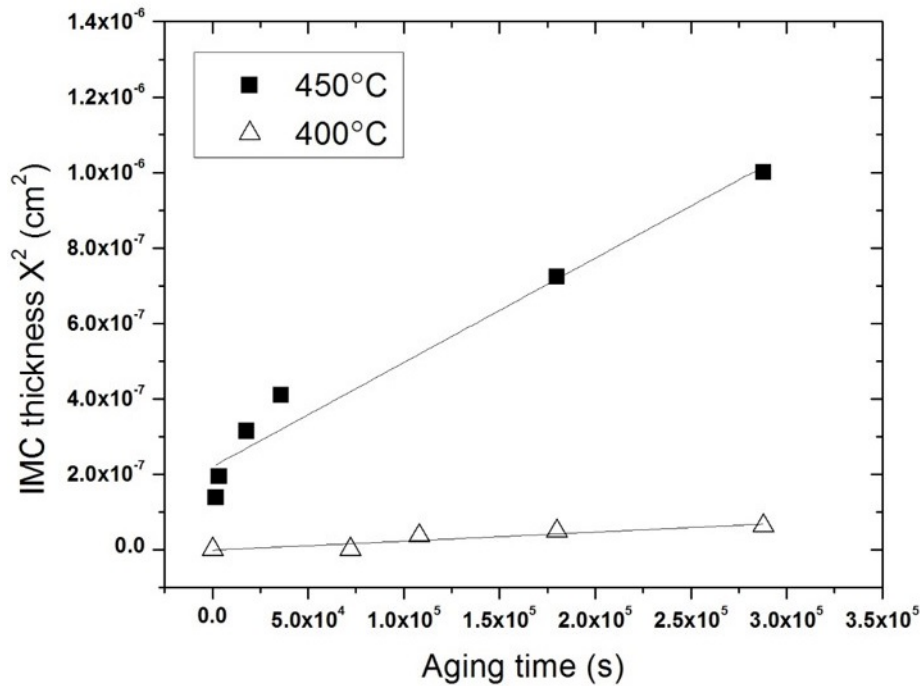


*Figure 3.4 Plot of the square of the total IMC layer as function of the aging time.*

The Arrhenius plot used to determine the activation energy is shown in Figure 3.5. Such plots are often utilized as a way to analyze the contribution of temperature on the rate of chemical reactions. A linear regression is acquired when a thermally activated process such as diffusion is involved. One can then compute the pre-exponential factor as well as the activation energy. The activation energy of the Al diffusion, estimated from the kinetic constant $K$ obtained at 400ºC and 450ºC is ~1.85eV.
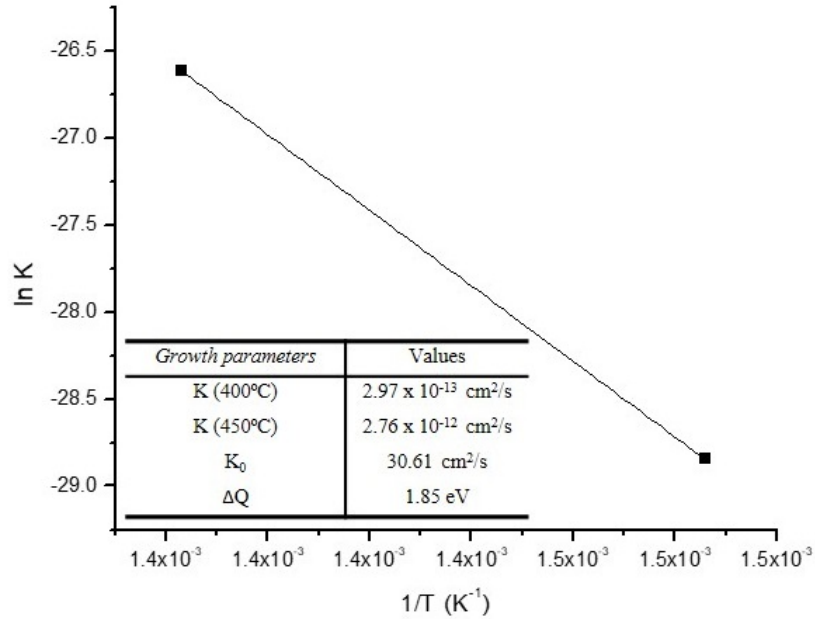
*Figure 3.5 Arrhenius plot applicable to this Cu-Al interdiffusion system.*

Knowing the values corresponding to the pre-exponential factor and having extracted the activation energy, it is now possible to derive the IMC growth rate as function of temperature and time:

$$X^2 = \left[\left(30.61 \exp\left(\frac{-21715}{T}\right)\right) t\right] \tag{3.3}$$

Where $X$ is the total IMC thickness, $T$ is the temperature, and $t$ is the diffusion time. In this analysis, the IMC thickness as function of time obtained after aging at 350°C was not included on purpose, as its growth rate was too slow to yield data assisting the activation energy analysis. Therefore, the estimated activation energy cannot be taken too seriously, but it at least suggests a bulk diffusion dominance, as it is very close to the activation energy for Al bulk diffusion in Cu reported in other studies. It is our belief that the bulk diffusion dominance is a result of annealing treatment conducted prior to Al thin film

deposition, because recrystallization and subsequent grain growth effectively reduces the short-circuit diffusion paths like dislocations and grain boundaries.

### 3.3.2 Interface Strain Analysis

The failure at interface shown in Figure 3.3 deserves further analysis in order to determine its mechanism. Two main sources of interface failure are associated with IMC growth. The first is what is known as the Kirkendall effect, which is the result of a mass flux imbalance at the phase boundary. There is a competing failure process that is stress driven interface fracture. An IMC phase formation can produce a lattice distortion to itself and surrounding phases. Interface fracture can be induced when the lattice distortion produces sufficient stress to result in a crack initiation and growth. While these two mechanisms are equally possible, and the first is the more frequent mechanism in most cases, our experiment produces repeated evidence that the failure observed in our study is the result of the development of interface strain between α' phase and the Cu substrate, and not by the collection of Kirkendall voids.

The first indicator for the strain development is found from a Williamson-Hall (W-H) analysis conducted on the XRD results [69]. According to the W-H theory, the FWHM (full width half maxima) of any x-ray diffraction peak is influenced by the grain size as well as a non-uniform lattice strain existing in the material, namely:

$$\beta_{hkl} \, cos\theta_B = (\frac{0.9\lambda}{D}) + 4 \, \varepsilon \, sin\theta_B, \tag{3.4}$$

where $\beta_{hkl}$ represents the FWHM of a peak at *(hkl)*, $D$ is the average grain size, and $\varepsilon$ the lattice strain, respectively. When diffraction occurs in materials with an appreciable degree

of internal strain, the quantity $\beta_{hkl}\, cos\theta_B$ would become a linear function of $4\, sin\theta_B$ with

a proportionality to ε.  A W-H analysis on the diffraction results of γ-Cu₉Al₄ and α' phase

from Figure 3.2 is shown in Figure 3.6.  Notice the fact that $\beta_{hkl}\, cos\theta_B$ shows a linear

dependence on $4\, sin\theta_B$ for the case of α' phase, while such dependence is absent in γ-

Cu₉Al₄ phase, indicating the presence of mechanical strain in α' but not in γ-Cu₉Al₄ phase.
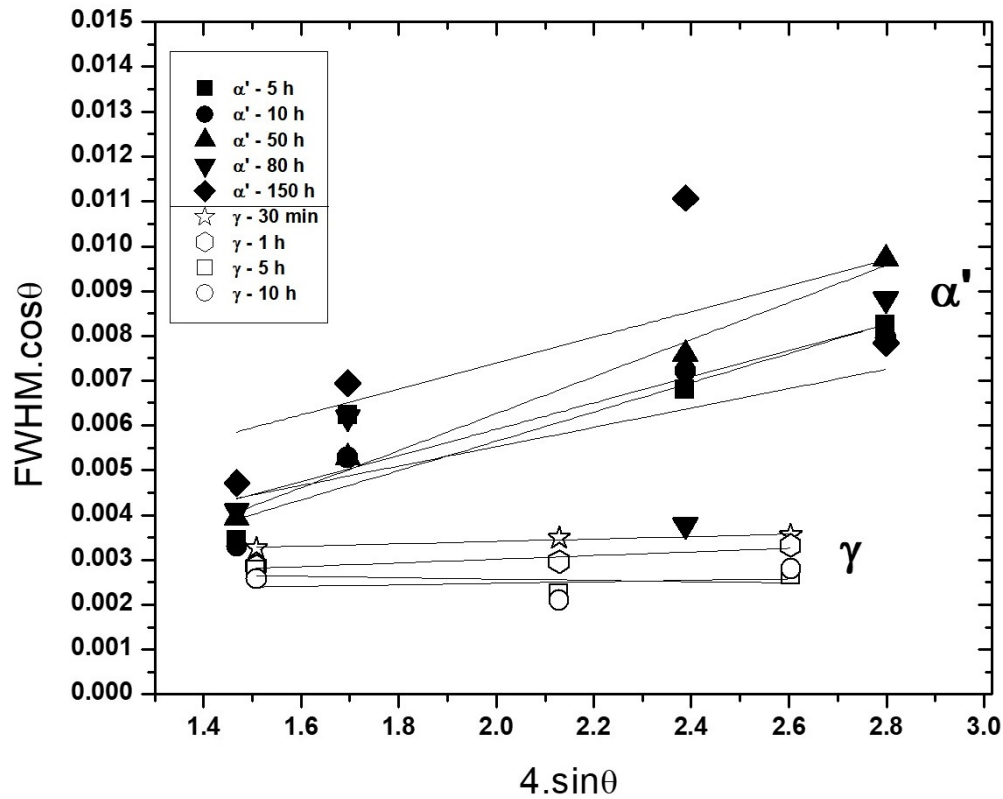


*Figure 3.6 Williamson-Hall analysis conducted on* α' *and* γ *peaks.*

Although the results shown in Figure 3.6 provide evidence of the existence of strain in α',

it does not provide any indication as to the direction and source of strain.  Careful

inspection of all diffraction peaks reveals that the strain in α' is compressive and that it is

the result of lattice continuity with the Cu substrate.  Supporting evidence is presented in

Figure 3.7, where an enlarged view of the diffraction result, near the Cu (111) peak, is displayed for the case of 0.5h, 1h and 5h aging at 450ºC.
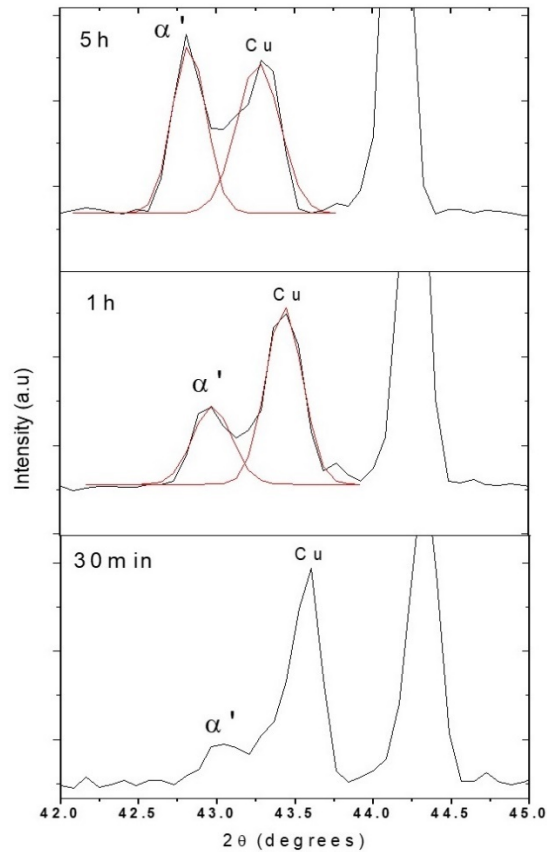


*Figure 3.7 XRD patterns showing the doublet (111) diffraction of α' and Cu. The dotted red line shows the peak separation.*

The first distinctive feature to notice is the growth of α' (111) peak located at the left side of the Cu (111) peak. The small separation in peak position between these two peaks forms what is referred to as a doublet. Similar doublets are observed at all other Cu diffraction peaks. The doublet can be split into two separate peaks by the usual process of deconvolution, which involves an assumption of two Gaussian functions. However, the peak splitting produces a result indicating that there exists an excess intensity in between

the two peaks. This means that the right side of α' (111) peak is slightly more intense while the same exists in the left side of Cu (111). This type of asymmetric diffraction peak shape is routinely observed in the epitaxial growth of thin films, where two materials are joined with a lattice continuity across an interface. This epitaxy forces the two lattices to be connected even if the lattice spacing is not the same. Then, the material with the larger lattice spacing will be compressed and the material with smaller lattice spacing will be stretched. This causes the interplanar spacing of each material to change at the interface, making the diffraction intensity to be stronger on one side of the diffraction peaks for each material. A right shift of peak intensity implies lattice parameter decreasing, and a left shift implies a lattice parameter increase. We believe that the same mechanism is at work in our case. Since the difference in the lattice parameter of these two phases is likely to be maintained, if not signified with difference in thermal expansion coefficient at aging temperatures used in our study, the condition of lattice continuity makes a certain volume of α' phase at the interface to be under compression and Cu to be under tension. This strained volume of α' and Cu at the interface adds additional intensity to the diffraction angles in between the $2\theta_B$ (111) for the α' phase and Cu substrate. Presently, it is not clear whether the interface has perfect coherency or not; however, available data suggests that the interface maintains a sizable degree of lattice continuity prior to the interface failure.

The interface lattice strain, that is compressive for α' phase and tensile for Cu substrate, is found to increase with aging time until it becomes too high for the interface to sustain the continuity. Evidence for the increasing strain, with the growth of α'phase, is found from the change in the lattice parameters of the α' phase and the Cu substrate corresponding to aging. The lattice parameter of each phase in our experiment has been

back-calculated from the diffraction peak positions using eq. (3.1). The average lattice parameter of each phase and its change with aging time at 450ºC is shown in Figure 3.8 (a). Note the continuous increase and decrease of lattice parameters for the α' phase and Cu substrate, respectively, until aging time reach 80h.
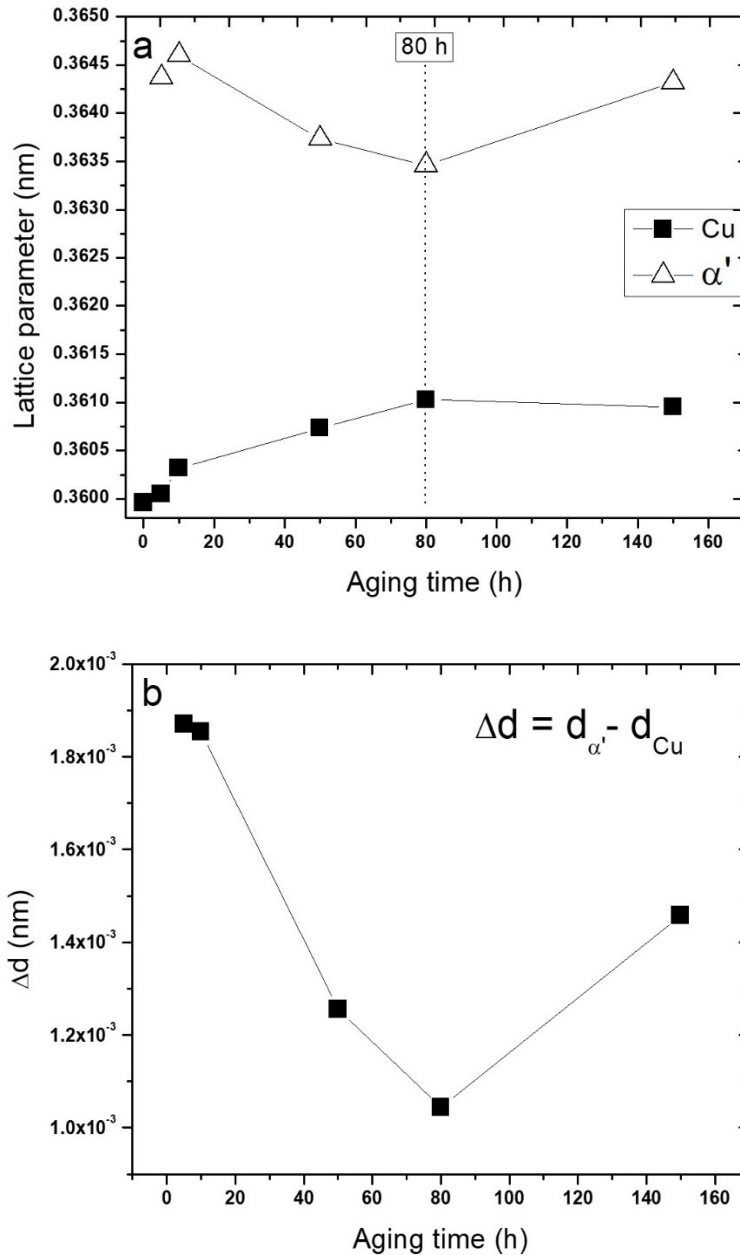


Figure 3.8 Plots showing the change in the lattice parameter of α' and Cu (a), and the total difference in the lattice parameter between the two phases (b) as a function of aging time at 450ºC.

This physically means that compressive strain in α' phase and tensile strain in Cu substrate increases with the growth of α' phase. The strain reaches a maximum at 80h of aging, at which point an interface crack develops as shown in Figure 3.3. Breaking the lattice continuity, the interface crack induces strain relaxation and results in the lattice parameter of both phases changing in the direction of an unstrained condition. Figure 3.8 (b), where the net difference in the lattice parameter of the two phases is plotted as a function of aging time, clearly shows the relaxation of the interface strain after 80h of aging.

The observation of interface strain and its association with crack formation provides a reasonably consistent explanation to the interface failure observed in previous studies. Our analysis suggests that the interface fracture occurs when the α' phase reaches a critical thickness that induces interface strain (or stress) sufficient for crack nucleation. Figure 3.9. shows the α' phase growth mechanism triggering failure.
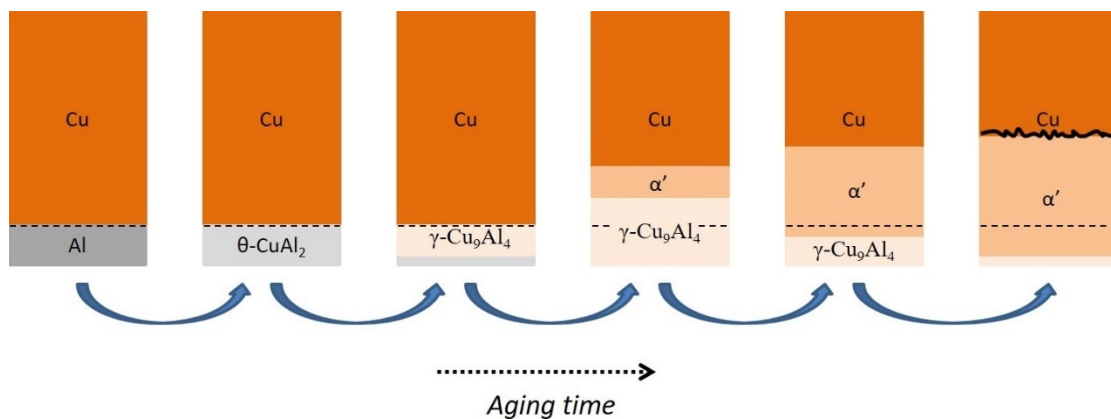


*Figure 3.9 Suggested mechanism for IMC growth leading to crack nucleation.*

The critical thickness for the interface failure needs more investigation, but it is likely to scale inversely with temperature. In other words, the interface crack would form with much less growth of α' phase if the interface reaction is induced at lower temperature than

the aging temperature used in our study. We believe that the temperature effect exists because the activity of the strain relaxation mechanism is strongly affected by temperature in metallic materials. The interface strain is elastic in nature but can be released by way of plastic deformation. Since the relaxation mechanism, like dislocation glide or creep, is less active at lower temperatures, the interface becomes increasingly prone to fracture with decreasing reaction temperature. Another consideration point is the influence of other IMC phases on the interface fracture. The evolution of interface microstructure shown in Figure 3.3 seems to suggest that $\gamma$-$Cu_9Al_4$ phase affects the failure because the interface crack forms at aging condition where $\gamma$-$Cu_9Al_4$ phase is nearly consumed. It is possible that $\gamma$-$Cu_9Al_4$ phase provides a mechanical constraint that limits the interface strain and crack initiation. But, we believe that such an effect plays a minor role, and that the result of crack formation at the time of $\gamma$-$Cu_9Al_4$ phase consumption is likely to be a coincidence. If $\gamma$-$Cu_9Al_4$ phase provides a damping effect to a degree to suppress the interface strain, it should also be strained, which is not supported by the W-H analysis result shown in Figure 3.6. Therefore, it is not unreasonable to conclude that the most influential factor for the interface failure is the growth of $\alpha$' phase that creates the interface strain.

### 3.3.3 Discussion

The findings made in our investigation resolve various uncertainties in the mechanism of IMC formation and interface failure reported in studies of Al-Cu interdiffusion. As evidenced by our XRD analysis, the source of the failure is the interface strain. Such strain development is shown to be impossible in cases where Cu is interfaced with $\gamma$-$Cu_9Al_4$ phase. The crystal structure of $\gamma$-$Cu_9Al_4$ phase is so different from Cu that the $\gamma$-$Cu_9Al_4$ phase is likely formed by a process of nucleation and growth, and thermal

53

strain would be the only source of strain.  Without the formation of α' phase, interface failure by cracking, observed in other studies, cannot be adequately explained.

While successful advancements in understanding the various aspects of interdiffusion in Al-Cu system have been made through our findings, there still remains several details that deserve further analysis.  The first is related to the sequence of IMC phase formation observed in our experiment.  It is observed that the first phase formed by interdiffusion is θ-$CuAl_2$ phase and it is followed by γ-$Cu_9Al_4$ and α' phases.  This may appear to suggest that θ-$CuAl_2$ phase has the lowest formation energy among all IMC phases.  It is very tempting to make such an assertion, especially considering conflicting reports about the formation energy for θ-$CuAl_2$ and γ-$Cu_9Al_4$ phases [70-72].  However, such a conclusion cannot be made from our results and there is a more reasonable explanation.  The θ-$CuAl_2$ phase is the terminal phase at the Al-rich end of the diffusion couple, and it forms by a diffusion of Cu into Al.  Because the grain size of Al thin film is very small, ~1μm, Cu diffusion can be assisted greatly by the grain boundary diffusion mechanism. This grain boundary density difference between the thin film and bulk, close to one order of magnitude, causes the diffusion to primarily occur within the Al thin film during the first stages of the interdiffusion process. Additional evidence is found in the SEM micrograph Figure 3.3 when after 30min of aging the Al thin film is already consumed by the Cu-rich IMC γ-$Cu_9Al_4$. Naturally, this confirms that θ-$CuAl_2$ is the very first IMC phase to form.

The second finding deserving more in-depth analyses is related to α' phase formation, as it was demonstrated that it plays a primordial role in the interface failure. XRD results show without any ambiguity that this IMC has a FCC-based crystal structure

slightly larger than Cu. Many similarities have been shown to exist between the known $\alpha_2$-Cu$_3$Al and $\alpha'$; their crystal structure, lattice parameter, and chemical composition make for a very similar diffraction behavior, assuming $\alpha_2$-Cu$_3$Al is partially disordered. Nevertheless, the high temperature stability of $\alpha'$ poses a problem when knowing that past studies suggested that $\alpha_2$-Cu$_3$Al decomposes by peritectoid reaction at only 363°C. It is a fact that interdiffusion doesn't always follow the equilibrium phase diagram, and IMC phases can be stabilized at higher temperatures by the presence of impurities. However, the stability around 100°C above the equilibrium limit is odd and difficult to grasp. In the light of these observations, and the lack of key indicators, we decided to treat $\alpha'$ as a new FCC-based IMC phase containing a slightly inferior Al content than $\alpha_2$-Cu$_3$Al. Further investigations regarding its formation mechanism, structure, and stability will be the subject of the next chapter.

The third aspect of IMC formation in need of further analysis is related to the interfacial continuity between $\alpha'$ and Cu. All experimental observations consistently suggest that $\alpha'$ phase growth proceeds while maintaining some degree of interface coherency with Cu lattice. This type of growth is essentially the same process as the solid -state epitaxy that usually demands careful placement of atoms. At first glance, it seems impossible that such an organized atomic growth can occur during the interdiffusion process. However, considering the fact that $\alpha'$ crystal structure is not so different from Cu solid solution, growth by solid state epitaxy may not be unrealistic. Further, placement of Al atoms into Cu unit cells, that turn Cu into $\alpha'$, involves little lattice expansion. This makes the coherent boundary more favorable than the incoherent boundary because the

strain energy should be far smaller than the phase boundary energy at such conditions. These factors enable the α' phase growth by a manner similar to that of solid state epitaxy.

Finally, it should be noted that our findings can have several practical implications to reliability problems common in engineering components based on a Al-Cu pair. In particular, they can be helpful to better understand the failure mechanism of the Cu wire-bond, promoting engineering routes for its suppression. While the interdiffusion in the wire-bond proceeds at temperatures well below $200^{\circ}C$, the process of IMC formation and subsequent failure should be governed by the same mechanism found in this study. An extension of understandings made in this study suggests that the failure in Cu wire-bond occurs by the stress driven interface facture at a time when α' phase grows to a critical thickness. It is therefore important to find a way to suppress the growth of α' phase. In this regard, engineering the microstructure of Cu wire is likely to be more effective especially because the failure is predicted to be on the Cu wire side, not in the Al pad of the interface. The failure location is predicted to be on the Cu wire side because α' is the phase interfaced with Cu, and forms by the process of Al diffusion into Cu wire. Reduction of short-circuit diffusion paths like dislocations, grain boundary and free surface can be effective in delaying the failure. Equally important is to remove or reduce residual stress in the Cu wire. Residual tensile stress coupled with the interface stress can make the interface much more susceptible to fracture. In particular, the control of the residual stress near the wire surface is expected to be the most critical for several reasons. It is our expectation that the surface end of Cu-α' phase interface is most likely to fracture. This is the location where α' growth would be the most extensive with surface assisted diffusion. Furthermore, the difference in the elastic modulus of α' phase and Cu makes the residual

stress distribute with a singularity at the interface. These factors allow crack nucleation at the surface end of the interface with growth propagating inward.  In fact, a majority of studies on wire-bond failure report that the failure begins at the surface end of the interface, which agrees very well with the prediction.

## 3.4 Conclusion

Experimental investigation on the IMC formation and growth by interdiffusion in Al-Cu binary system, conducted using 2µm thick Al coated Cu bulk plate with variation in aging time at temperature between 350ºC and 450ºC, reveals two essential findings.  The first is the fact that the terminal IMC phase at the Cu-rich end of the diffusion couple is the newly found $\alpha'$ phase, not the conventionally believed $\gamma$-$Cu_9Al_4$.  This IMC phase is likely to be similar to $\alpha_2$-$Cu_3Al$, but displays stability at much higher temperatures.  The second is the fact that the interface strain development parallels the formation and growth of $\alpha'$ phase, probably due to the lattice continuity between $\alpha'$ and Cu solid solution.  This interface strain is believed to trigger the interface failure by crack nucleation and its propagation.

Chapter 4: High-Temperature Investigation of Cu-Al Diffusion Couple: Evidence for D0$_{22}$ ordering within α-Cu(Al) Solid Solution Range

## 4.1 Introduction

In the previous chapter, we found evidence suggesting that an unaccounted-for FCC-based intermetallic phase, α', exists in compositions considered to be at the solubility limit of α-Cu(Al), and at temperatures too high for it to be α$_2$-Cu$_3$Al. Unlike other binary alloys, α-Cu(Al) is reported to exhibit anomalous properties such as an odd dependence of the specific heat, electrical resistivity, and microhardness on composition and aging [73]. Previous studies have suggested a local short-range order (SRO) as a probable mechanism, and that SRO may create domains having the composition of Cu$_3$Al with the L1$_2$ structure [74-80]. This aforementioned mechanism is possible to entertain, as it is a well-known fact that Al-Cu solid solutions exhibit a negative enthalpy of mixing ($\Delta H_{mix} < 0$) over the whole range of composition [81], thus favoring the formation of A-B bonds.

In the present study, we chose an approach using high-temperature interdiffusion and atomic-scale characterization to obtain clearer information about this phase's crystal structure as well as its phase field. Even though characterization of alloys with specific concentrations can yield interesting information related to phase field, it can also pose considerable difficulty, especially when two phases, if present, are in close proximity in diffraction behaviors. Additionally, sluggish and slow ordering reactions due to limited chemical potential gradient (thermodynamic driving force) can lead to characterization omission and inaccuracies. On the other hand, diffusion couple induces formation of equilibrium phases across the composition at given temperatures and thus enables easy

identification of phases involved, while ambiguity is often a result of suppression or rapid consumption of possible phases, due to lack of their stability as well as kinetics. Further, a considerable amount of real world Al-Cu systems exist as couples where interfacial reactions resulting from diffusion are of primary importance. For this purpose, we conducted a diffusion couple experiment by preparing Cu plate coated with 2µm thick Al thin film and inducing diffusion at various high temperatures, ranging from 525-625$^{o}$C.

## 4.2 Methodology

The samples investigated in the interdiffusion experiments were fabricated following the same protocol as in Chapter 3 (section 3.2). The detailed procedure can be found there. The thermal treatment for inducing interdiffusion was conducted in a high-temperature tube furnace at temperatures of 525ºC and 625ºC, for 1h and 5min respectively. For the entire duration of aging, the tube was filled with a continuous flow of 95% $N_2$-5% $H_2$ forming gas to prevent oxidation. All samples were quenched in ice water following each thermal treatment.

## 4.3 Results & Discussion

Figure 4.1 (a) shows the Cu-rich end of the phase diagram where three IMCs are shown to exist: $\gamma$-$Cu_9Al_4$, $\beta$-$Cu_3Al$ and $\alpha_2$-$Cu_3Al$. The temperatures chosen for interdiffusion appear as blue and red dotted lines for 525ºC and 625ºC respectively. Considering the thin film-bulk configuration of the diffusion couples and the limited Al supply, it is expected that

Al-rich IMCs will quickly be consumed and transform into Cu-rich IMCs. Consequently, at 525ºC $\gamma$-$Cu_9Al_4$ should be the phase coexisting with $\alpha$-Cu(Al), while $\beta_1$' ($\beta$-$Cu_3Al$ that underwent martensitic transformation during quenching) should be the one at 625ºC. Figure 4.1 (b) shows the diffraction patterns obtained after interdiffusion. After 1h at 525ºC it can be seen that the complex metallic alloy $\gamma$-$Cu_9Al_4$ is present along with Cu. However, a new set of diffraction peaks very reminiscent of the previously found $\alpha$' phase appear to form doublets with those of Cu. One can notice that they always exist at the left of each Cu reflection. The diffraction pattern taken after 5min at 625ºC confirms the existence of these doublets along with the equilibrium IMC $\beta$-$Cu_3Al$. It is important to mention at this point that this must be a separate phase and cannot be a disordered solid solution. The existence of doublets indicates an abrupt change in composition and a resulting interphase. According to the diffraction patterns, the phase must have an FCC-based structure with a lattice constant slightly bigger than the one of pure Cu. After lattice parameter calculation, the result yields a = 3.65Å for this new phase, compared to a = 3.61Å for pure Cu. There is no doubt at this stage that the new phase corresponds to the $\alpha$' phase found in lower temperature interdiffusion conditions in Chapter 3. Its exceptionally high stability confirms that it is indeed distinct from the $\alpha_2$-$Cu_3Al$ phase aforementioned.
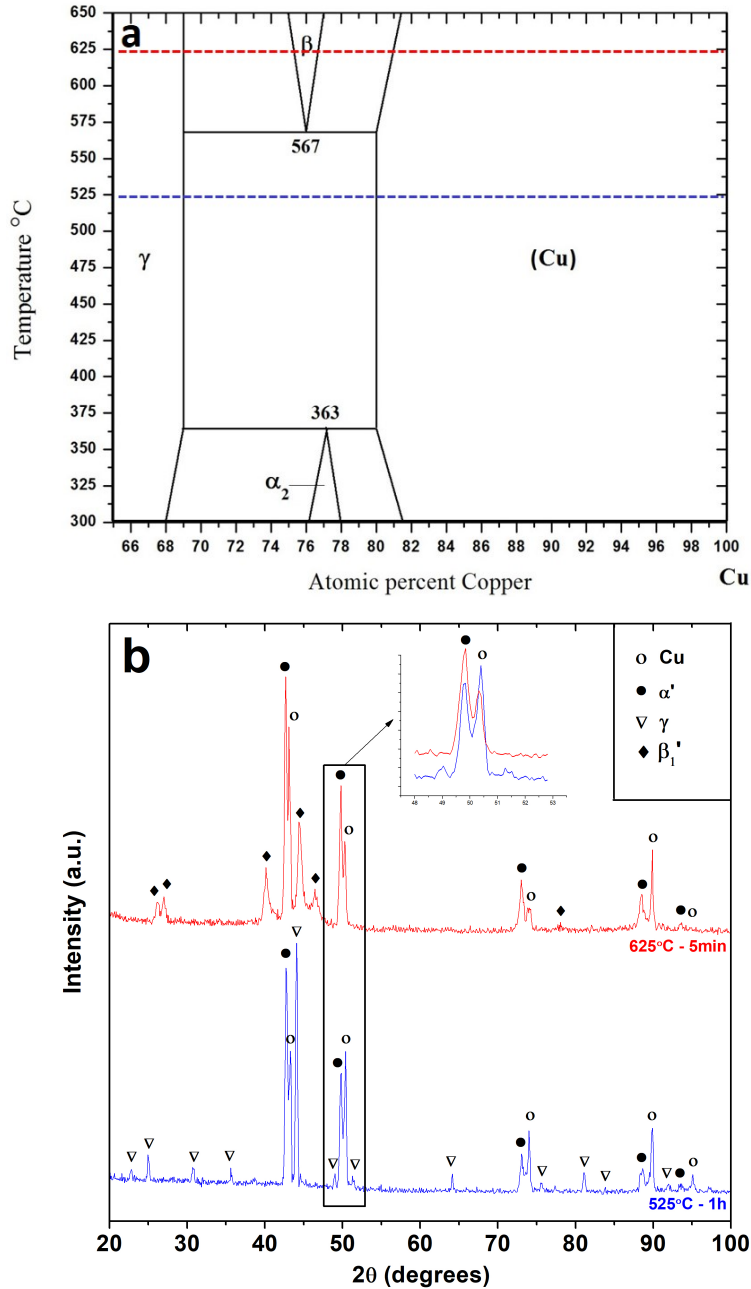
*Figure 4.1. (a) Cu-rich end of the phase diagram. The blue and red dashed lines indicate the annealing temperatures used. (b) XRD patterns after annealing at 525℃ for 1h and 625℃ for 5min.*

Figure 4.2 (a) and Figure 4.2 (b) show the SEM cross-section of the sample annealed at 525℃ for 1h and 625℃ for 5min, respectively. The inset is the same picture taken with optical microscope. The etchant reveals that both γ-$Cu_9Al_4$ (γ-brass) and $β_1$'

(orthorhombic) indeed have very different crystal structures compared to Cu. Especially, one can note the typical martensite structure of $\beta_1$', composed of randomly oriented needles (Figure 4.2 (b)). However, the 1-2$\mu$m $\alpha$' layer that grows directly on the Cu end doesn't seem to disrupt the Cu bulk. Only a slight change in contrast after etching indicates a higher Al content. Additionally, one can notice that the twin boundary at the bottom of Figure 4.3 (a) crosses the $\alpha$'/ Cu boundary without interruption. As hypothesized in Chapter 3 when discussing the interface failure mechanism, serious experimental evidence suggests that $\alpha$' was grown epitaxially with the Cu substrate due to the similarity in crystal structures and the lattice mismatch inferior to 2%. Compositional analysis conducted using EDS revealed that $\alpha$' has a chemical composition close to the maximal solubility of Al in $\alpha$-Cu(Al), yielding an Al content ranging from 17 to 20 at.%.
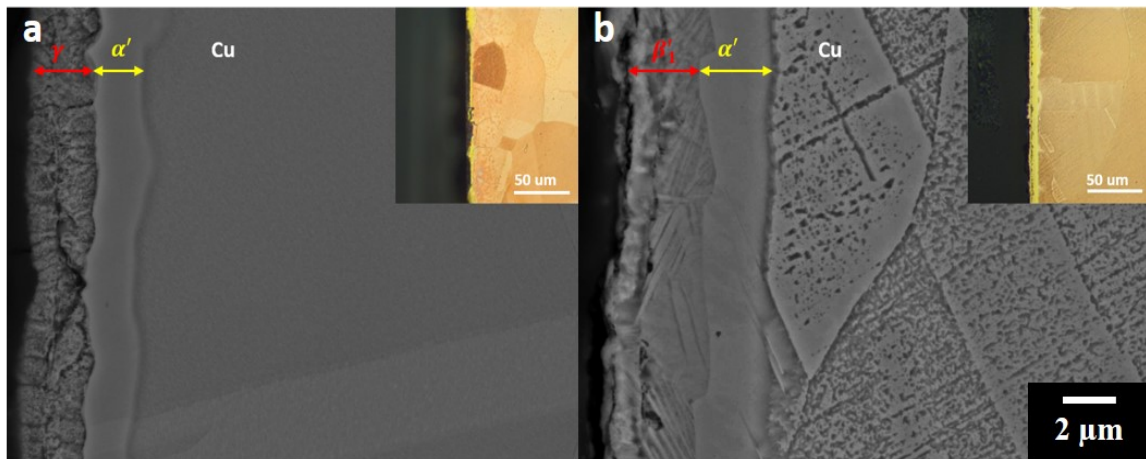


*Figure 4.2 SEM cross-sections after annealing at 525℃ for 1h (a) and 625℃ for 5 min (b). The inset is the equivalent picture taken with OM.*

In light of these results, additional in-situ high-temperature XRD experiments were carried out to definitively rule out the possibility that $\alpha$' forms upon quenching. Figure 4.3 displays the high-temperature XRD patterns recorded at different time intervals at 400℃.

The XRD patterns are focused around the Cu (111) reflection for improved x-ray intensity and readability.
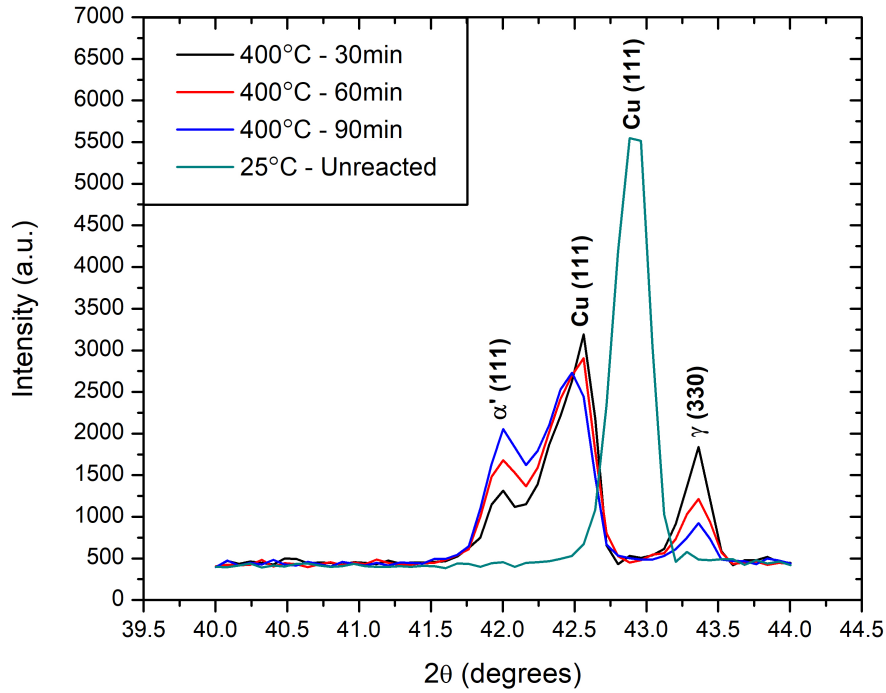


*Figure 4.3 In-situ XRD patterns recorded after 30, 60, 90min at 400ºC, and compared to an unreacted sample analyzed at room temperature.*

It is first important to specify that the peak shift of Cu (111) between the room temperature and 400ºC specimens is due to thermal expansion. From these patterns it can clearly be seen that α' first appears as a left-shouldering of Cu (111), and progressively develops into a distinct diffraction peak that increases in intensity as a function of the aging time. This supplemental evidence proves beyond any doubt that α' indeed exists at the high-temperature previously claimed.

An atomic scale analysis was carried out on the sample aged for 1h at 525ºC and is displayed in Figure 4.4. The HRTEM micrograph of the γ-Cu$_9$Al$_4$ / α' interface is shown in Figure 4.4 (a). The SAED pattern seen in Figure 4.4 (b) was taken close to this interface

where the Al content is higher. Careful analysis of this SAED pattern revealed a [111] zone axis of a $D0_{22}$ crystal structure. The simulated and indexed diffraction pattern in Figure 4.4 (d) unmistakably prove the presence of $D0_{22}$ ordering. The superlattice spots appear somewhat faint and diffuse, as the phase is off-stoichiometry compared to the typical $A_3B$ formula for $D0_{22}$ structures. Constitutional vacancies must be present to allow this ordering to happen at about 5at.% less Al than the stoichiometric composition. Non-ideal ordering could also be the result of the high-temperature used that engenders high atomic mobility, rendering the ordering process more difficult to achieve. Figure 4.4 (c) is the SAED pattern taken from the $\alpha$-Cu(Al) solid solution underneath $\alpha$' at [112] zone axis, while Figure 4.4 (e) is the corresponding simulated diffraction pattern. No HRTEM micrograph is shown in this case, as no clear interface could be detected, due to the similarities in crystal structure between $\alpha$' and $\alpha$-Cu(Al). In this localized, one grain case, the question arises as to why $\alpha$' and $\alpha$-Cu(Al) are observed from a different zone axis, namely [111] and [112], even though no sample tilting was operated. The question can be easily addressed by analyzing both unit cells, as well as their respective indexing. Figure 4.5 shows a comparison between a simple FCC unit cell and a $D0_{22}$ unit cell. The $D0_{22}$ modeling parameters were taken from the diffraction data of $\alpha$', where a = 3.65Å, and the tetragonality component was taken from the work of Kuwano et al. on $\alpha_2$-$Cu_3Al$; c/a = 1.002 approximately. To better illustrate this, $(111)_{FCC}$ and $(112)_{D022}$ planes, shown as parallel in Figure 4.4 (d) and (e) were added to the drawing. One can see that despite different indexing, they are crystallograhically equivalent planes. Since $\alpha$' has a lower symmetry $D0_{22}$ structure, the planar mismatch of all probable crystallographic orientation between $\alpha$' and Cu was calculated using the two-dimensional disregistry approach suggested by Bramfitt [82]:
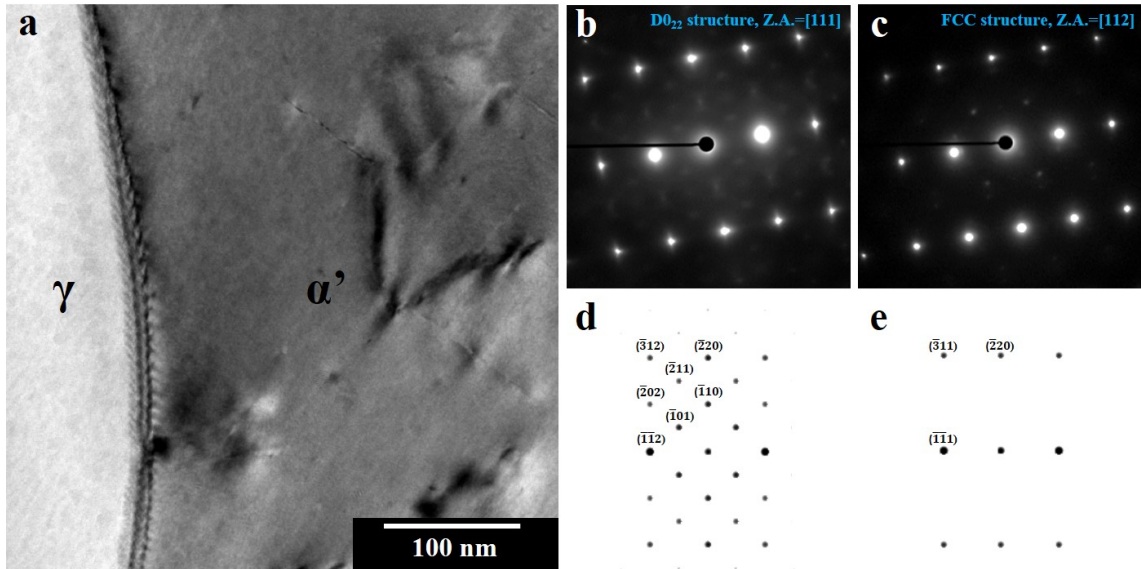
*Figure 4.4 (a) HRTEM cross-section of the γ-Cu₉Al₄ / α' interface after annealing at 525°C for 1h. (b) is the corresponding [111] SAED pattern of α' lattice. (c) is the [112] SAED pattern of the Cu lattice underneath. (d) and (e) are the simulated SAED patterns for (b) and (c) respectively. Simulations were carried out using MacTempas software.*

**FCC (Cu)**          **D0₂₂ (α')**
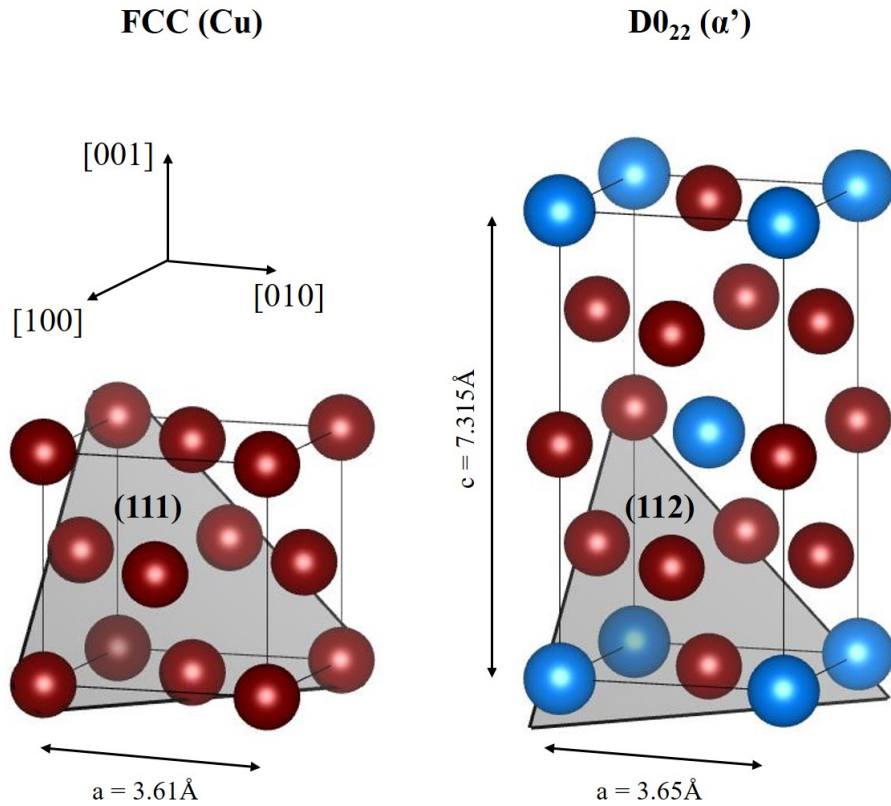


*Figure 4.5 Schematic representation of FCC and D0₂₂ crystal structures emphasizing on (111)_FCC and (112)_D022, crystallographically equivalent lattice planes. Red atoms are Cu, while blue atoms are Al positions. Drawings produced using VESTA.*

$$\delta \frac{(hkl)_{Cu}}{(hkl)_{\alpha'}} = \frac{1}{3} \sum_{i=1}^{3} \left\{ \frac{\left| d[uvw]^i_{Cu} \cos\theta - d[uvw]^i_{\alpha'} \right|}{d[uvw]^i_{\alpha'}} \right\} \times 100 \ (\%) \qquad (4.1)$$

where *(hkl)$_{Cu}$* and *(hkl)$_{\alpha'}$* are low index planes of Cu and α'; *[uvw]$_{Cu}$* and *[uvw]$_{\alpha'}$* are the low index directions on *(hkl)$_{Cu}$* and *(hkl)$_{\alpha'}$* ; *d$_{[uvw]Cu}$* and *d$_{[uvw]\alpha'}$* are interatomic spacing along *[uvw]$_{Cu}$* and *[uvw]$_{\alpha'}$* ; $\theta$ is the angle between *[uvw]$_{Cu}$* and *[uvw]$_{\alpha'}$*. The planar lattice mismatches between possible crystallographic orientation between α' and Cu are listed in Table 4.1. It is obvious that the mismatch values for all possible crystallographic orientation are less than 2% and the tetragonality component can thus be neglected. As a result, it can be reasonably well agreed upon that α' and Cu are coherent and share a cube-on-cube orientation relationship. This agrees well with the XRD data in Figure 4.1 (b) where the α' and Cu doublets were shown to exists on all diffracting planes.

*Table 4.1 Two-dimensional mismatch calculation between α' and Cu.*

| Matching Face | (100) α' // {100} Cu | | | (001) α' // {001} Cu | | | (110) α' // {110} Cu | | | (112) α' // {111} Cu | | |
|---|---|---|---|---|---|---|---|---|---|---|---|---|
| $[uvw]_{Cu}$ | [001] | [010] | [011] | [100] | [010] | [110] | [001] | [-110] | [-111] | [-110] | [-101] | [0-11] |
| $[uvw]_{\alpha'}$ | [001] | [010] | [012] | [100] | [010] | [110] | [001] | [-110] | [-112] | [-110] | [-102] | [0-12] |
| $d_{Cu}$ | 3.610 | 3.610 | 5.105 | 3.610 | 3.610 | 5.105 | 3.610 | 5.105 | 6.252 | 5.105 | 5.105 | 5.105 |
| $d_{\alpha'}$ | 3.658 | 3.650 | 5.167 | 3.650 | 3.650 | 5.162 | 3.658 | 5.162 | 6.326 | 5.162 | 5.167 | 5.167 |
| δ (%) | | 1.20 | | | 1.10 | | | 1.19 | | | 1.17 | |

4.4 Conclusion

The findings made in this investigation reveal the presence of D0$_{22}$ ordering at high-temperature, within what is considered α-Cu(Al) concentration range. A very similar D0$_{22}$-based phase is already known to exists in the Al-Cu binary system: α$_2$-Cu$_3$Al. However, the phase diagram shows that it decomposes peritectoidally at 363°C, more than 250°C

lower than in our experiments, and exists within the composition range 22-24at.% Al. Consequently, it remains unclear whether α' is an entirely different entity or if it is the result of ordering within α-Cu(Al). In interdiffusion conditions, the progressive and directional supply of Al atoms from the thin film towards the Cu bulk might enhance the ordering process and make α' to be long-range-ordered (LRO). This concept is analogous to second-order phase transition where a continuous increase in SRO throughout the crystal ultimately leads to LRO. Further, α' and α-Cu(Al) were determined to be coherent, with no clear boundaries seen under HRTEM, excluding the involvement of a nucleation and growth mechanism. The absence of nucleation could also be explained by the fact that the formation of α' nuclei would involve long-distance atomic rearrangement, while only local atomic rearrangement is necessary for an ordering process involving second-order phase transition. Indeed, the diffusivity of Al atoms inwards, across IMC layers such as $\gamma$-$Cu_9Al_4$ and β, is slowed down, hence local atomic rearrangement upon penetrating the Cu bulk might be kinetically favorable. Additional thermodynamic computations on phase transformation and order-disorder transition, part of which is ongoing in our lab, would be helpful to fully fathom these new findings.

Chapter 5: Diffusion Induced Solid State Epitaxial Growth and Failure Mechanism in Cu-

Al Diffusion Couple

5.1 Introduction

In the previous chapter, the existence of the α' phase, a $D0_{22}$-based phase responsible for inducing interfacial failure in Cu-Al diffusion couples was demonstrated. Now, this chapter will provide more in-depth experimental evidence suggesting that α' grows on Cu in a hetero-epitaxial manner, and that crack nucleation happens after the interface strain becomes too high for the system to bear. The hypothesis was initially made in Chapter 3 based on the fact that both Cu and α' have a very similar crystal structure with small lattice mismatch. Figure 5.1 shows the schematic representation of a typical interface evolution in a hetero-epitaxially grown thin film. In such a case, the smaller the lattice mismatch between the substrate and film, the better long-term reliability can be achieved.
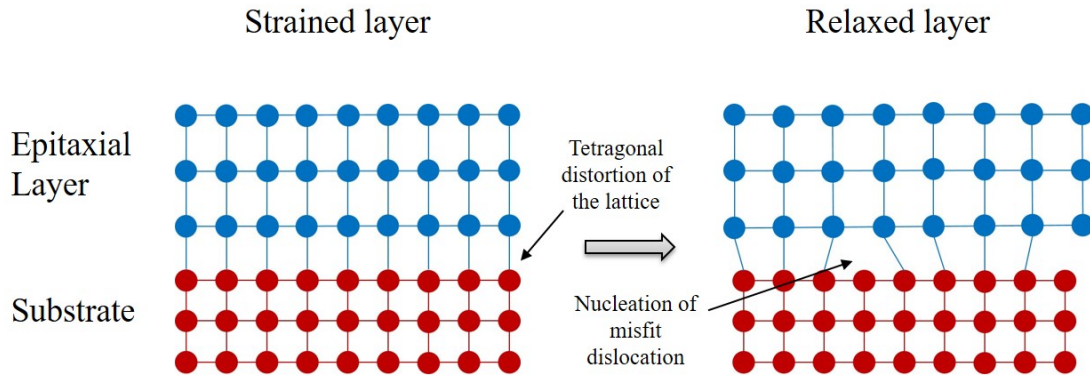


*Figure 5.1 Schematic representation of the evolution of heteroepitaxial structures.*

In our specific case, the Cu substrate is the one with the smaller lattice parameter, hence it will be subjected to elastic tensile stress in order to maintain the lattice continuity across the interface. Inversely, α' will be subjected to compressive stress. In a fully

coherent interface, the resulting compressive strain will be accommodated by some degree of tetragonal distortion normal to the interface (see Figure 5.1). The strain energy is a function of the thickness of the epitaxial layer. Figure 5.2 shows a simplified hypothetical plot of the energy evolution as a function of the thickness of the grown layer.
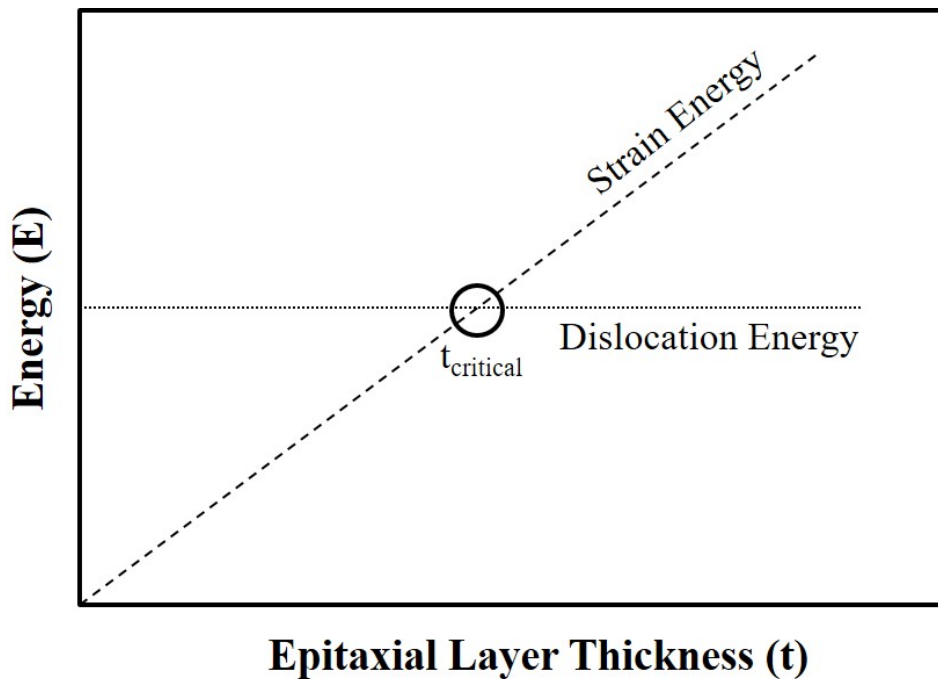


*Figure 5.2 Hypothetical plot representing the energy evolution as function of the epitaxial layer thickness.*

From this very straightforward plot, it can de deduced that it is first energetically favorable for the system to maintain the interface coherency; this is known as strained layer. Unlike the dislocation energy, the strain energy is increasing with the layer thickness until a critical thickness $t_c$ is reached. At this crossover point the strain energy becomes too significant, therefore the system will nucleate misfit dislocations at the interface; it is known as relaxed or semi-coherent layer. As the misfit dislocation density increases to relax the elastic strain, this ultimately leads to an incoherent interface and delamination of the epitaxial film.

Moreover, in the Cu-Al wire bonding configuration, thermal stress arising from the difference in thermal expansion coefficients between phases plays a significant role in the interface dynamics leading to crack formation.

In order to decisively prove that this hetero-epitaxial failure mechanism applies to the Cu-Al diffusion couple, an approach using a monocrystalline substrate was employed. A Cu (111) single crystal was coated with a 1 μm thick Al thin film, and interdiffusion was induced by heat treatment at 525°C for 30min. The (111) orientation of the substrate was chosen as it would result in maximal x-rays intensity for Bragg-Brentano and RC XRD measurements. As hypothesized, the $\alpha$' phase layer is observed to form and grow epitaxially with respect to the (111) Cu single crystal. For the sake of simplicity in indexing and better global understanding, $\alpha$' will be approximated as an FCC-based phase in this last chapter of the work. Amazingly, the complex metallic alloy (CMA) $\gamma$-$Cu_9Al_4$ also seems to display epitaxial relationship with $\alpha$' phase beneath. Advanced XRD and TEM characterizations show that it exhibits a Nishiyama-Wassermann OR with the FCC-based $\alpha$' phase, such as: $(111)_{\alpha'}$ // $(011)_\gamma$ and $[11\overline{2}]_{\alpha'}$ // $[01\overline{1}]_\gamma$.

## 5.2 Methodology

A commercially available Cu (111) single crystal of dimensions 10x10x1.0mm was used as substrate material. The purity is exceeding 99.99% and the orientation is <111> +/- $2^o$. A 1μm Al thin film was sputtered using the same conditions and equipment as for polycrystalline diffusion couples in Chapters 3 and 4. The thermal treatment for inducing interdiffusion was conducted in a high-temperature tube furnace at 525°C for 30min. For

the entire duration of aging, the tube was filled with a continuous flow of 95% $N_2$-5% $H_2$ forming gas to prevent oxidation.

## 5.3 Results & Discussion

### 5.3.1 XRD analysis

Analysis carried out on the single crystal Cu-Al diffusion couple indicates that α', but also γ-$Cu_9Al_4$, have an epitaxial relationship with the Cu substrate. The heat treatment at 525°C for 30min was chosen to induce sufficient IMC growth without risking dissolving all IMC phases into the Cu solid solution. Figure 5.3 shows the XRD pattern obtained after thermal treatment. The RC measurements of α' and γ-$Cu_9Al_4$ are displayed in the inset.
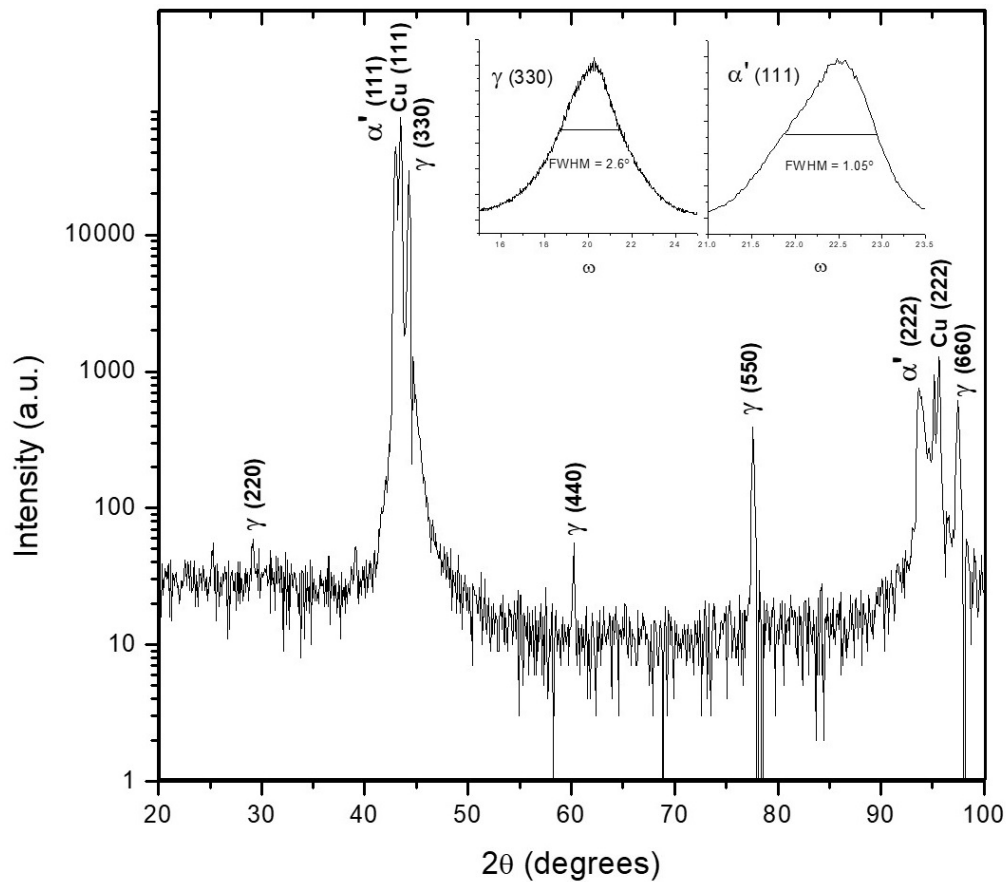


*Figure 5.3 XRD pattern after annealing at 525ºC for 30min. Inset are the RC.*

One can notice that the tetragonal $\theta$-CuAl$_2$ is absent, meaning it has already been dissolved into the more Cu-rich IMC $\gamma$-Cu$_9$Al$_4$ and $\alpha$'. This is in good agreement with past results obtained in polycrystalline interdiffusion studies, where it proved to be short-lived in these conditions. The XRD pattern decisively shows that $\alpha$' indeed has an epitaxial relationship with the Cu substrate; only the {111} family of planes can be seen as $\alpha$'/Cu doublet, while other characteristic FCC diffracting planes such as (200), (220), and (311) are absent. The lattice parameter of $\alpha$' was re-calculated (a = 3.65Å) and perfectly matches the previous data gained from polycrystalline diffusion couples. The sharp (111) peak obtained from RC measurement (inset) has a FWHM of about 1°, indicating a very low degree of mosaicity with minimal misorientation. From the RC, the misfit dislocation density using the Hirsh model was estimated to be about 5.59 x 10$^{10}$ / cm$^2$, or approximately 1 dislocation per 10,000 two-dimensional unit cell. Unexpectedly, $\gamma$-Cu$_9$Al$_4$ also seems to display an epitaxial behavior while growing on FCC-based structures; as seen in Figure 5.3, only the {110} family of planes diffracts. The RC measurement carried out on the main (330) diffraction plane shown in the inset indicates a sharp peak having a FWHM of about 2.6°. A 2.6° degree of mosaicity can seem high, however it is not considered unusual for a CMA having such a big lattice parameter (a = 8.7Å). Since rocking curve measurements only provide information regarding the out-of-plane epitaxial relationship, pole figure measurements were carried out to determine the in-plane epitaxial relationship of $\gamma$-Cu$_9$Al$_4$ and $\alpha$'. Figure 5.4 (a) and (b) are the (111) and (311) pole figures obtained from $\alpha$', and they represent the typical epitaxial behavior of a (111) oriented FCC-based phase. The (330) and (222) pole figures of $\gamma$-Cu$_9$Al$_4$ are then shown in Figure 5.4 (c) and (d), respectively. The (222) pole figure exhibits a 6-fold symmetry having an angle of about

60° between each diffraction intensity. The stereographic projection of a (110) oriented cubic crystal is only supposed to show two (222) spots, symmetrical with respect to the center of the pole figure. Hence, these four additional diffraction intensities, equally spaced along the in-plane rotation angle, suggests the presence of rotational epitaxy within the γ-Cu₉Al₄ layer. Definitive evidence would come from HRTEM micrographs coupled with SAED / fast Fourier transform (FFT) patterns. Additionally, further characteristics regarding γ-Cu₉Al₄ crystal structure need to be introduced in order to comprehend how such a phase can display an epitaxial behavior when forming by solid-state interdiffusion.
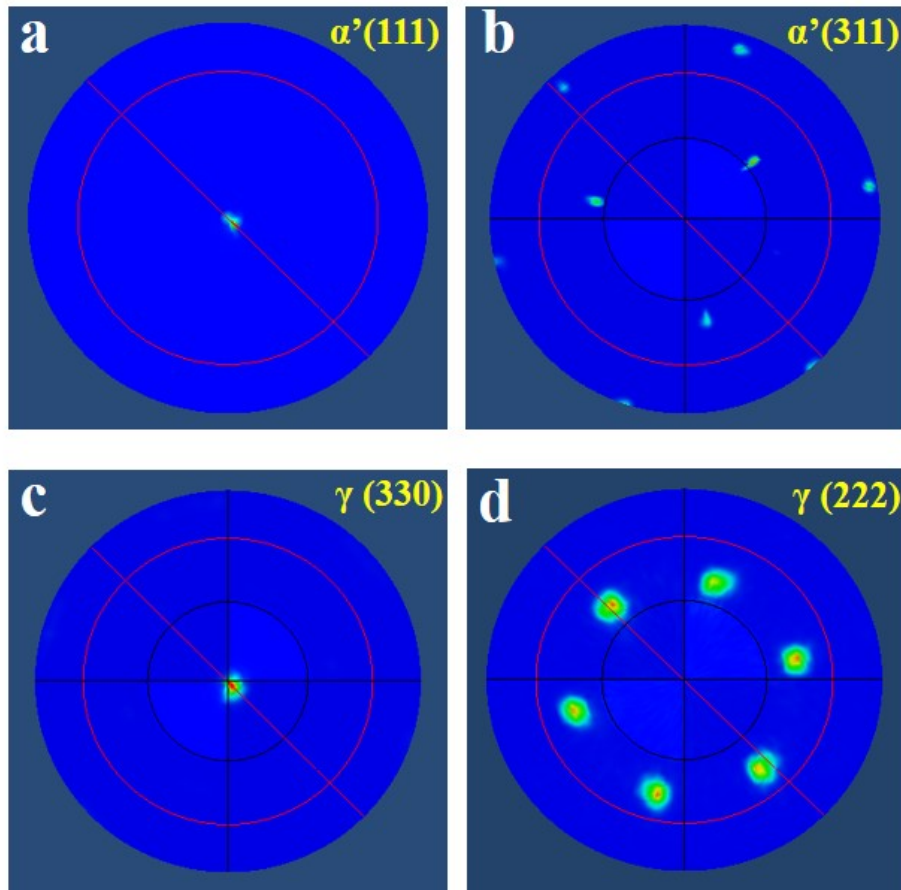


*Figure 5.4 XRD pole figures. (a) and (b) are the (111) and (311) pole figures of α'. (c) and (d) are the (330) and (222) pole figures of γ-Cu₉Al₄.*

### 5.3.2 γ-Cu$_9$Al$_4$ as a Complex Metallic Alloy

γ-Cu$_9$Al$_4$ is known as a CMA, but also as a quasicrystal approximant. Quasicrystal IMC phases are ordered but not periodic. They can entirely fill the space, but don't have translational symmetry. Approximants such as γ-Cu$_9$Al$_4$ are related phases but do have a periodic structure, and their chemical composition is very close to the quasicrystalline phases [83]. They are characterized by their large unit cell containing tens of atoms up to thousands of them. Many studies have been carried out on these materials, motivated by their potentially interesting properties, such as poor wetting, excellent corrosion resistance, and low-friction coefficients [84]. According to Gaudry et al., γ-Cu$_9$Al$_4$ has a supercell containing 52 atoms based on 3 x 3 x 3 B2 structure (ordered BCC) having two vacancies, that can also be regarded as composed by two 26-atom clusters. γ-Cu$_9$Al$_4$ is a Hume-Rothery IMC phase stabilized by the Fermi sphere-Brillouin zone interaction [85]. Its unit cell is displayed in Figure 5.5.
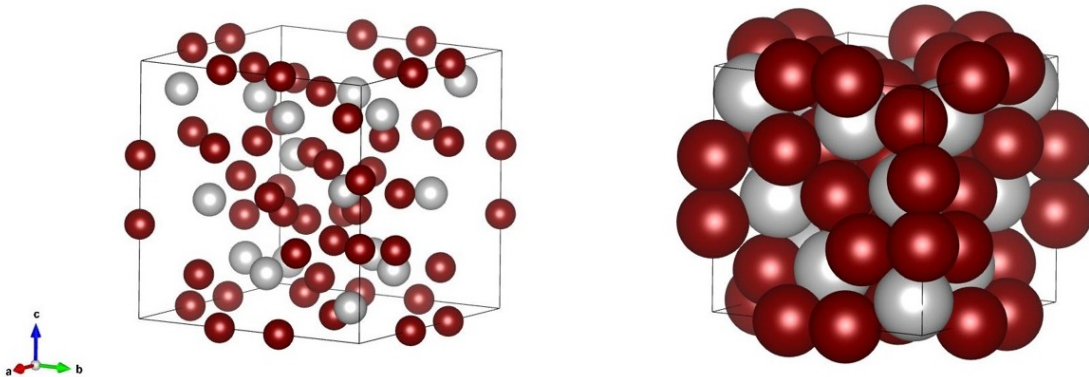


*Figure 5.5 γ-Cu$_9$Al$_4$ unit cell. Red atoms are Cu and grey atoms are Al. Drawings produced using VESTA.*

Based on the XRD pattern gained from single crystal interdiffusion, the most densely packed {110} planes are the ones exhibiting an epitaxial behavior with the close-packed

{111} planes of α' underneath. Therefore, careful examination of γ-Cu$_9$Al$_4$ {110} planes atomic arrangement is crucial to fathom the alignment between the two IMCs. The [110] projection of γ-Cu$_9$Al$_4$ structure is shown in Figure 5.6 where two distinct kinds of (110) planes are stacked: corrugated and flat planes. When the crystal is observed from this specific direction, one can notice that both the corrugated and flat planes have a reflectional symmetry with respect to the line at the center. The unit cell of a corrugated plane is formed by 12 Cu atoms and 6 Al atoms. Flat planes also contain 12 Cu atoms but only 4 Al atoms [83]. The resulting density of corrugated planes is much higher and make these planes more suitable for sustaining lattice continuity along the γ-Cu$_9$Al$_4$ / α' interface.
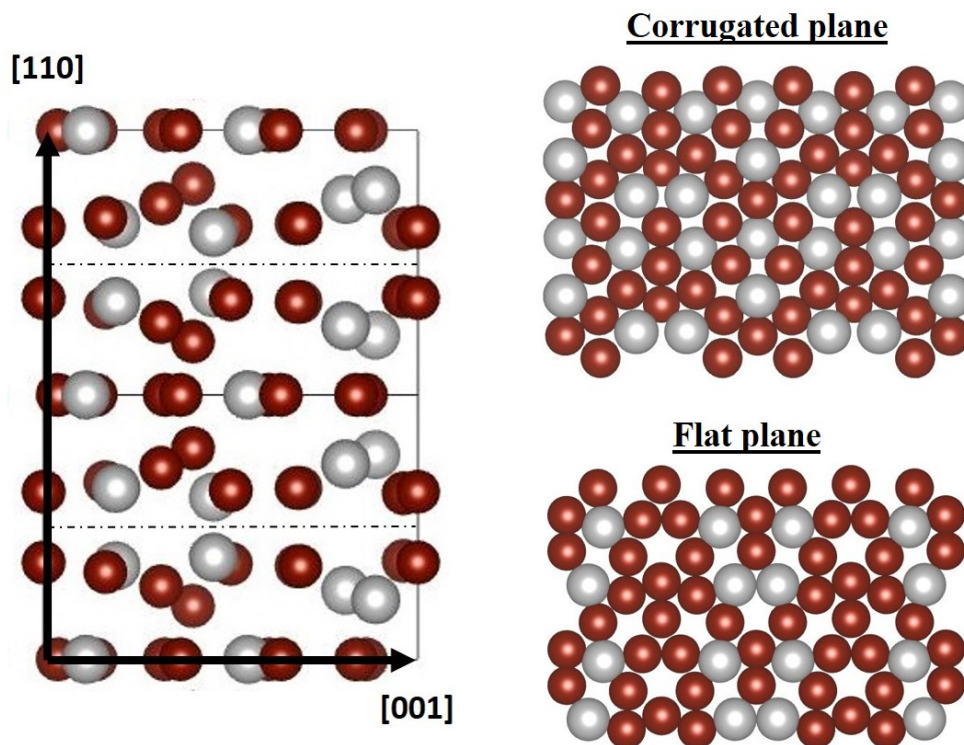


Figure 5.6 [110] projection of γ-Cu$_9$Al$_4$ unit cell. Atomic arrangement for corrugated planes (top right) and flat planes (bottom right). Red atoms are Cu and grey atoms are Al. Drawings produced using VESTA.

75

Figure 5.7 shows a hypothetical crystallographic simulation of the OR between $\gamma$-$Cu_9Al_4$ and $\alpha'$, according to the information thus far extracted from XRD data: $(110)_\gamma$ // $(111)_{\alpha'}$. For the sake of simplicity, $\alpha'$ was modeled as a stoichiometric $L1_2$ compound. Additionally, a densely packed corrugated $\gamma$-$Cu_9Al_4$ (110) plane was determined to be a better fit for simulating the OR.
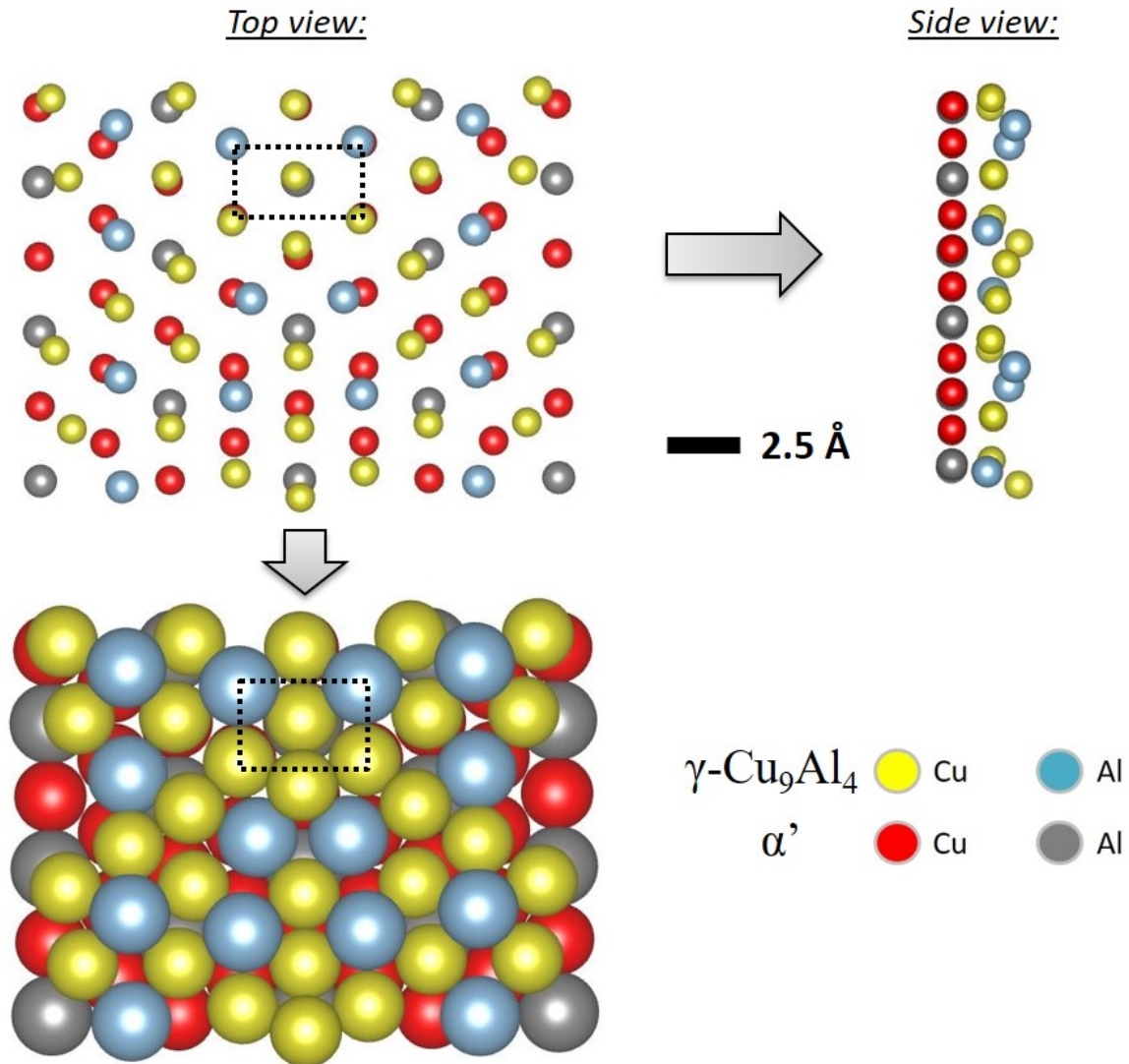


*Figure 5.7 Speculative crystallographic representation of $\gamma$-$Cu_9Al_4$ and $\alpha'$ stacking with a $(110)_\gamma$ // $(111)_{\alpha'}$ OR. Dashed rectangle represents a typical BCC (110) motif. Drawings produced using VESTA.*

As previously mentioned, $\gamma$-$Cu_9Al_4$ has a structure derived from a B2 CsCl-like structure. The black dashed rectangle shown in Figure 5.7 shows the typical (110) motif of a BCC-like structure. In a FCC-based structure, the (111) plans also exhibit a very similar sub-motif within the main hexagonal motif. By looking back carefully at the stacking in Figure 5.7, it is not unreasonable to believe that a lattice continuity between $\gamma$-$Cu_9Al_4$ and $\alpha$' exists, should elastic interfacial stress be added.

### 5.3.3 HRTEM Analysis of Orientation Relationships

HRTEM analysis was carried out on the cross-section of the single crystal diffusion couple. HRTEM and SAED/FFT patterns investigation is the most powerful way to characterize the OR between phases both morphologically and structurally. Figure 5.8 shows the low-magnification TEM micrograph of the overall diffusion zone, along with a EDS line profile analysis. From the innermost layer, $\alpha$' (17-20 at.% Al) is growing onto the Cu substrate, then two different layers of $\gamma$-$Cu_9Al_4$ (30 at.% Al) are stacked on the outermost part of the diffusion couple. Hereafter they will be called $\gamma_a$ and $\gamma_b$.
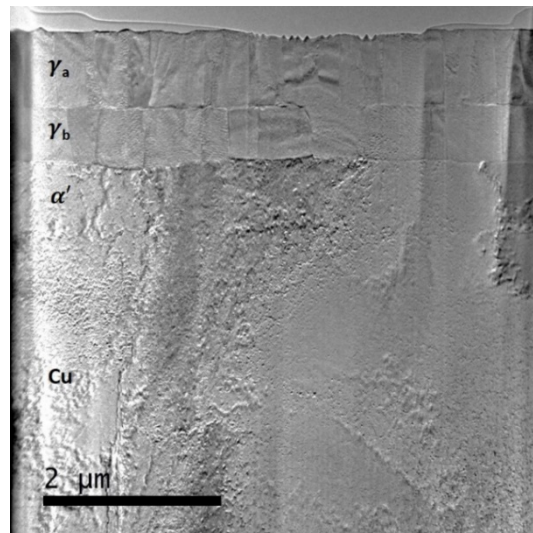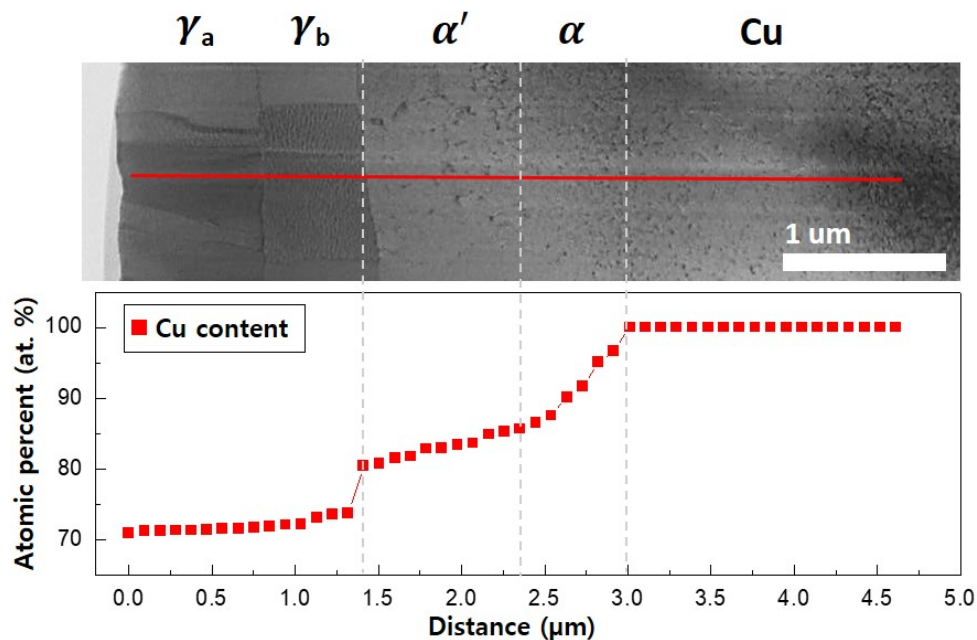
*Figure 5.8 Low magnification TEM micrograph of the cross-section of the single crystal diffusion couple, and EDS line profile analysis.*

No clear contrast can be seen under TEM between α' and Cu, as they only slightly differ in both composition and crystalline structure. The underlying explanation related to the presence of $\gamma_a$ and $\gamma_b$ is closely correlated to the formation and subsequent dissolution of $\theta$-CuAl$_2$. As previously claimed in Chapter 3, this Al-rich IMC is the first ever to form within the Al thin film. It is based on a body-centered tetragonal structure (BCT) that cannot reasonably share any sort of particular OR with either γ-Cu$_9$Al$_4$, α' or Cu. Also, note that $\gamma_a$ has the exact thickness as the initial Al film (1μm). Therefore, it is believed that the lattice disturbance caused by the initial transformation of $\theta$-CuAl$_2$ into γ-Cu$_9$Al$_4$ is the reason why $\gamma_a$ might have a different OR than $\gamma_b$, directly nucleating onto the Cu substrate side.

Figure 5.9 (a) is the HRTEM image of the $\gamma_a$ / $\gamma_b$ interface, and the corresponding SAED pattern is shown in (b). Figure 5.9 (c) is the inverse fast Fourier transform (IFFT) of (a), showing the parallel lattices planes in more detail.



*Figure 5.9 (a) HRTEM micrograph of the $\gamma_a$ / $\gamma_b$ interface. Insets are the FFT. (b) Equivalent SAED pattern taken at the same interface. (c) IFFT filtered image of the interface showing the parallel lattice planes of $\gamma_a$ and $\gamma_b$.*

From the FFT and SAED pattern, the OR between the two $\gamma$-Cu$_9$Al$_4$ can be easily established. According to the FFTs and SAED pattern, the two zone axes $\gamma_a$ [$3\bar{1}1$] and $\gamma_b$

$[01\bar{1}]$ are perfectly aligned, and the {110} family of planes of both $\gamma$-Cu$_9$Al$_4$ is parallel, therefore the OR is as follows: $[3\bar{1}1]\gamma_a$ // $[01\bar{1}]\gamma_b$ and $(011)\gamma_a$ // $(011)\gamma_b$. The out-of-plane OR remains the same for both phases, which explains why only {110} planes were detected from XRD analysis. The rotational epitaxy defined as $[3\bar{1}1]\gamma_a$ // $[01\bar{1}]\gamma_b$ has an angle of about 64°, and emerges from the fact that $\gamma_a$ formed and grew on $\theta$-CuAl$_2$, an IMC that had no possible coherency with the surrounding phases.

Now, one of the most crucial aspects of this work is to investigate the $\gamma_b$ / $\alpha$' interface dynamics, and comprehend how a CMA and quasicrystal approximant such as $\gamma$-Cu$_9$Al$_4$ can maintain a lattice coherency, and epitaxially grow on FCC-based structures. Previous XRD data showed that $\gamma$-Cu$_9$Al$_4$ (330) plane has a d-spacing comparable to those (111) planes of $\alpha$' and Cu. Further, the superstructure $\gamma$-Cu$_9$Al$_4$ is based on BCC-like sublattice. Several well-known OR models between FCC and BCC phases have been reported in the past few decades. Among them, the Kurdjumov-Sachs (KS), Bain (martensitic transformation), and Nishiyama-Wassermann (NW) are the most commonly encountered [86]. It is well agreed in these models that the closed-packed {111}$_{FCC}$ are parallel to the most densely packed {110}$_{BCC}$. However, the main difference between the KS and NW assumptions is related to the direction to which these parallel planes face:

Kurdjumov-Sachs: {111}$_{FCC}$ // {110}$_{BCC}$ ; <110>$_{FCC}$ // <111>$_{BCC}$

Nishiyama-Wassermann: {111}$_{FCC}$ // {110}$_{BCC}$ ; <112>$_{FCC}$ // <110>$_{BCC}$

These two OR can seemingly look very different, but actually are separated only by 5.23° [87]. Alternative OR have been shown to exist, as it is quite often the case that experimental results do not perfectly match these two pioneer models.

The HRTEM micrograph taken at the $\gamma_b$ / $\alpha'$ interface is shown in Figure 5.10 (a), while the corresponding SAED pattern is displayed in (b). Figure 5.10 (c) is a IFFT close-up, showing the interface in more detail.
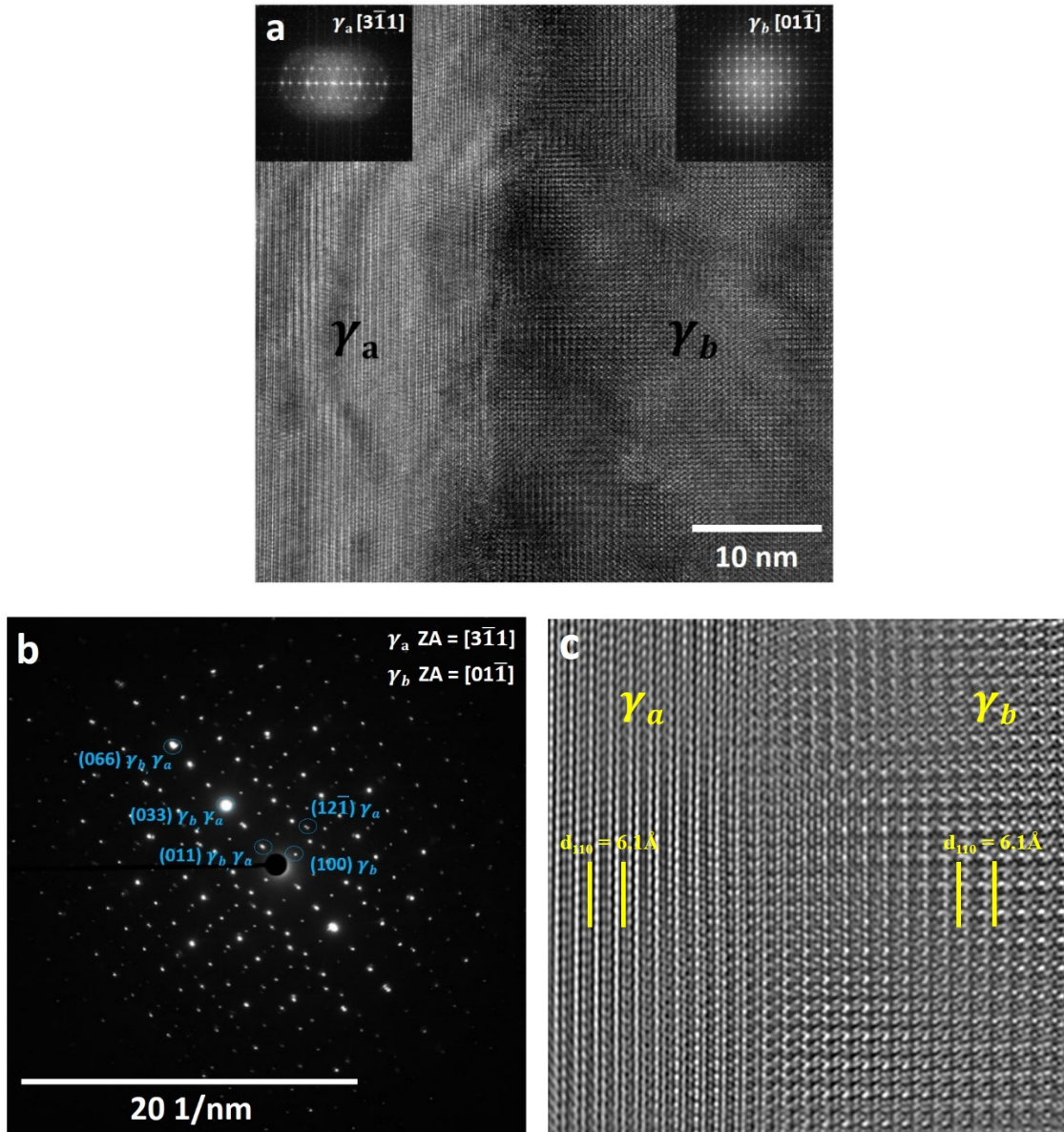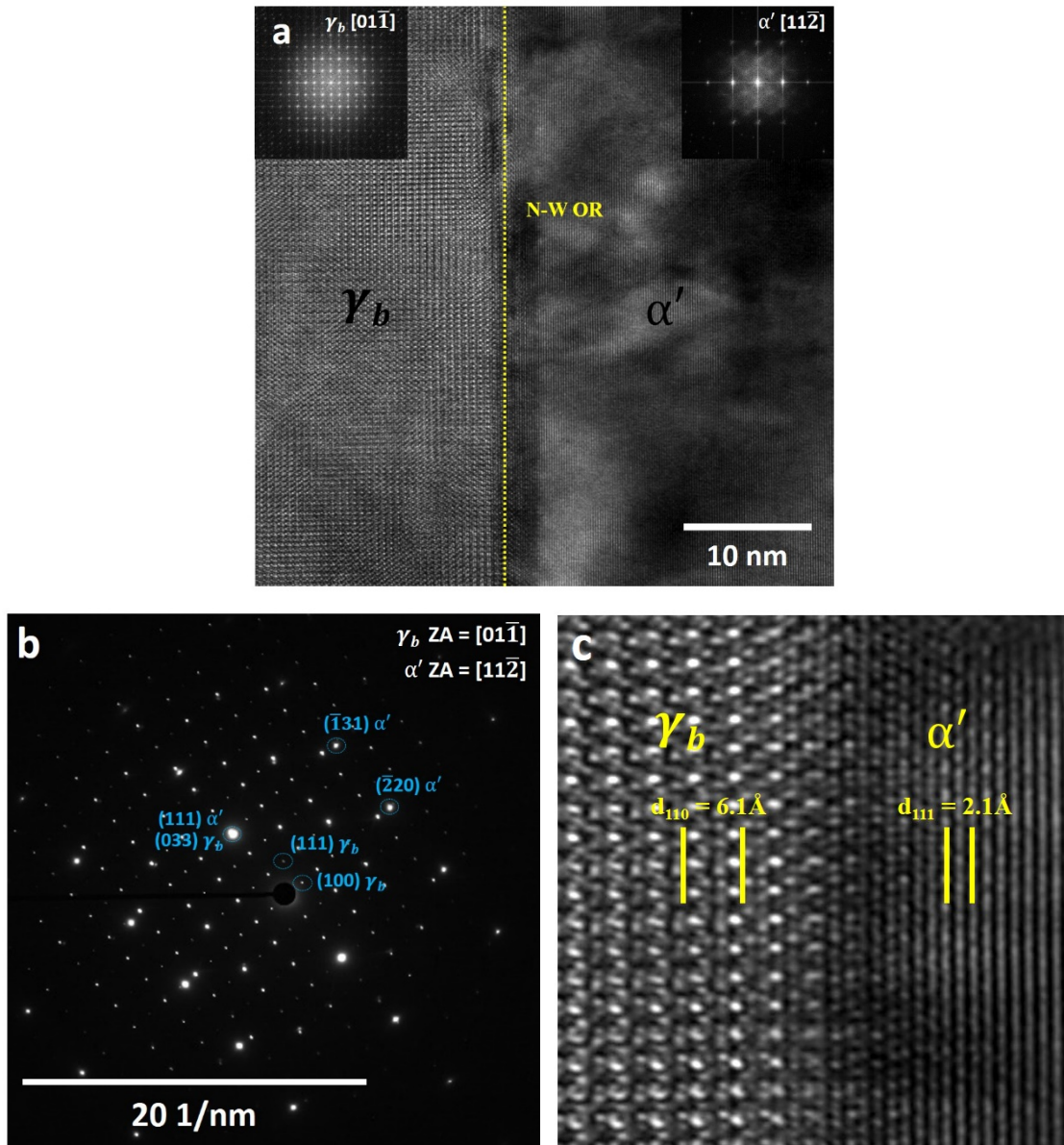


*Figure 5.10 (a) HRTEM micrograph of the $\gamma_b$ / $\alpha'$ interface. Insets are the FFT. (b) Equivalent SAED pattern taken at the same interface. (c) IFFT filtered image of the interface showing the parallel lattice planes of $\gamma_b$ and $\alpha'$.*

The HRTEM image displays a very flat interface with no apparent corrugation. The FFT taken on the $\alpha'$ side of the interface corresponds to a <211> zone axis of a FCC-based

phase, while the one on the $\gamma_b$ side is the same <110> zone axis as previously confirmed. From the FFT computation, both zone axes seem to be perfectly aligned. Figure 5.10 (b) decisively reveals the perfect superimposition of $\gamma_b$ [01$\overline{1}$] with $\alpha$' [11$\overline{2}$]. Additionally, (033)$\gamma_b$ is shown to be absolutely parallel to (111)$\alpha$'. This is in good agreement with the XRD data that showed $\gamma$-Cu$_9$Al$_4$ (330) plane having a d-spacing negligibly smaller than the (111) plane of $\alpha$'. At this stage it can be comfortably claimed that the CsCl-based CMA $\gamma_b$ and $\alpha$' obey the NW OR: (111)$_{\alpha'}$ // (011)$_\gamma$ and [11$\overline{2}$]$_{\alpha'}$ // [01$\overline{1}$]$_\gamma$. To better visualize the matching between these two phases, an atomic-scale illustration of one of the possible variants of the NW OR is shown in Figure 5.11. To the best of our knowledge, such specific OR induced by solid-state interdiffusion was never demonstrated before. On the other hand, it is important to mention that we do not think this epitaxial relationship is possible in cases of substrate orientation other than Cu (111). Any specific OR between $\gamma_b$ and $\alpha$' wasn't initially expected, and it is highly unlikely that other Cu atomic planes could obey an OR with $\gamma$-Cu$_9$Al$_4$ (011).
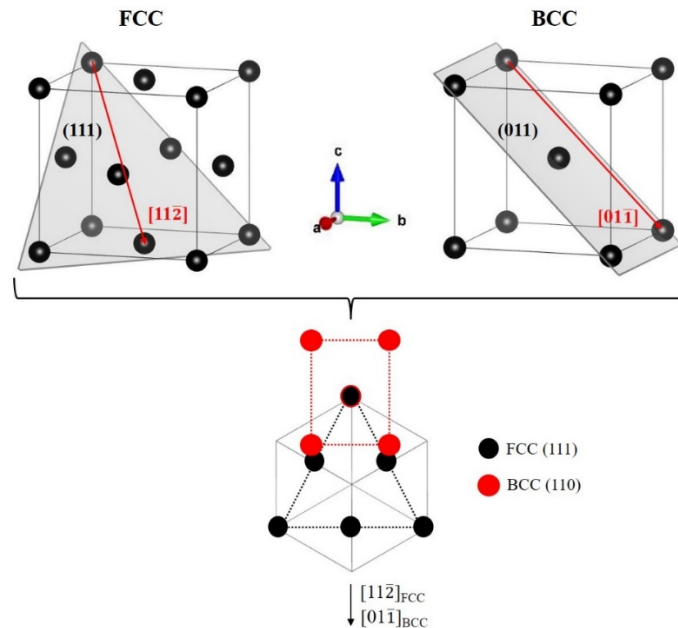


*Figure 5.11 Illustration of the Nishiyama-Wassermann orientation relationship.*

Finally, the reason for pursuing this investigation was to understand the interface dynamics between Cu and the IMC phase responsible for causing crack initiation in Al-Cu diffusion couple, α'. Unlike γ-$Cu_9Al_4$, one would expect α' to obey a cube-on-cube OR with Cu regardless which atomic planes are involved; Chapter 3 XRD results carried out on polycrystalline diffusion couples showed the presence of α'/Cu doublet for each diffraction peak. This diffraction behavior is typical of strained layer epitaxially grown. In Chapter 4, no clear boundaries between α' and Cu could be established. The low magnification TEM picture pointing out where the interfacial analysis was executed is shown in Figure 5.12 (a), while (b) is the high resolution HRTEM and corresponding FFT.
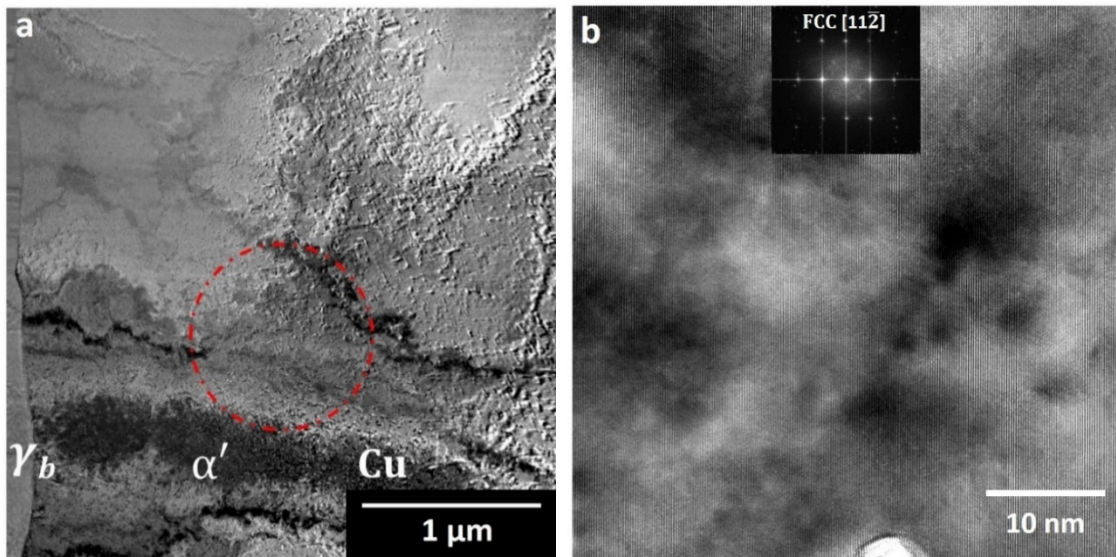


*Figure 5.12 (a) Low magnification TEM micrograph of the α' / Cu interface. The red sphere indicates where the HRTEM picture shown in (b) was taken.*

From Figure 5.12 (b), no real contrast difference between α' and Cu can be seen. This is due to the extreme similarity in crystal structure, added to the likelihood that *α'* formed by second-order phase transition, excluding classical nucleation and growth mechanism. The resulting diffused interface is almost impossible to resolve with TEM. No misalignment or rotation was visible. Hence, in this case *α'* and *Cu* obey a cube-on-cube OR, such as: $(111)_{\alpha'}$

// $(111)_{Cu}$ ; $[11\bar{2}]_{\alpha'}$ // $[11\bar{2}]_{Cu}$. This HRTEM analysis of $\alpha'$ / $Cu$ interface confirms what has

been proposed in Chapter. 3 as a plausible failure mechanism in Cu-Al diffusion couple.

Indeed, the short aging treatment operated on the Al-coated Cu (111) single crystal proved

the epitaxial growth of a strained $\alpha'$ layer, so aging time-dependent degradation of the

interface coherency, eventually leading to delamination can be reasonably well explained.

The overall stacking of IMC layers after interdiffusion is modeled in Figure 5.13.
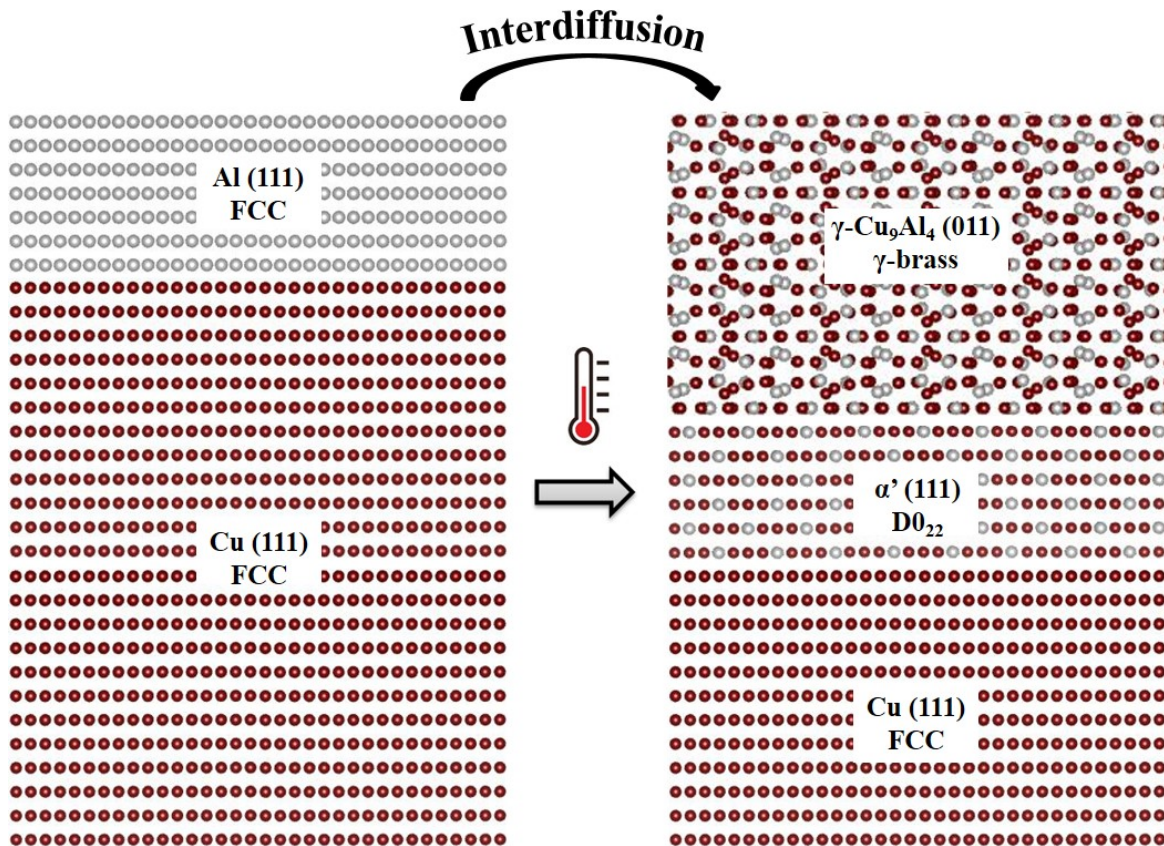


*Figure 5.13 Overall staking of the IMC layers obtained after interdiffusion. Drawing produced using VESTA.*

### 5.3.4 Discussion

The findings made in this investigation allow confirmation of the failure mechanism observed in Cu-Al diffusion couple, on top of revealing valuable information related to the epitaxial growth of IMC phases induced by solid state interdiffusion. In the first part of this Chapter 5, XRD analysis pointed out the out-of-plane epitaxial relationship of both $\gamma$-$Cu_9Al_4$ (110) and $\alpha$' (111) with respect to the Cu (111) substrate. Subsequent RC measurements, resulting in sharp peaks with only small misorientaion for both IMC phases, further confirmed the occurrence of epitaxy. Indeed, a RC incrementally measures the x-ray intensity coming from a specific diffraction peak at 2$\theta$ angles slightly off the ideal diffraction condition. When a material is polycrystalline and randomly oriented, the total x-ray intensity collected by the detector will cancel out and the RC will be flat. On the other hand, a sharp peak can only be attained from a material exhibiting either strong fiber texture or single crystal behavior.

Additionally, HRTEM micrographs coupled with SAED/FFT pattern analysis yielded unexpected results related to what appears to be the formation of two epitaxial $\gamma$-$Cu_9Al_4$: $\gamma_a$ and $\gamma_b$. $\gamma_b$ nucleated on the Cu side of the diffusion couple while $\gamma_a$ layer forms by dissolving $\theta$-$CuAl_2$ within the initial 1$\mu$m Al thin film boundary. It was found that the in-plane rotational epitaxy between $\gamma_a$ and $\gamma_b$ is about 64°, such as: $[3\bar{1}1]\gamma_a$ // $[01\bar{1}]\gamma_b$ ; $(011)\gamma_a$ // $(011)\gamma_b$. It is a well-known fact that $\{110\}$ planes of $\gamma$-$Cu_9Al_4$ are the densest and have a low surface energy that makes for a greater stability. Thus, the formation and growth of $\gamma$-$Cu_9Al_4$ layer along <110> direction can be explained as a way to minimize the surface energy. Another valuable finding from this investigation came from the discovery of a NW

OR between $\gamma_b$ and $\alpha$'. More generally, identification of ORs is of primary importance in the comprehension of solid-phase transformation. Our HRTEM analysis confirms the possibility of maintaining a strained and semi-coherent interface between a simple FCC-based structure and an intermediately complex $\gamma$-brass structure, grown over a 1μm thickness. Although considered as a very intricate structure by usual IMC standards, it was shown that $\gamma$-$Cu_9Al_4$ can be subdivided as simple CsCl (B2) sub-cells, making the NW OR between BCC and FCC phases possible.

The hetero-epitaxial growth of intermetallic phases by mean of interdiffusion doesn't follow the classical nucleation and growth theory where nuclei of random orientation form at a given surface / interface. Available literature on the subject is scarce, however P.J. Shang et al. have previously showed the possibility to grow columnar $Cu_3Sn$ grains with specific OR on single crystalline Cu substrate after solder reflow (liquid-solid interface) [88]. It is claimed that the specific OR is maintained by the simultaneous nucleation of $Cu_3Sn$ and the directional supply of the reacting elements. However, in our case it is a solid-state reaction that cannot take advantage of the "amorphousness" of the liquid to epitaxially grow an IMC on the solid substrate. Therefore, here is presented a suggested mechanism explaining this epitaxial growth:

- A supersaturated solid solution is first formed when the Cu matrix is enriched in Al atoms.
- Stable $\gamma$-$Cu_9Al_4$ nuclei form. Cu is expected to have a higher surface energy than the CMA $\gamma$-$Cu_9Al_4$, hence it is predicted that $\gamma$-$Cu_9Al_4$ will have a very low contact-angle with the Cu substrate [89]. High-wetting and absence of crystallographic

defects in the Cu single crystal will promote homogeneous nucleation: the nuclei will randomly nucleate along the interface, propagate laterally and merge.

- In order to decrease the interfacial energy, initial $\gamma$-$Cu_9Al_4$ nuclei will form along (110) to maintain lattice continuity with Cu (111). This gives rise to the Nishiyama-Wassermann OR between Cu (111) planes and BCC-like sub-cell of $\gamma$-$Cu_9Al_4$ (110) planes.

- The initial continuous $\gamma$-$Cu_9Al_4$ (110) layer eventually grows normal to the interface in a diffusion controlled regime.

Even though it is out of the scope of this study, it should be noted that epitaxially grown {110} $\gamma$-$Cu_9Al_4$ can be of great interest in industrial applications. As previously stated, quasicrystals and their approximants can be particularly useful as functional coating providing high corrosion and wear resistance. Additionally, they can also be used as intermediate layer, providing better adherence properties for the growth of the more complex quasicrystalline structures [90].

Finally, demonstration was made that $\alpha$' is indeed growing epitaxially on Cu, by means of solid-state interdiffusion. The $\alpha$' layer of about $1\mu$m thickness displays a perfect cube-on-cube OR with the Cu (111) substrate. In light of these results, we can reasonably assume that $\alpha$' should be maintaining such epitaxy regardless of the substrate orientation in polycrystalline diffusion couples. Therefore, the proposed interface failure mechanism in Cu-Al diffusion couple is compatible with the growth of this strained $\alpha$' layer, progressively reaching a critical thickness triggering relaxation and eventual crack nucleation.

## 5.4 Conclusion

To summarize, the interdiffusion experiment performed on a Cu (111) single crystal PVD coated with a 1μm thick Al thin film reveals two main discoveries. First, we showed that the CMA γ-Cu$_9$Al$_4$ (110) could be epitaxially grown over a 1μm thickness and a large area of 1cm$^2$, on FCC-based (111) atomic planes, by solid-state interdiffusion. The OR was determined to correspond to the well-known NW, as in the case of simple BCC-FCC strain transformation. These findings may prove to be of fundamental interest, but could also help improve the surface properties of quasicrystal and approximants for potential industrial applications, by tuning their orientation. Secondly, demonstration was made that α' (111) forms epitaxially as a strained layer maintaining lattice continuity on the Cu (111) substrate. In this case the OR is a simple cube-on-cube. Consequently, the interface strain build-up triggering crack formation and eventual delamination is the suggested cause of failure in Cu-Al diffusion couples.

Chapter 6: Conclusions and Future Work

The IMC formation and growth in Al thin film Cu bulk diffusion couple was thoroughly investigated in this work. The findings made in this work can resolve several uncertainties related to the failure mechanism occurring in the Cu wire bonding technology.

Our investigations first led to the conclusion that it is not the commonly assumed $\gamma$-$Cu_9Al_4$ that triggers delamination/failure at the Cu-side of the diffusion couple. Instead, a new phase with higher Cu content, named $\alpha$', is responsible for the stress build-up at the interface. In-Depth XRD analyses revealed the epitaxial nature of the $\alpha$' layer with respect to the Cu substrate. Interface stress development in lattice matched layers is a well-known phenomenon that can result in failure when the hetero-epitaxial layer reaches a critical thickness, and it is shown that it is the main source of reliability issue in Cu-Al interdiffusion condition.

Atomic scale characterizations were subsequently carried out in order to shed light on $\alpha$' crystal structure and thermal stability. HRTEM analyses combined with SAED pattern computations carried out on high-temperature diffusion couples decisively showed that $\alpha$' has a $\alpha_2$-$Cu_3Al$-like $D0_{22}$ crystal structure, and exists at temperatures well beyond the peritectoid decomposition of $\alpha_2$-$Cu_3Al$. As with $\alpha_2$-$Cu_3Al$, the tetragonality component inherent to $D0_{22}$ structures was shown to be negligible, hence the phase can be considered as ordered FCC or $L1_2$. The diffuse superlattices indicate a non-perfect ordering, that could result from the high mobility of diffusion elements under interdiffusion conditions, and the off-stoichiometry nature of $\alpha$' that requires extensive constitutional vacancies ordering. A blurred interface with disordered $\alpha$-Cu(Al) underneath is a good indication that $\alpha$' formed via atomic rearrangement (second-order phase transition), excluding the possibility of

nucleation and growth. Further indication comes from the cube-on-cube OR it shares with Cu. Consequently, it is possible to entertain two separate formation mechanisms. First, α' could be the result of the high tendency for ordering in Al-Cu solutions combined with kinetic considerations, such as the progressive and directional supply of Al in the Cu bulk. This could explain its extremely high thermal stability (> 625ºC) compared to the stability of $\alpha_2$-$Cu_3Al$ (363ºC). A second possible mechanism is that α' is an equilibrium phase, thus possessing its own phase field. Additional Molecular Dynamics and Monte Carlo simulations are currently being performed within our research unit to fully assess α' relationship to the equilibrium phase diagram.

Another valuable finding from this work is the discovery of the possibility to epitaxially grow a CMA/quasicrystal approximant such as γ-$Cu_9Al_4$ on single crystalline Cu (111) substrate by mean of solid-state interdiffusion. XRD pole figures, along with HRTEM analyses of the interface, decisively demonstrate the epitaxial nature of γ-$Cu_9Al_4$ (110) layer on Cu (111). The semi-coherent OR was determined to be the well-known Nishiyama-Wassermann OR between BCC and FCC phases. Specific OR between matrix/precipitates in stoichiometric alloys are well documented, however the occurrence of this phenomenon in an interdiffusion condition is rather unreported in the literature. The suggested underlying mechanism relies on the early stages of γ-$Cu_9Al_4$ nucleation, and the need to maintain a semi-coherent interface, which is much more energetically favorable than a totally incoherent one.

Finally, this last finding can potentially have practical implications in the industry. As surfaces of quasicrystal and approximants have peculiar properties, such as hardness

and corrosion resistance, the ability to form epitaxial coatings oriented in a desirable direction can open new opportunities for this fascinating category of materials.

# References

[1] Ivy Wei Qin: "Wire bonding tutorial", Solid State Technology: Inside for Electronics Manufacturing, Advances in Bonding Technology, July 2005.

[2] Semikron. "Wire Bonding Technology." *Your Source for Everything Power Electronics*, 23 Oct. 2012, www.powerguru.org/wire-bonding-technology/.

[3] Lemna, Boyd. "Foundry Watch: Insights into IBM's Packaging Technology." *EETimes*, 15 Oct. 2003, www.eetimes.com/document.asp?doc_id=1190826.

[4] Quin, Ivy Wei. "Wire Bonding Tutorial." *Solid State Technology*, electroiq.com/blog/2005/07/wire-bonding-tutorial/.

[5] "15 Gold And Silver Price Charts Till 2013." *Gold Silver Worlds*, goldsilverworlds.com/15-gold-silver-price-charts-2013/.

[6] "ISO - International Organization for Standardization." *ISO 26262-1:2011 - Road Vehicles -- Functional Safety -- Part 1: Vocabulary*, 13 Jan. 2015, www.iso.org/standard/43464.html

[7] Anderson, O.L., Christensen, H. and Andreatch, P., 1957. Technique for connecting electrical leads to semiconductors. *Journal of Applied Physics, 28*(8), pp.923-923.

[8] Saiki, H., Marumo, Y., Nishitake, H., Uemura, T. and Yotsumoto, T., 2006. Deformation analysis of Au wire bonding. *Journal of materials processing technology, 177*(1), pp.709-712.

[9] Hu, S.J., Lim, G.E., Lim, T.L. and Foong, K.P., 1991. Study of temperature parameter on the thermosonic gold wire bonding of high-speed CMOS. *IEEE Transactions on components, hybrids, and manufacturing Technology*, *14*(4), pp.855-858.

[10] Xu, H., Liu, C., Silberschmidt, V.V., Pramana, S.S., White, T.J., Chen, Z., Sivakumar, M. and Acoff, V.L., 2010. A micromechanism study of thermosonic gold wire bonding on aluminum pad. *Journal of applied physics*, *108*(11), p.113517.

[11] Liu, D.S. and Chao, Y.C., 2003. Effects of dopant, temperature, and strain rate on the mechanical properties of micrometer gold-bonding wire. *Journal of electronic materials*, *32*(3), pp.159-165.

[12] Zhang, X. and Tee, T.Y., 2006. Numerical and experimental correlation of high temperature reliability of gold wire bonding to intermetallics (Au/Al) uniformity. *Thin solid films*, *504*(1), pp.355-361.

[13] Murali, S., Srikanth, N. and Vath, C.J., 2003. An analysis of intermetallics formation of gold and copper ball bonding on thermal aging. *Materials Research Bulletin*, *38*(4), pp.637-646.

[14] Chen, K.H., Choi, S., Chan, C.Y. and Nigos, J.M., Agilent Technologies, Inc., 2004. *Room temperature gold wire bonding*. U.S. Patent 6,698,646.

[15] Tomiyama, S. and Fukui, Y., 1982. Gold bonding wire for semiconductor applications. *Gold bulletin*, *15*(2), pp.43-50.

[16] Hu, G., 2012, August. Comparison of copper, silver and gold wire bonding on interconnect metallization. In *Electronic Packaging Technology and High Density Packaging (ICEPT-HDP), 2012 13th International Conference on* (pp. 529-533). IEEE.

[17] Watson, Jeff, and Maithil Pachchigar. "The Extreme Environments Driving Design Innovation." *The Extreme Environments Driving Design Innovation*, 20 July 2015, www.electronicspecifier.com/mixed-signal-analog/the-extreme-environments-driving-design-innovation.

[18] Thompson, S.E. and Parthasarathy, S., 2006. Moore's law: the future of Si microelectronics. *Materials today*, *9*(6), pp.20-25.

[19] J. Friedel. Electronic structure of primary solid solutions in metals. Adv. Phys. 3, 1954, 446-507.

[20] J. D. Eshelby. The continuum theory of lattice defects. Solid State Phy. 3, 1956, 79-144.

[21] N. F. Mott. The cohesive forces in metals and alloys. Rep. Prog. Phys. 25, 1962, 218-243.

[22] A. Cottrell. An Introduction to Metallurgy. 2nd ed. London: Edward Arnold, 1975. pp. 345-347.

[23] Zhang, Y.M., Evans, J.R.G. and Yang, S., 2010. The prediction of solid solubility of alloys: developments and applications of Hume-Rothery's rules. *The Journal of Crystallization Physics and Chemistry*, *1*(2), pp.103-119.

[24] Darken, L.S. and Gurry, R.W., 1953. Physical Chemistry of Metals, Metallurgy and Metallurgical Engineering Series.

[25] Viderama, Samantha. "PERIODIC TABLE | ELECTRONEGATIVITY | NOBLE GASES." *PAULING ELECTRONEGATIVITY VALUES*, 29 Sept. 2012, secrets-of-periodic-table.blogspot.com/2012/09/pauling-electronegativity-values.html.

[26] Kodentsov, A.A., Bastin, G.F. and Van Loo, F.J.J., 2001. The diffusion couple technique in phase diagram determination. *Journal of alloys and compounds*, *320*(2), pp.207-217.

[27] Mehrer, H., 1996. Diffusion in intermetallics. *Materials Transactions, JIM*, *37*(6), pp.1259-1280.

[28] Kidson, G.V., 1961. Some aspects of the growth of diffusion layers in binary systems. *Journal of Nuclear materials*, *3*(1), pp.21-29.

[29] Nonaka, K., Sakazawa, T. and Nakajima, H., 1995. Reaction diffusion in Mg–Cu system. *Materials Transactions, JIM*, *36*(12), pp.1463-1466.

[30] He, P. and Liu, D., 2006. Mechanism of forming interfacial intermetallic compounds at interface for solid state diffusion bonding of dissimilar materials. *Materials Science and Engineering: A*, *437*(2), pp.430-435.

[31] Liu, H., Wang, H., Zhu, W., Tao, X. and Jin, Z., 2007. Prediction of formation of intermetallic compounds in diffusion couples. *Journal of materials research*, *22*(6), pp.1502-1511.

[32] Thompson, C.V., 1992. On the role of diffusion in phase selection during reactions at interfaces. *Journal of materials research*, *7*(2), pp.367-373.

[33] Turnbull, D., 1956. Solid State Physics, edited by F. Seitz and D. Turnbull (Academic Press, New York), Vol. 3, pp. 225.

[34] Porter, D.A., Easterling, K.E. and Sherif, M., 2009. *Phase Transformations in Metals and Alloys, (Revised Reprint)*. CRC press.

[35] Howe, J.M., 1997. *Interfaces in materials: atomic structure, thermodynamics and kinetics of solid-vapor, solid-liquid and solid-solid interfaces*. Wiley-Interscience.

[36] Becker, R., 1938. Nucleus formation in the separation of metallic mixed crystals. *Ann. Phys*, *32*, pp.128-40.

[37] Murray, J.L., 1985. The aluminium-copper system. *International metals reviews*, *30*(1), pp.211-234.

[38] Ponweiser, N., Lengauer, C.L. and Richter, K.W., 2011. Re-investigation of phase equilibria in the system Al–Cu and structural analysis of the high-temperature phase η 1-Al 1− δ Cu. *Intermetallics*, *19*(11), pp.1737-1746.

[39] Cooper, A.S., 1962. Precise lattice constants of germanium, aluminum, gallium arsenide, uranium, sulphur, quartz and sapphire. *Acta Crystallographica*, *15*(6), pp.578-582.

[40] Havinga, E.E., 1972. Compounds and pseudo-binary alloys with the CuAl2 (C16)-type structure II. Theoretical discussion of crystallographic parameters. *Journal of the Less Common Metals*, *27*(2), pp.187-193.

[41] Preston, G.D., 1931. XCIV. An X-ray investigation of some copper-aluminium, alloys. *The London, Edinburgh, and Dublin Philosophical Magazine and Journal of Science*, *12*(80), pp.980-993.

[42] Lukas, H.L. and Lebrun, N., 2005. Aluminum-Copper-Silicon. *Landolt-Bornstein New Series IV, G. Effenberg and S. Ilyenko, Eds*, *11*, pp.135-147.

[43] El-Boragy, M., Szepan, R. and Schubert, K., 1972. Kristallstruktur von Cu3Al2+ (h) und CuAl (r). *Journal of the Less Common Metals*, *29*(2), pp.133-140.

[44] Gulay, L.D. and Harbrecht, B., 2004. The crystal structure of ζ 1-Al 3 Cu 4. *Journal of alloys and compounds*, *367*(1), pp.103-108.

[45] Gulay, L.D. and Harbrecht, B., 2003. The Crystal Structure of ζ2- Al3Cu4-δ. *Zeitschrift für anorganische und allgemeine Chemie*, *629*(3), pp.463-466.

[46] Bradley, A.J., Goldschmidt, H.J. and Lipson, H., 1938. The intermediate phases in the aluminium-copper system after slow cooling. *J. Inst. Metals*, *63*, p.149.

[47] Kisi, E.H. and Browne, J.D., 1991. Ordering and structural vacancies in non-stoichiometric Cu–Al γ brasses. *Acta Crystallographica Section B: Structural Science*, *47*(6), pp.835-843.

[48] Liu, X.J., Ohnuma, I., Kainuma, R. and Ishida, K., 1998. Phase equilibria in the Cu-rich portion of the Cu–Al binary system. *Journal of Alloys and Compounds*, *264*(1), pp.201-208.

[49] Arnberg, L.A.R.S. and Westman, S.V.E.N., 1978. Crystal perfection in a noncentrosymmetric alloy. Refinement and test of twinning of the γ-Cu9Al4 structure. *Acta Crystallographica Section A: Crystal Physics, Diffraction, Theoretical and General Crystallography*, *34*(3), pp.399-404.

[50] Andrews, K.W. and Hume-Rothery, W., 1941. On the α/β Brass Type of Equilibrium. *Proceedings of the Royal Society of London. Series A, Mathematical and Physical Sciences*, pp.464-473.

[51] Kuwano, N., Doi, T. and Eguchi, T., 1977. Period of Antiphase and Tetragonality in the α2 Phase of Cu–Al Alloys. *Transactions of the Japan Institute of Metals*, *18*(11), pp.807-815.

[52] Straumanis, M.E. and Yu, L.S., 1969. Lattice parameters, densities, expansion coefficients and perfection of structure of Cu and of Cu–In α phase. *Acta Crystallographica Section A: Crystal Physics, Diffraction, Theoretical and General Crystallography*, *25*(6), pp.676-682.

[53] Jiang, H.G., Dai, J.Y., Tong, H.Y., Ding, B.Z., Song, Q.H. and Hu, Z.Q., 1993. Interfacial reactions on annealing Cu/Al multilayer thin films. *Journal of applied physics*, *74*(10), pp.6165-6169.

[54] Calvo, F.A., Ureng, A., De Salazar, J.G. and Molleda, F., 1988. Special features of the formation of the diffusion bonded joints between copper and aluminium. *Journal of materials science*, *23*(6), pp.2273-2280.

[55] Chen, C.Y. and Hwang, W.S., 2007. Effect of annealing on the interfacial structure of aluminum-copper joints. *Materials transactions*, *48*(7), pp.1938-1947.

[56] Hentzell, H.T.G., Thompson, R.D. and Tu, K.N., 1983. Interdiffusion in copper–aluminum thin film bilayers. I. Structure and kinetics of sequential compound formation. *Journal of applied physics*, *54*(12), pp.6923-6928.

[57] Yu, C.F., Chan, C.M., Chan, L.C. and Hsieh, K.C., 2011. Cu wire bond microstructure analysis and failure mechanism. *Microelectronics reliability*, *51*(1), pp.119-124.

[58] Kim, H.J., Lee, J.Y., Paik, K.W., Koh, K.W., Won, J., Choe, S., Lee, J., Moon, J.T. and Park, Y.J., 2003. Effects of Cu/Al intermetallic compound (IMC) on copper wire and aluminum pad bondability. *IEEE Transactions on Components and Packaging Technologies*, *26*(2), pp.367-374.

[59] Broddin, D., Van Tendeloo, G., Van Landuyt, J., Amelinckx, S. and De Graef, M., 1989. The long-period antiphase-boundary-modulated structures in Cu3+ xAl1− x. *Philosophical Magazine A*, *59*(5), pp.979-998.

[60] Tan, Y.Y. and Yong, F.K., 2010, July. Cu-Al IMC micro structure study in Cu wire bonding with TEM. In *Physical and Failure Analysis of Integrated Circuits (IPFA), 2010 17th IEEE International Symposium on the* (pp. 1-4). IEEE.

[61] Momma, K. and Izumi, F., 2011. VESTA 3 for three-dimensional visualization of crystal, volumetric and morphology data. *Journal of Applied Crystallography*, *44*(6), pp.1272-1276.

[62] Hirsch, P.B., 1956. Mosaic structure. *Progress in Metal Physics*, *6*, pp.236-339.

[63] "Scanning Electron Microscope." *Wikipedia*, Wikimedia Foundation, 23 Apr. 2018, en.wikipedia.org/wiki/Scanning_electron_microscope. www.ammrf.org.au/myscope/sem/background/concepts/interactions.php.

[64] Batson, P.E., Dellby, N. and Krivanek, O.L., 2002. Sub-ångstrom resolution using aberration corrected electron optics. *Nature, 418*(6898), p.617.

[65] "Transmission Electron Microscopy." *Wikipedia*, Wikimedia Foundation, 12 Apr. 2018, en.wikipedia.org/wiki/Transmission_electron_microscopy.

[66] Xu, H., Liu, C., Silberschmidt, V.V., Pramana, S.S., White, T.J., Chen, Z. and Acoff, V.L., 2011. Behavior of aluminum oxide, intermetallics and voids in Cu–Al wire bonds. *Acta Materialia*, *59*(14), pp.5661-5673.

[67] Li, J., Liu, L., Deng, L., Ma, B., Wang, F. and Han, L., 2011. Interfacial microstructures and thermodynamics of thermosonic Cu-wire bonding. *IEEE Electron Device Letters*, *32*(10), pp.1433-1435.

[68] England, L. and Jiang, T., 2007, May. Reliability of Cu wire bonding to Al metallization. In *Electronic Components and Technology Conference, 2007. ECTC'07. Proceedings. 57th* (pp. 1604-1613). IEEE.

[69] Williamson, G.K. and Hall, W.H., 1953. X-ray line broadening from filed aluminium and wolfram. *Acta metallurgica*, *1*(1), pp.22-31.

[70] Chen, J., Lai, Y.S., Wang, Y.W. and Kao, C.R., 2011. Investigation of growth behavior of Al–Cu intermetallic compounds in Cu wire bonding. *Microelectronics reliability*, *51*(1), pp.125-129.

[71] Haidara, F., Record, M.C., Duployer, B. and Mangelinck, D., 2012. Investigation of reactive phase formation in the Al–Cu thin film systems. *Surface and Coatings Technology*, *206*(19), pp.3851-3856.

[72] Tavassoli, S., Abbasi, M. and Tahavvori, R., 2016. Controlling of IMCs layers formation sequence, bond strength and electrical resistance in Al Cu bimetal compound casting process. *Materials & Design*, *108*, pp.343-353.

[73] Kinoshita, C., Tomokiyo, Y., Matsuda, H. and Eguchi, T., 1973. Local Atomic Arrangements and Anomalous Behavior in αCu–Al Alloys. *Transactions of the Japan Institute of Metals*, *14*(2), pp.91-96.

[74] Epperson, J.E. and Fürnrohr, P., 1980. Characterization of the locally ordered regions in short-range ordered α-phase Cu–Al alloys. *Acta Crystallographica Section A: Crystal Physics, Diffraction, Theoretical and General Crystallography*, *36*(3), pp.372-378.

[75] Varschavsky, A., Perez, M.I. and Löbel, T., 1975. An electron microscopic and diffraction study of Cu-9 wt pct Al alloy. *Metallurgical Transactions A*, *6*(3), p.577.

[76] Popplewell, J.M. and Crane, J., 1971. Order-strengthening in Cu−Al alloys. *Metallurgical and Materials Transactions B*, *2*(12), pp.3411-3420.

[77] Schönfeld, B., Roelofs, H., Malik, A., Kostorz, G., Plessing, J. and Neuhäuser, H., 1996. The microstructure of Cu-Al. *Acta materialia*, *44*(1), pp.335-342.

[78] Tomokiyo, Y., Kuwano, N. and Eguchi, T., 1975. Short Range Ordering in Deformed αCu–Al Alloys. *Transactions of the Japan Institute of Metals*, *16*(8), pp.489-499.

[79] Sugino, S., Nakanishi, N. and Mitani, H., 1964. Anomalous phenomena in α phase Cu-Al binary alloys.

[80] Varschavsky, A. and Donoso, E., 1991. Short-range ordering by excess and thermal vacancies during linear heating experiments in α-Cu Al alloys. *Materials Science and Engineering: A*, *145*(1), pp.95-107.

[81] Flandorfer, H., Rechchach, M., Elmahfoudi, A., Bencze, L., Popovič, A. and Ipser, H., 2011. Enthalpies of mixing of liquid systems for lead free soldering: Al–Cu–Sn system. *The Journal of chemical thermodynamics*, *43*(11), pp.1612-1622.

[82] Bramfitt, B.L., 1970. The effect of carbide and nitride additions on the heterogeneous nucleation behavior of liquid iron. *Metallurgical Transactions*, *1*(7), pp.1987-1995.

[83] Belin-Ferré, E., 2008. *Basics of thermodynamics and phase transitions in complex intermetallics* (Vol. 1). World Scientific.

[84] Gaudry, E., Shukla, A.K., Duguet, T., Ledieu, J., Dubois, J.M. and Fournée, V., 2010. Structural investigation of the (110) surface of γ-Al 4 Cu 9. *Physical Review B*, *82*(8), p.085411.

[85] Metallurgy, P., 2014. by DE Laughlin and K. Hono.

[86] Dahmen, U., 1982. Orientation relationships in precipitation systems. *Acta Metallurgica*, *30*(1), pp.63-73.

[87] Bunge, H.J., Weiss, W., Klein, H., Wcislak, L., Garbe, U. and Schneider, J.R., 2003. Orientation relationship of Widmannstätten plates in an iron meteorite measured with high-energy synchrotron radiation. *Journal of applied crystallography*, *36*(1), pp.137-140.

[88] Shang, P.J., Liu, Z.Q., Pang, X.Y., Li, D.X. and Shang, J.K., 2009. Growth mechanisms of Cu3Sn on polycrystalline and single crystalline Cu substrates. *Acta Materialia*, *57*(16), pp.4697-4706.

[89] Kern, K., David, R., Palmer, R.L. and Comsa, G., 1986. Complete wetting on ''strong''substrates: Xe/Pt (111). *Physical review letters*, *56*(26), p.2823.

[90] Dubois, J.M., 2012. Properties-and applications of quasicrystals and complex metallic alloys. *Chemical Society Reviews*, *41*(20), pp.6760-6777.

Biographical Information

Valery Ouvarov-Bancalero received his B.S. in Metallurgical Engineering from the Université de Lorraine in France in 2011, and his M.S. in Energy Science & Materials from the Université du Québec-Institut National de la Recherche Scientifique in Canada in 2014. He subsequently joined the University of Texas at Arlington in Fall 2015 to pursue a Ph.D. in Materials Science & Engineering under the supervision of Dr. Choong-Un Kim. During his time as a Ph.D. student, he worked on multiple projects related to metallurgical degradation phenomena in metal interconnects.